

CHAPTER 1

INTRODUCTION

1.1 Background of the Research Studies

A solar cell or photovoltaic cell is a semiconductor device that capable to absorb sunlight and directly transforms it into electrical energy by way of the photovoltaic effect. The term “photovoltaic” arises from the Greek letter in which “phos” meaning light and “voltaic” signifying electrical, that refers to the name of the Italian physicist Alessandro Volta, after whom the measurement unit volt is denoted (Smee, 1849). A photocurrent flow is induced when a formed bound electron-hole pair is dissociated by a potential barrier (such as p-n heterojunction) upon an excitation of electron from the valence band into the conduction band after a photon energy in sunlight that equal or greater than that of the band gap is absorbed.

Typically, solar cells do not require chemical reactions to generate electric power and they have no moving parts that require service or fuels for replenishment. Thus, solar cells are favorably to be explored as promising alternative renewable source of energy, especially for the power generation in remote locations including space satellites. Nowadays, solar cells have been intensively used to power many types of optoelectronic equipments, including calculators, solar panel, advertising signs, and remote radiotelephones.

The solar cells have evolved dramatically, and in the past few years, significantly large strides have been made in the field of research and development of solar cells. There are three main classifications of solar cells technology, which can be referred to as generation on account of when the technology first appeared. The first generation of solar cells consists of silicon or germanium that doped with boron or phosphorous in a p-n junction. They accounted for around 90% of commercial

production in the world, and achieved a theoretical maximum efficiency of around 33%., though the market shares of these solar cells are gradually declining. However, the manufacturing processes that used to produce silicon-based solar cells are inherently expensive and detrimental to the environment. And later, the second generation of solar cells, which is also called as thin-film solar cells, is designed to be substantially cheaper and easier to be mass produced than silicon-based first generation of solar cells. There are many types of thin films such as polycrystalline silicon, micro-crystalline silicon, amorphous silicon, cadmium telluride or copper indium selenide/sulfide, which are applied onto glass or plastic substrates. Nevertheless, the efficiency of this second generation solar cells is lower compared to the first generation. Besides, relatively high production cost of thin films that may due to the excess consumption of inorganic semiconducting materials and equipments used in the fabrication process still become the main drawbacks of these types of solar cells. The necessity for solving the problems and bottlenecks drives the previous two generation of solar cells to make urgent search for cost-effective and environmental-friendly solar cells.

And thus, the third generation of solar cells has become the cutting edge of solar technology which preferably employs organic semiconducting materials, such as conductive organic polymers or small organic molecules as photoactive thin film over a wide range of potential solar devices including polymer solar cells, nanocrystalline solar cells, and dye-sensitized solar cells. Though it is still in the research phase, the third generation of solar cells has advanced well beyond the silicon-based solar cells. Recently, a hypothetical “forth generation” of solar cells based on composite photovoltaic technology is designed, in which semiconducting polymers with nanoparticles are mixed together to form a single active layer, in order to enhance the device efficiency (Bharathan & Yang, 1998; Chamberlain, 1983).

However, organic materials commonly possess a lower dielectric constant and a higher exciton binding energy than their inorganic semiconductors counterparts. The solar power conversion efficiency is limited due to the low charge mobility that leads to a less efficient of charge transport to the respective electrodes. In order to address such problems, two materials of different p-type and n-type that differ in electron donating and accepting properties have been utilized in the organic solar cells. Free charge carriers are created by photoinduced electron transfer between the two components and establish a p-n junction. To further improve the power conversion efficiencies, the electron-donor and acceptor need to be brought in close contact which is usually realized by mixing them in a single layer, yielding a so-called bulk heterojunction (BHJ) structure in order to form a more efficient separation of charge transport layers (Halls et al., 1995; Yu, Gao, Hummelen, Wudl, & Heeger, 1995).

In this dissertation, research studies and results are presented, focusing on the hybrid organic solar cells, in which a p-type conjugated polymer is blended with n-type inorganic semiconductors.

1.2 History of organic solar cells (OSCs)

At the preliminary stage, photovoltaic (PV) effect was discovered by Alexandre Edmond Becquerel in 1839, who observed a photocurrent when platinum electrodes that coated with silver bromide or silver chloride was illuminated in an aqueous solution (Becquerel, 1839). Later, photoconductivity phenomenon was again detected by Willoughby Smith (1873) and also by William Grylls Adams (1876) who working on selenium. Anthracene was the first organic compound in which its photoconductivity was studied by Alfredo Pochettino (1906) and Max Volmer (1913), respectively. In the early of 1960s, it was found that many common dyes and some other organic materials such as, chlorophylls, carotenes and other porphyrins, as well as phthalocyanines, were among the substances to exhibit the PV effects. In 1958, Kearns and Calvin who worked

with magnesium phthalocyanine (MgPh) had successfully measured a photovoltage of 200mV (Kearns & Calvin, 1958). In 1980s, the first polymer based solar cells was fabricated with limited power conversion efficiency (PCE) well below of 0.1% (Spanggaard & Krebs, 2004). However, the drawback was improved by designing bulk heterojunction-based solar cells, which was later made by Ching W. Tang (1986), in which the power efficiency was intensively increased to about 1%. Later, first polymer/fullerene based solar cells were successfully made by Sariciftci et al. (1993).

In recent years, a lot of attention has been focused on hybrid solar cells composed of p-type conjugated polymers with n-type inorganic semiconductors. Typically, the device performance of a hybrid solar cell is improved compared to a pristine polymer solar cell. AM 1.5 power conversion efficiency of 1.7% was achieved in poly(3-hexylthiophene) (P3HT):CdSe hybrid solar cell (Huynh, Dittmer, & Alivisatos, 2002). Huisman *et al* (2003) reported 0.06% efficiency for solar cells based on TiO₂:poly(3-octyl)thiophene. In 2006, Waldo J.E. Beek investigated hybrid solar cell made from regioregular polythiophene and ZnO nanoparticles, a PCE of 0.9% was obtained (Beek, Wienk, & Janssen, 2006). Liu et al. (2009) made hybrid PV cells based on copper-phthalocyanine (CuPc) and fullerene with vertically oriented ZnO nanowires to obtain PCE value of about 0.53%. More recently, efficiencies exceeding 3% were reported for polymer nanocrystal hybrid solar cells based on mixtures of cadmium selenide (CdSe) quantum dots with low band gap polymer poly[2,6-(4,4-bis-(2-ethylhexyl)-4H-cyclopenta[2,1-b;3,4-b']-dithiophene)-alt-4,7-(2,1,3-benzothiadiazole)] (PCPDTBT) under inert atmosphere in a glove box system (Zhou et al., 2011). Celik et al. (2012) achieved an improved PCE approaching 3.5% for BHJ hybrid solar cells based on high mobility inorganic semiconductors of CdSe nanorods and PCPDTBT. All these achievements indicated that OSCs have good potential in PV application.

However, the device efficiencies are still far away compared to silicon-based PV cells.

Table 1.1 shows some important milestones in the development of OSCs.

Table 1.1: A list of development in the organic solar cells.

Year	Some important milestones in the development of organic solar cells	References
1839	Becquerel discovered the photovoltaic (PV) effect through an electrochemical experiment.	(Becquerel, 1839)
1873 & 1876	Smith and Adams observed the photoconductivity of selenium.	(Adams, 1876; Smith, 1873)
1906 & 1913	Pochettino and Volmer studied the photoconductivity of anthracene.	(Moore & Silver, 1960; Volmer, 1913)
1958	Kearns and Calvin worked with magnesium phthalocyanine (MgPh) and had been successfully measured a photovoltage of 200mV.	(Kearns & Calvin, 1958)
1986	Tang fabricated the first bulk heterojunction (BHJ)-based solar cell.	(Tang, 1986)
1993	Sariciftci successfully made the first polymer/fullerene based solar cell.	(Sariciftci, et al., 1993)
1991	Hiramoto fabricated the first dye/dye BHJ solar cell.	(Hiramoto, Fujiwara, & Yokoyama, 1991)
1994	Yu fabricated the first polymer/fullerene BHJ solar cell.	(Po, Maggini, & Camaioni, 2009)
1995	Yu and Hall fabricated the first polymer/polymer BHJ solar cell.	
2000	Peter and van Hal applied oligomer-C ₆₀ dyads/triads as the photoactive material in PV cell.	(Peeters et al., 2000)
2001	Ramos made double-cable polymers in PV cells.	(Ramos, Rispens, van Duren, Hummelen, & Janssen, 2001)
2002	Huynh and his co-researchers successfully fabricated hybrid solar cells based on a blending of polymer P3HT with inorganic CdSe and achieved a power conversion efficiency of 1.7%.	(Huynh, et al., 2002))
2003	Huisman reported 0.06% efficiency for solar cells based on TiO ₂ :poly(3-octyl)thiophene.	(Huisman, et al., 2003)
2006	Beek et al. studied hybrid solar cells based on polythiophene and ZnO nanoparticles and reported a power conversion efficiency of 0.9%.	(Beek, et al., 2006)

2007	Ko et al. fabricated a single layer of BHJ solar cell by blending P3HT and a small organic molecule of fullerene derivative called PCBM. The reported efficiency of 5.2 % has been achieved.	(Ko, Lin, Chen, & Chu, 2007).
2008	Saunders, B. R et al. studied P3HT:inorganic nanoparticles–polymer PV cells based on different types of inorganic materials (CdSe, ZnO or PbS).	(Saunders & Turner, 2008)
2009	Liu et al. made hybrid PV cells based on copper-phthalocyanine and fullerene with vertically oriented ZnO nanowires to obtain efficiency of about 0.53%.	(Liu, et al., 2009)
2011	Zhou et al. reported efficiencies exceeding 3% for polymer nanocrystal hybrid solar cells based on mixtures of CdSe quantum dots with PCPDTBT under inert atmosphere in a glove box system.	(Zhou, et al., 2011)
2011	Basten et al. reported 0.76% efficiency for PV devices based on fully P3HT infiltrated ZnO nanorod arrays.	(Baeten et al., 2011)
2012	Celik et al. used high mobility materials of PCPDTBT:CdSe nanorods to achieve device efficiency of about 3.5%.	(Celik, et al., 2012)

1.3 The reasons of investigation on hybrid polymer solar cells

In the 21st century, there is no short term ambition to replace silicon or thin film technologies, but to develop a long term cost-effective technology based on environmentally friendly materials. Hybrid polymer solar cells have been deeply investigated due to their peculiar advantages. Typically, they can be produced relatively easily using low-cost solution processable techniques such as spin coating, inkjet-printing, dip coating techniques and so on. Large scale production of hybrid solar cells is favorable, since the amounts of organic materials consumed are relatively small (100 nm thick film), as compared to the silicon-based solar cells which usually require micrometer scale of layer thickness. Besides, hybrid polymer solar cells can be tuned chemically or mechanically in hence to adjust band gap, charge transport, valence and conduction energy levels, solubility and several other structural properties (Hoppe & Sariciftci, 2004). Conversely, silicon-based solar cells are heavy, fragile and require a

energy pay back time of about 4 years, compared to the polymeric based solar cells of which can be applied onto flexible, lightweight substrates, and the energy payback time merely lies within a couple of weeks (Shah, Platz, & Keppner, 1995). In addition, their excellent mechanical flexibility is very welcome for many applications on curved surfaces and ubiquitous usages, such as applied on house roof as solar panel.

In this research work, poly(3-hexylthiophene) P3HT as an electron donating material is studied. P3HT is a well known conjugated (semiconducting) polymer which possesses peculiar optoelectronic properties such as good chemical stability and low optical band gap (~ 1.9 eV). Since it has the highest charge carrier mobility among the conjugated polymers and its hole mobility is reported as high as $0.1 \text{ cm}^2 \text{V}^{-1} \text{s}^{-1}$, P3HT is preferably be chosen as an excellent electron donor (Sirringhaus, Tessler, & Friend, 1998). Besides, P3HT has the advantage of being easy to dilute in common organic solvents such as chloroform and chlorobenzene due to the presence of alkyl side chain on the thiophene group. By blending P3HT and a small organic molecule of fullerene derivative called [6,6]-phenyl- C_{60} -butyric acid methyl ester (PCBM), it was reported that a power conversion efficiency of 5.2 % has been achieved for a single layer of bulk heterojunction solar cell (Ko, et al., 2007). Nevertheless, the limitations such as low charge mobility and low absorbance in near-infrared (NIR) spectrum of both P3HT and PCBM components, compared to inorganic semiconductors are seriously concerned too.

Hybrid polymer solar cells, a subclass of BHJ, which are a mixture of nanostructures of both organic and inorganic materials employing conjugated polymers (semiconducting polymers) like regioregular poly(3-hexylthiophene) (P3HT) as electron donating component and an inorganic semiconductor nanoparticle as electron accepting component (Xu & Qiao, 2011). Alternative types of hybrid polymer solar cells, based on conjugated polymers combined with n-type inorganic nanoparticles (NPs), such as cadmium sulfide (CdSe) (Sun, Snaith, Dhoot, Westenhoff, & Greenham, 2005),

titanium dioxide (TiO₂) (Kwong et al., 2004), plumbum sulfide (PbS) (Zhang, Cyr, McDonald, Konstantatos, & Sargent, 2005) and zinc oxide (ZnO) (Beek, Wienk, & Janssen, 2004) have been employed due to the advantages of high electron mobility and excellent chemical and physical stability of inorganic semiconductors.

There are many techniques can be used to fabricate hybrid solar cells such as inkjet printing, dip coating, thermal evaporation and physical vapour deposition technique. In this research work, spin coating technique is chosen to produce homeogenous, uniform thin film with required thickness onto large area. A typical structure of the organic/inorganic hybrid solar cell is metal/polymer:inorganic nanoparticles/indium tin oxide (ITO). ITO serves as an anode and is treated as front electrode due to its transparency to light. On the other hand, aluminum (Al) is normally used as the top metal cathode, which is deposited on top of the blend film by thermal evaporation under a high vacuum condition. To further enhance the device performance, Poly(3,4-ethylenedioxythiophene)-poly(styrenesulfonate) (PEDOT:PSS) is used as a hole-tranporting layer in the solar cell, at the same time it may aid to reduce the surface roughness of ITO (Huang et al., 2005).

Typically, the performances of optoelectronic devices can be improved by controlling the morphology of films (Brabec, Sariciftci, & Hummelen, 2001) which is influenced by processing conditions such as the blend composition, types of inorganic nanoparticles used, chemical synthesis route, and thermal annealing process. Thus, the study of the effects of certain processing conditions on the optical, structural, morphological as well as the electrical properties of the hybrid solar cells are seriously focused in this work. In order to further improve the film surface morphology and thus the charge transport through the active layer to the respective electrodes, sol-gel synthesis route is utilized to produce a better mixing blend of P3HT and inorganic compound.

The common fundamental problem associated to the hybrid polymer solar cells is the short life span due to the low stability of the devices under ambient condition. Degradation might probably take place once the polymer films expose to the air, which leads to the deterioration in device performances. Thereby, high device efficiency is still remaining the main challenge in this work and need to be addressed in advance for future works.

1.4 Research Objectives

The main objective of this work is to fabricate and characterize hybrid polymer solar cells based on a blend of a p-type conjugated polymer of P3HT and n-type inorganic nanoparticles. The second objective is to investigate the effects of blend composition (or known as doping effects) on the optical, structural, morphological as well as the electrical properties of the hybrid polymer solar cells by varying the content of inorganic nanoparticles in the blends. The third objective is to make comparison on the physical properties and device performances of solar cells based on three different types of as-purchased n-type inorganic metal oxide nanoparticles, namely zinc oxide (ZnO), titanium dioxide (TiO₂) and yttrium oxide (Y₂O₃). The forth objective is to study the effects on film surface morphology and device performances for P3HT:ZnO solar cells prepared from sol-gel synthesis route under several different approaches including varying the sol content in the P3HT blends, different annealing temperature, and inserting an additional ZnO buffer layer between the active layer and Al cathode.

As a summary, the objectives of this study are listed below:

- (i) To fabricate and characterize hybrid polymer solar cells consist of P3HT and inorganic nanoparticles,
- (ii) To investigate the effects of blend composition (or known as doping effects) on the optical, structural, morphological as well as the electrical properties of the hybrid polymer solar cells,

- (iii) To compare the physical properties and device performances of the hybrid solar cells consist of inorganic metal oxide nanoparticles, namely ZnO, TiO₂ and Y₂O₃,
- (iv) To study the effects on film surface morphology and device performances for P3HT:ZnO solar cells prepared from sol-gel synthesis route.

1.5 Dissertation Outline

Chapter 2 explains the literature review and the fundamental aspects of the peculiar properties of conjugated polymer, electron-donating polythiophene and several types of electron-accepting inorganic nanoparticles used in this work. Besides, the background of sol gel synthesis route for inorganic compound is well elaborated in this chapter too. Additionally, it explains the basic working principle, key parameters and different types of device architectures for hybrid solar cells.

Chapter 3 explains the experimental methodology involved in this research work. The sub-topics in this chapter include chemical and solutions preparation, sol gel synthesis route, thin film preparation via spin-coating technique, device fabrication, aluminum (Al) electrode deposition via thermal evaporation method, and several types of characterization aspects, namely: ultraviolet-visible-near infrared (UV-VIS-NIR), X-ray diffraction (XRD), atomic force microscopy (AFM), field-effect scanning electron microscopy (FESEM), and photovoltaic measurements.

Chapter 4 explains the results and discussion on the optical, structural, morphological as well as the electrical characterizations of hybrid solar cells based on as-purchased P3HT and ZnO inorganic nanoparticles. The effects of varying the nanoparticles content in blends on the physical properties and device performances are discussed.

Chapter 5 is divided into two parts. Part I studies about the effects of blend composition for the other two types of hybrid systems, namely P3HT:TiO₂ and

P3HT:Y₂O₃. Besides, it elucidates the comparison in physical properties and device performances between the three different types of P3HT:inorganic metal oxide nanoparticles hybrid systems (P3HT:ZnO, P3HT:TiO₂ and P3HT:Y₂O₃). For Part II, the results obtained for P3HT:ZnO hybrid systems prepared from sol-gel synthesis route by varying several processing conditions are presented and discussed in advance.

Finally, Chapter 6 concludes and suggests some future works which can be carried out associated to this work. Figure 1.01 shows the block diagram of the summary of the research methodology used in this study.

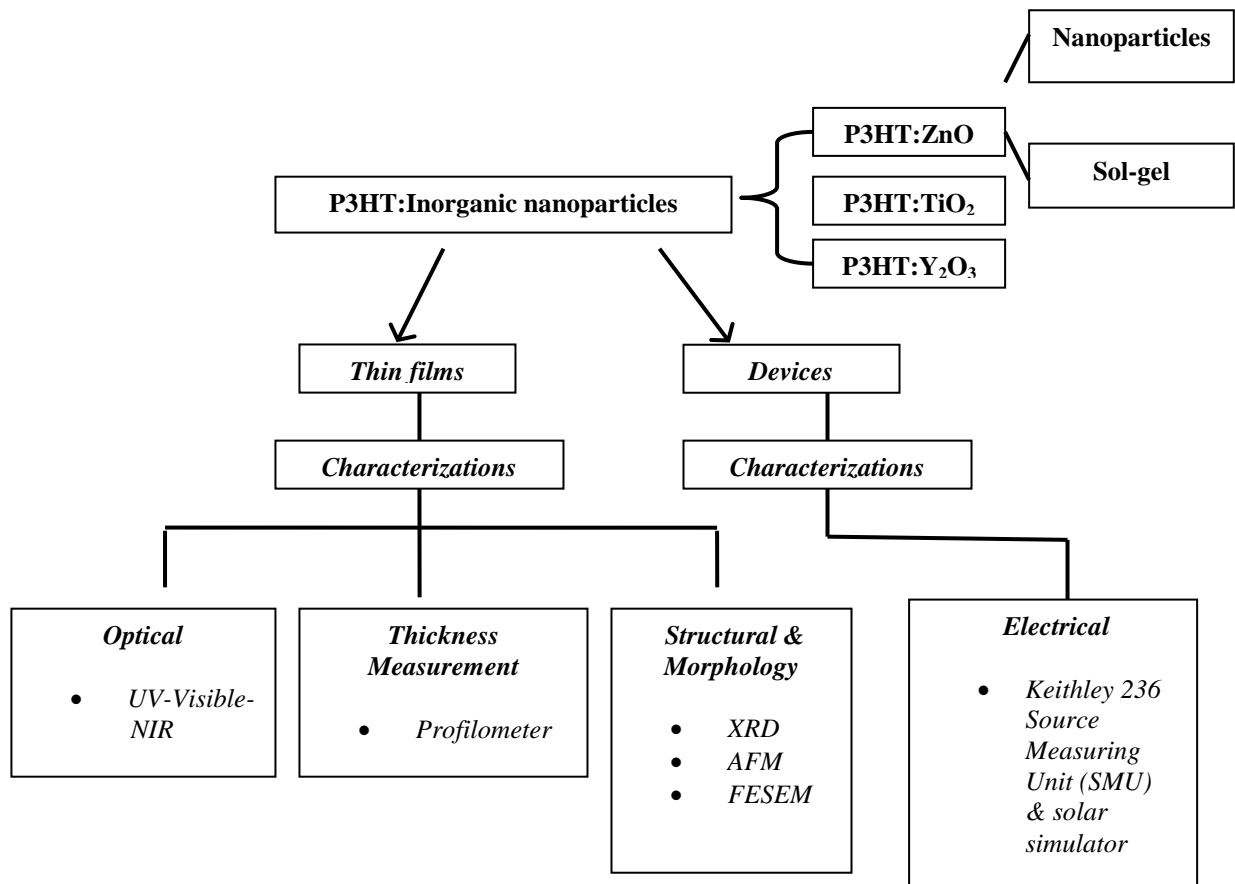


Figure 1.01: Block diagram of research methodology used in this study.

CHAPTER 2

THEORETICAL BACKGROUND

2.1 Overview

This chapter presents related theory of this whole research work, including the introduction of conjugated polymer and further explanation of its peculiar physical and electrical properties. Besides, this chapter reveals several unique properties possessed by the required donor and acceptor materials used in this research work, namely: polythiophene and three different types of semiconducting inorganic nanoparticles. In addition, the fundamental principle of sol-gel synthesis approach is well elaborated in this chapter as well. Lastly, a brief description on the basic photovoltaic working operation, key parameters and several types of device architecture forms of hybrid solar cells are discussed in this chapter.

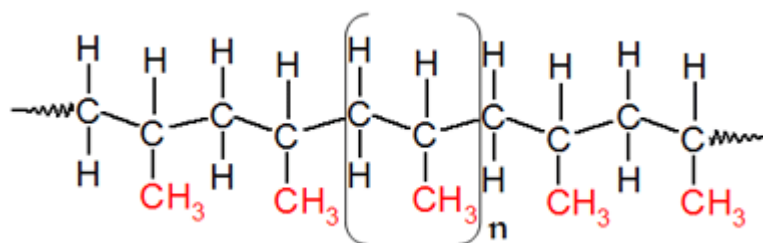
2.2 Conjugated Polymers

In general, polymers are well-known as macromolecules which are formed by a number of linked repeating units of monomers (Callister, 2007). They are basically two categories of polymers; which are conjugated polymers and non-conjugated polymers. Non-conjugated polymer, which consisting of repeating single sigma σ -bond in the polymer chain structure, are electrically insulating in nature and transparent to visible light, due to their relatively large energy gap (Salaneck, Stafström, & Brédas, 1996). In the other way, conjugated polymers can be well recognized since they exhibit a framework of alternating single and double bonds structure (conjugation) (Skotheim, Elsenbaumer, & Reynolds, 1998) and possess a pi-bond (π -bond) network extending along the chain (Kalinowski, 1999). Some examples of non-conjugated and conjugated polymers are shown in Figure 2.01. Each single bond comprises of a substantially

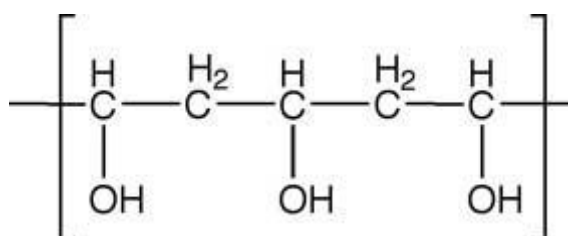
localized sigma-bond (σ -bond) that forming a strong chemical bond whereas every double bond comprises of a less strongly localized π -bond with an σ -bond. In the sense, there are two fundamental kinds of carbon bond hybridization present in common organic molecules, namely sp^3 and sp^2 hybridization of carbon atoms. Among all the others basic representative elements of conjugated polymers, let consider ethylene (see Figure 2.02) as an example. Each carbon atom in a molecule has three nearest neighbors, hence 3 equivalent σ -bonds consisting of C-H and C-C bonds are formed. Each carbon atom possesses an unbounded, delocalized free valence electron. In the means to achieve complete electron configuration at the outer shell, the odd valence electrons have to be paired up by constructing a second covalent bond between the two carbon C-C atoms. Consequently, the atoms are essentially to alter their p_z orbital structure, in the sense to accommodate the formed second C-C bond. However, this second C-C bond is relatively weak since the electrons in the bond are less tightly bound to the carbon nuclei. And hence, this bond is termed as π bond. It can be considered to be a more delocalized entity as less energy is required to perturb the electron from it (Petty, Bryce, & Bloor, 1995).

For a common inorganic semiconductor, its electronic structure consists of a conduction band (CB) and a valence band (VB) which is separated by an energy band gap (E_g), and its size is dependent upon the types of materials. Conjugated polymers act as semiconductors, and hence their electronic properties are analogous to those of inorganic semiconductors. The semiconducting properties of conjugated polymers arise from the π bonds. The π -bonds are delocalized throughout the whole molecule. The quantum mechanical overlap of p_z orbitals give rises to two orbitals, a filled bonding (π) orbital and an empty antibonding (π^*) orbital which are analogous to the valence band and conduction band for inorganic semiconductor, as shown in Figure 2.03. The lower energy π -orbital produces the Highest Occupied Molecular Orbital (HOMO), whereas

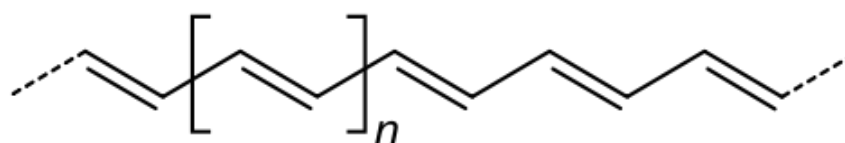
the higher energy π^* -orbital forms the Lowest Unoccupied Molecular Orbital (LUMO). The difference in energy between the two orbital levels gives rise to band gap that determines the optical properties of the organic material. Most conjugated polymers have a band gap in the range from 1.5-3.0 eV, which are favorable for various kinds of optoelectronic applications (Kido, Hongawa, Okuyama, & Nagai, 1994; Simon, André, Lehn, & Rees, 1985).



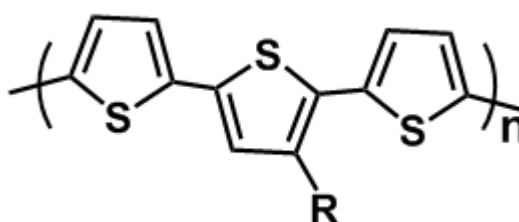
1(i)



(ii)



2(i)



(ii)

Figure 2.01: The examples of 1) non-conjugated polymers: (i) Polypropylene, (ii) Poly(vinyl alcohol); 2) conjugated polymers: (i) Polyacetylene, (ii) Polythiophene (Skotheim, et al., 1998).

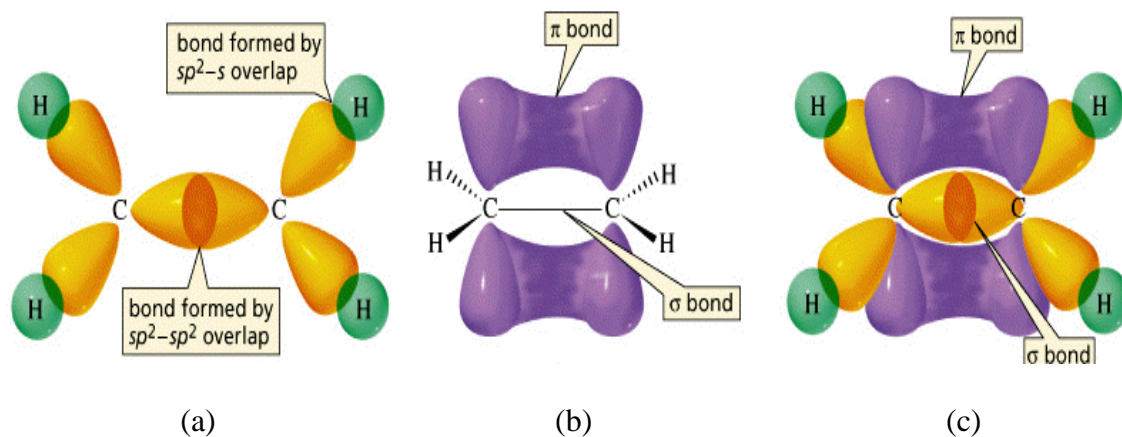


Figure 2.02: (a) The structure of ethylene comprises of σ bonds which formed from the three sp^2 -hybridized orbitals on each carbon atom. (b) The formation of π bond due to the overlap of the unhybridized p_z orbital. (c) A cutaway view of the whole σ and π system within the ethylene molecule (Hari Singh Nalwa, 2002).

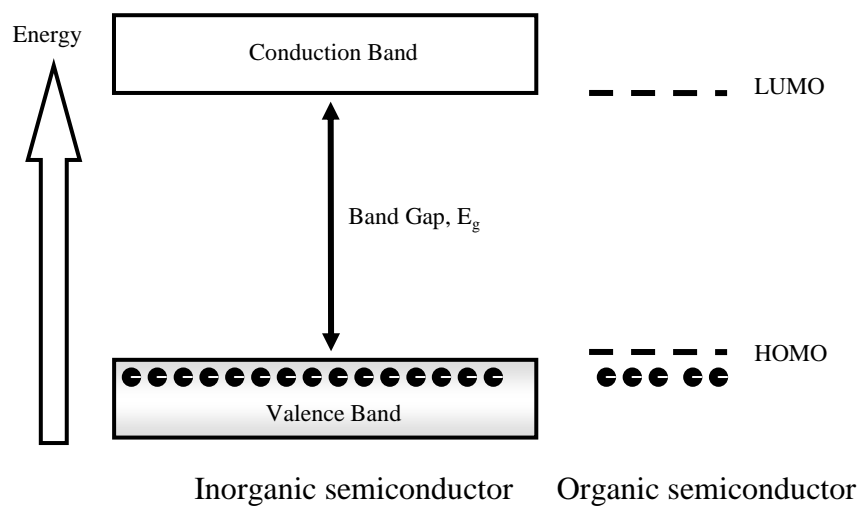


Figure 2.03: The schematic diagram of HOMO and LUMO bands.

2.3 Charge Transport Characteristics of Conjugated Polymers

Basically, the charge transport characteristics of conjugated polymers are governed by their backbone system; however these characteristics can be significantly affected by the intramolecular and intermolecular interactions. Intrachain charge diffusion is strongly dependent upon the chemical structure and molecular weight of polymer, the conformation of the polymer backbone, the number and nature of defect sites as well. On the other hand, the interchain charge diffusion is governed by the degree of order and orientation (Skotheim, et al., 1998).

In addition, charge transport process of conjugated polymers depends on their charge carrier mobility as well. Carriers with higher mobility are favorable for more efficient charge transport compared to those with lower mobility. Here, the charge carrier mobility of conjugated polymers can be well illustrated as a function of intrachain charge diffusion and interchain interaction (Sirringhaus et al., 1999; Tokuhisa, Era, & Tsutsui, 1998), as shown in Figure 2.04.

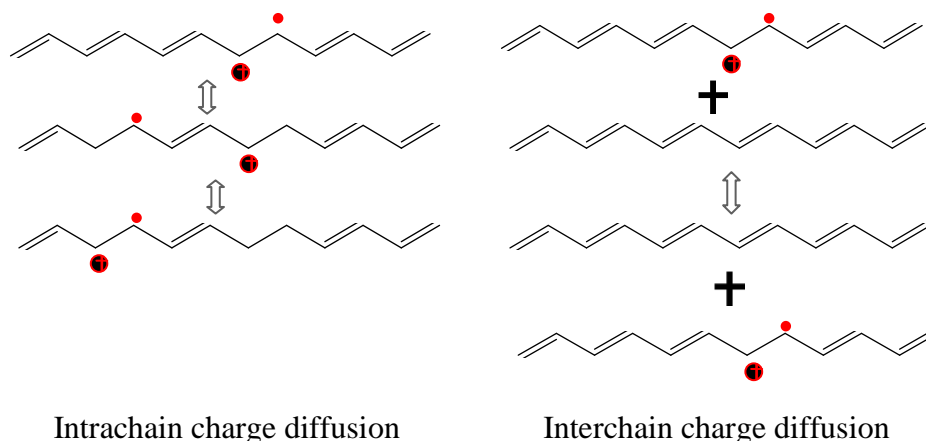


Figure 2.04: Schematic representation of intrachain charge diffusion (left) and interchain charge diffusion (right) in polyacetylene.

More recent research studies have shown that the carrier mobility can be increased in more well-organized structures due to the enhancement of interchain interaction that involving hopping process within the polymer, in which it will be

further discussed in following section. Besides, thermal annealing process may also contribute to the improvement in carrier mobility, due to a better ordering and overlap between aggregates (Li, Shrotriya, Yao, & Yang, 2005).

2.4 Electronic Properties of Conjugated Polymers

Due to the delocalization of electrons, mostly through the overlap of π -orbitals along the conjugated backbones of polymers, conjugated polymers possess electrical conductivity (Kittel, 2005). Electronic properties of conjugated polymers can be well described in terms of semiconductor physics. Typically, the π -orbitals overlap is weaker than σ -orbitals overlap. The σ -bonds mainly contribute to the stability of the molecular structure (Cojan, Agrawal, & Flytzanis, 1977). The energy difference between the bonding and antibonding molecular orbitals is larger for the π - π^* than for the σ - σ^* orbitals, and those are referred as HOMO and LUMO respectively, in terms of molecular physics.

The electronic properties of conjugated polymer was first explored by Heeger's group (Su, Schrieffer, & Heeger, 1979). According to SSH theory, conjugated polymers are generally divided into two categories of electronic structures, namely: conjugated polymer with degenerate ground state and conjugated polymer with non-degenerate ground state. Example of conjugated polymers with degenerate ground state is *trans*-polyacetylene. On the other hand, *cis*-polyacetylene and all the others conjugated polymers are those with non-degenerate ground state. In this view, energy band gap is a result of the bond length alternation. Potential energy as a function of the bond length alternation $E(\Delta r)$ for these two different categories of conjugated polymers is shown in Figure 2.05. For both cases, the $E(\Delta r)$ exhibits one maximum point with two minima. The π -electrons are remain unpaired and the $E(\Delta r)$ value becomes zero when reach the maximum point. For conjugated polymer with degenerate ground state, the change in the bond length, Δr is equivalent that produces homogeneous structures (phase A and

phase B) with identical ground state energy, as exhibited in Figure 2.05 (a). The π -electrons are hence delocalized along the carbon chains with equivalent bond length (Bredas, Heeger, & Wudl, 1986; O'Reilly, 2002).

However, for non-degenerate ground state conjugated polymers, two different structures with different energies are formed, which are aromatic and quinoid structures, due to the different bond length alternation, as shown in Figure 2.05 (b). The aromatic-type structure has a larger band gap and is therefore more energetically stable than the other one.

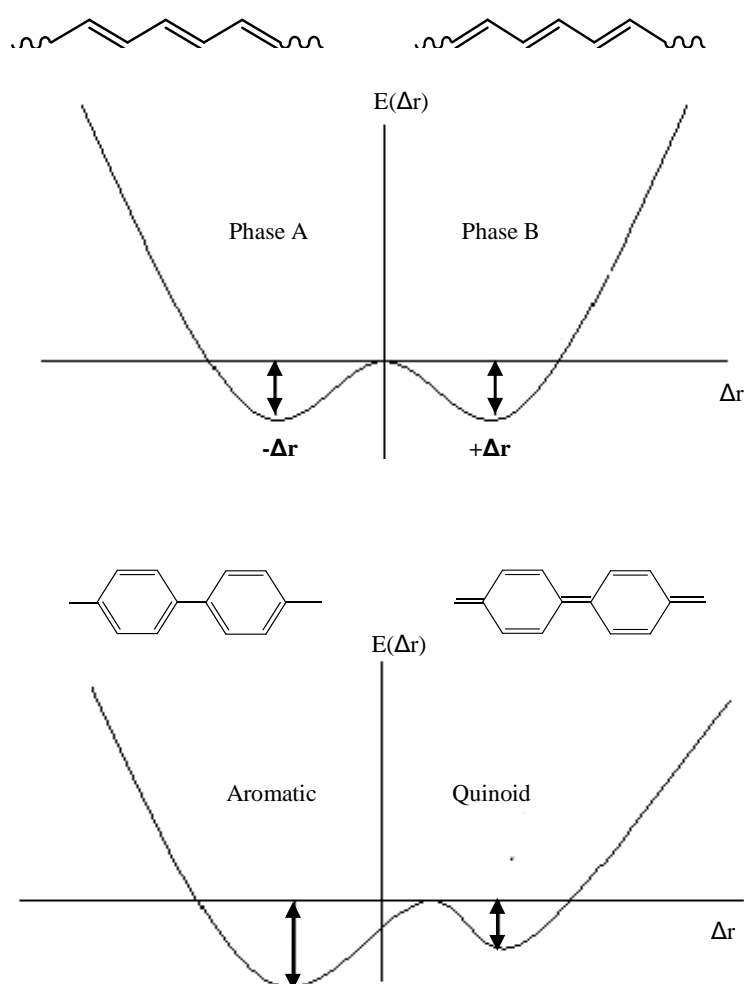


Figure 2.05: Potential energy as a function of bond length alternation for the two categories of conjugated polymers are exhibited for (a) a degenerate ground state conjugated polymer, *trans*-polyacetylene; (b) a non-degenerate ground state conjugated polymer (in the given example is poly-para-phenylene (PPP)).

Based on the two categories, different non-linear excitations are obtained. Degenerate conjugated polymers produce solitons. Figure 2.06 shows the energy diagram and schematic structure for soliton in conjugated polymers, in which one new energy state is formed between the band gap. This energy state can be either empty (positive soliton is resulted), singly occupied (neutral soliton), or doubled occupied (negative soliton). In contrast to degenerate conjugated polymers, two states are formed between the band gap in non-degenerate conjugated polymers, which may due to the structural relaxation of the backbone chain. There are 3 types of quasi particles found, which are exciton (neutral), polarons (singly charged), and bipolarons (double charged), as shown in Figure 2.07. Polarons exhibit two allowed optical transitions, one with high energy, HE and the other with low energy, LE. Bipolaron exhibits merely one optical transition and does not have any unpaired electron. Hence, a more profound effect for organic solar cells emerges in the non-degenerate ground state case, as excitons are more possibly to be formed through an excitation of polymer (Winder & Sariciftci, 2004).

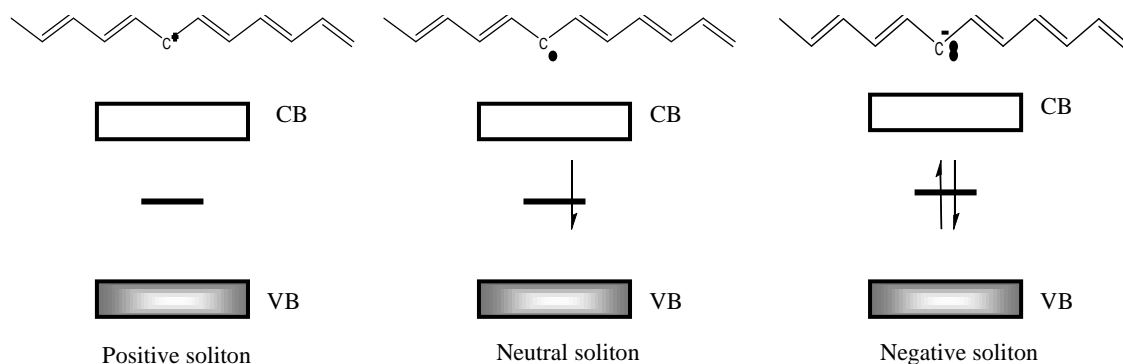


Figure 2.06: Schematic structure and energy diagram for solitons in conjugated polymer is shown.

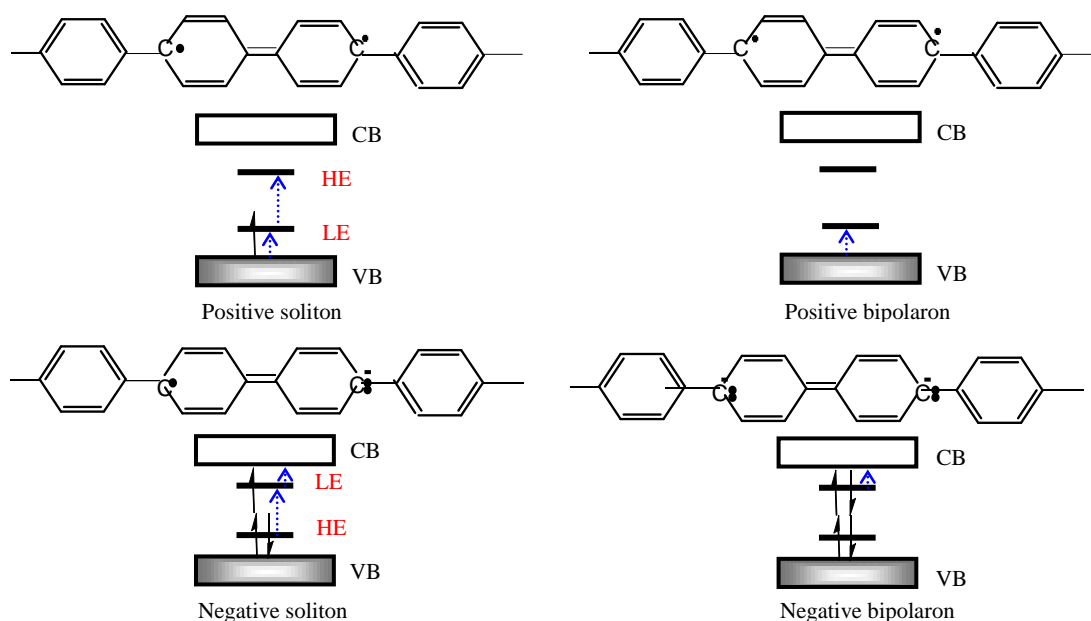


Figure 2.07: Schematic structure and band diagrams for excitations in non-degenerate ground state conjugated polymers. Allowed optical transitions are exhibited by the blue-colored dashed arrows.

2.5 Doping

Since conjugated polymers are kinds of semiconductors, their electronic properties can be tuned by doping, which is a process by either removing electrons from the π -conjugated system (oxidation, p-type doping) or adding electrons into the π -system (reduction, n-type doping) via the means of chemical or electrochemical methods (Elsenbaumer, Jen, & Oboodi, 1986). For further explanation, let consider polyacetylene and polythiophene as examples.

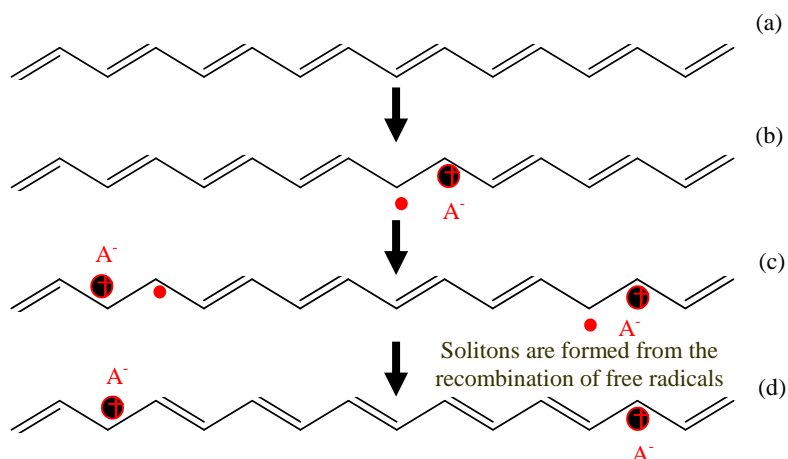


Figure 2.08: Removal of two electrons (p-type doping) from a polyacetylene chain produces two radical cations. The combination of both radicals forms a spinless di-cation.

The doping process (p-doping) of polyacetylene is described in Figure 2.08((a)-(d)). Initially, an electron is removed from the π -system of polyacetylene that leads to the formation of a radical cation (Fig.b). The abstraction of a second electron may form second radical cation (Fig.c). The recombination of the two radical cations gives rise to a spinless dication (Fig.d). Further oxidation takes place in the similar way leads to positive solitons. Each soliton forms up a boundary which separating domains with different phases of their π -bonds. On the other hand, cations are inserted into the polymer chain and forming negative solitons for n-type doping of polyacetylene.

For polythiophene case (heterocyclic conjugated polymer), different charge configuration can be formed. The doping process of polythiophene is depicted in Figure 2.09((a)-(c)). The removal of electron from π -conjugated system of polythiophene may produce a radical cation which is known as polaron (Fig.b), induces the formation of quinone-type bond sequence based domain within the poly(2,5-thienylene) chain possessing aromatic bond sequences. The removal of second electron gives rise to another polaron or a spinless bipolarons (Fig.c) (Heeger, Sariciftci, & Nandaa, 2010).

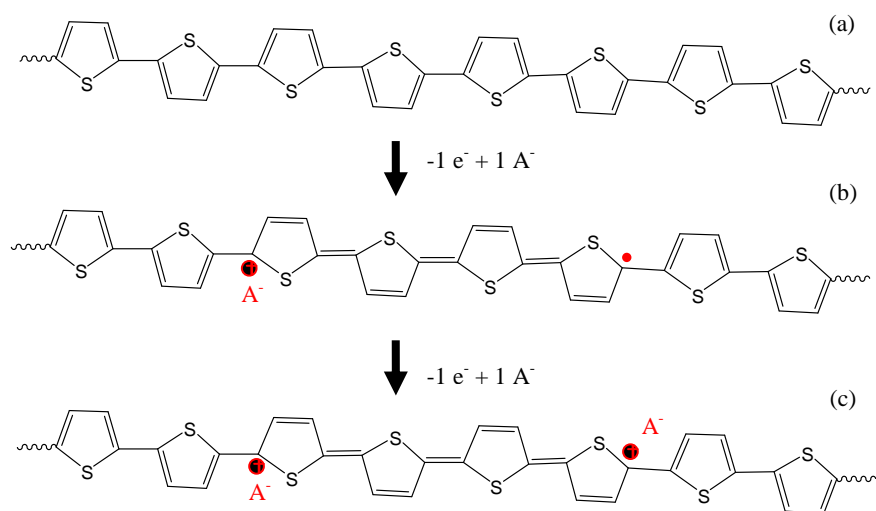


Figure 2.09: Removal of two electrons (p-type doping) from a polythiophene chain produces bipolaron. Bipolaron moves as a unit up and down the polymer chain, which is responsible to the electrical properties of conjugated polymers.

The extra electrons or holes introduced through doping behave as charge carriers. However, their delocalization motion is limited due to the existence of Coulomb attraction to their counter-ions. Since the doping process involves the charge transfer from or to the π -systems of the conjugated polymers, leaving the σ -system remain unperturbed, hence the structural properties of an individual chain is preserved. However, the optical, electronic, vibrational and other properties of the conjugated polymer are strongly affected by the doping level, especially in their conductivity counterpart (Pron & Rannou, 2002).

2.6 Optical Properties of Conjugated Polymers

The extended π -systems of conjugated polymers affect several interesting properties of these materials, including their optical properties. In conjugated polymers, it is very important to control the conjugation length. The effective conjugation length can be defined as the minimum number of bonded aromatic rings that are required to produce saturation of the physical, optical and electronic properties of the conjugated polymers (H.S. Nalwa). Let consider polythiophene as the example (as shown in Figure

2.10), the conjugation mostly depends on the overlap of π -orbitals of the aromatic rings, which requires the thiophene rings in coplanar form, and hence the conjugation length relies on the number of coplanar rings.

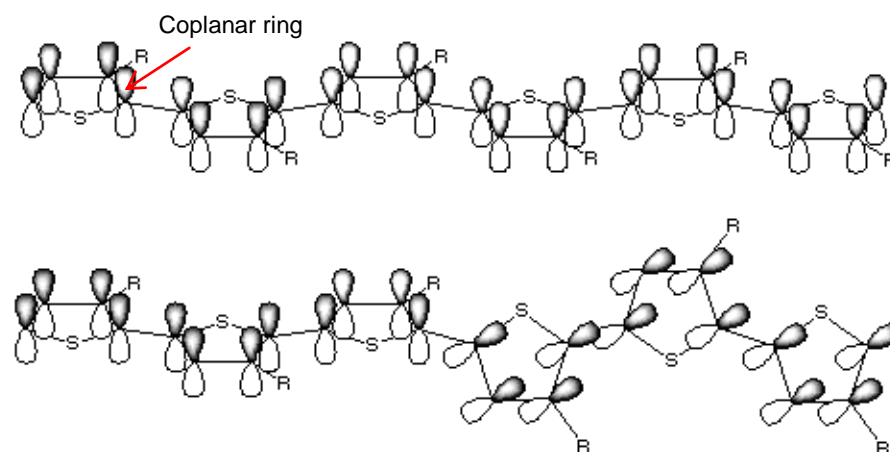


Figure 2.10: A coplanar π -orbitals polythiophene (top); a twisted substituted polythiophene (bottom) (Skotheim, et al., 1998).

Typically, conjugation length is well correlated to the energy gap and absorption wavelength. As the conjugation length increases, the separation between adjacent energy levels is reduced, and thus the absorption wavelength becomes longer, resulting in an absorption shift (Skotheim, et al., 1998). In reverse, as the conjugation length reduces, the separation between energy levels is increased, yields shorter absorption wavelength which may due to the deviation from coplanarity or twisted conjugated backbone system, as shown in Figure 2.10 (bottom). In fact, there are variety of factors may cause twisting of the conjugated backbone structure, including annealing temperature, types of solvents, the presence of bulky pendant group or dissolved ions, and application of an electric field (de Souza & Pereira, 2001; Izumi, Kobashi, Takimiya, Aso, & Otsubo, 2003)..

2.7 Donor material

2.7.1 Poly(thiophene)

Poly(thiophene) (PT) is one of the most valuable types of conjugated polymers and PT can be chemically modified to provide a wide variety of useful physical and electrical properties such as solubility, charge mobility, electrical conductivity and so on. In general, poly(thiophene) (as shown in Figure 2.11) is formed from the polymerization of thiophene monomers with a sulfur heterocycle that able to become conducting via doping process in which electrons are added or removed from the conjugated π -orbitals.

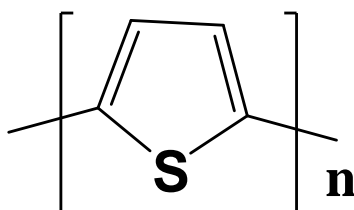


Figure 2.11: The chemical structure of monomer repeating unit of PTs.

A number of comprehensive reviews of PTs have been reported since 1981s (Street & Clarke, 1981). A detailed literature review has been published by Schopf and Koßmehl between 1990 and 1994 (Schopf & Koßmehl, 1997). Roncali reported of the electrochemical synthesis and the electronic properties of substituted PTs in 1992 and 1997, respectively (Roncali, 1992, 1997). In 1998, chemical synthesis of conducting PTs was studied by McCullough (1998). All these reviews provide appropriate guidance in preliminary PT literature from the past two decades.

I) Regioregularity

Regioregularity of conjugated polymers is one of the crucial factors to determine their higher structural order in solid state such as molecular orientation and crystallinity. Formation of good crystalline packing in conjugated polymer may provide better intra- and intermolecular ordering of polymer chains in the films, that lead to the enhancement in photons absorption and higher carrier transport, favorable for various kinds of optoelectronic device applications, as exhibited in Figure 2.12. In this sense, regioregular PTs have been explored extensively compared to the regiorandom, amorphous-based PTs (Barbarella, Bongini, & Zambianchi, 1994; Diaz-Quijada, Weinberg, Holdcroft, & Pinto, 2001).

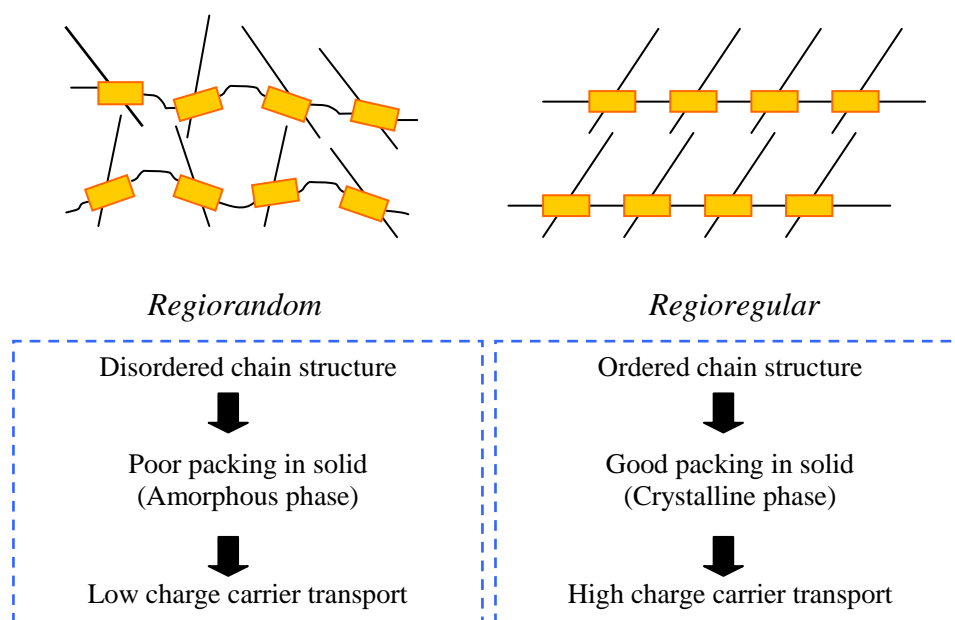


Figure 2.12: The differences between regiorandom and regioregular PTs in aspect of chain structure and charge transport characteristics.

II) Solubility

PTs as like many other polyaromatic compounds are generally insoluble in common organic solvents due to their rigid backbone structure. The lack of solution-processibility of PTs has been successfully overcome by substituting with an alkyl group at the 3 position of 2,5-thiophene ring without causing much perturbation to the

conjugated system (Pomerantz et al., 1991). In 1987, few of the examples of organic-soluble PTs were reported. Elsenbaumer et al. successfully synthesized two soluble PTs, poly(3-butylthiophene) and poly(3-methylthiophene-“co”-3'-octylthiophene) that could be spun-cast into films (Elsenbaumer, et al., 1986). Hotta et al. synthesized poly(3-hexylthiophene) and poly(3-butylthiophene) electrochemically (Hotta, Rughooputh, Heeger, & Wudl, 1987), and those polymers have been characterized in the form of solutions and cast into films (Hotta, 1987; Hotta, Rughooputh, & Heeger, 1987).

III) Regioregular Poly (3-hexylthiophene) (P3HT)

The chemical structure of P3HT is shown in Figure 2.13. Regioregular P3HT is often chosen to be promising candidate as electron donor in many research works related to its unique optoelectronic properties since it possesses the highest charge carrier mobility among all the others conjugated polymers and its hole mobility is reported as high as $0.1 \text{ cm}^2 \text{ V}^{-1} \text{ s}^{-1}$ (Zhou, Aryal, Mielczarek, Zakhidov, & Hu, 2010). The excellent charge mobility of P3HT is owing to its tendency to self-organize into ordered lamellae that leads to strong interchain interactions, and hence favor the efficient charge transport between the polysmer chains. Moreover, P3HT has good chemical stability and a low optical band gap of 1.9-2.0 eV that well matches to the strongest sunlight (Ballantyne et al., 2008; Bundgaard & Krebs, 2007). However, pure P3HT based solar cell device may limit the broad absorption profile to collect as much as photons throughout the range of solar spectrum ($\text{ca} \leq 30\%$), especially in the ultra-violet region (Bundgaard & Krebs, 2007). Moreover, the considerably high lying highest occupied molecular orbital (HOMO) level of P3HT limits the maximum open-circuit voltage (V_{oc} reaches up to $\sim 0.65 \text{ V}$) and causes oxidation instability of pure P3HT based device under ambient condition (Skotheim, et al., 1998). Hence, blending P3HT with inorganic semiconducting nanoparticles becomes the alternative route in addressing all these problems.

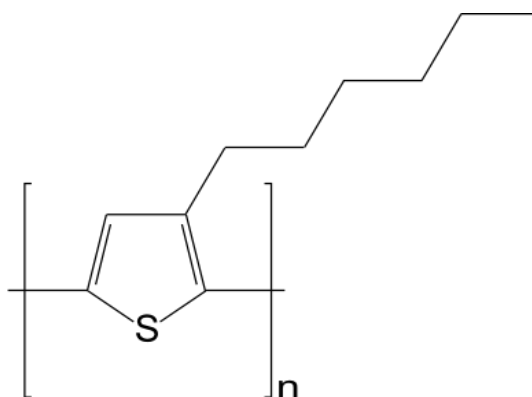


Figure 2.13: The chemical structure of P3HT

2.8 Acceptor Material

2.8.1 Inorganic Nanoparticles

In the field of materials science and nanotechnology, a particle can be defined as a small, elementary solid matter that behaves as an entire unit with its own properties. Typically, particles can be classified based on their respective geometry size, in terms of diameter. Fine particles are particles with diameter lie in nanometer range of 100-2500 nm, whereas ultrafine particles are sized between 1-100 nm (Granqvist, Buhrman, Wyns, & Sievers, 1976; Kiss, Söderlund, Niklasson, & Granqvist, 1999). The structures and shape of the inorganic nanoparticles which are widely used in hybrid polymer solar cells are depicted in Figure 2.14.

A bulk inorganic semiconductor possesses constant physical properties regardless of its size. However, an important aspect regarding to inorganic nanoparticles is the existence of quantum size effect in which their electrical as well as physical properties are altered significantly with great reduction in their size (Sato, Nakashima, Kamikura, & Yamamoto, 2008). This effect seems to be less dominant in particles size from macro to micro dimension, but it becomes pronounced when the matter size reach up to nanometer range. Nowadays, inorganic nanoparticles are of intense scientific interest since they are playing crucial role as effective bridge between the bulk material and atomic or molecular structure, which can be widely used in variety of potential

applications by varying their size and shape. Moreover, inorganic nanoparticles have larger surface area to volume ratio, which presents more area for charge transfer to take place that facilitates photovoltaic devices (S. S. Sun & Sariciftci, 2005).

Often, the inorganic nanoparticles exhibit collective behaviours. Thus, the physical properties as well as the dispersing state and the surrounding condition of the nanoparticles themselves become greatly influential. In many cases, nanoparticles appear in form of aggregates of the primary particles due to their high adhesiveness. The existing state of the nanoparticles is strongly dependent on the surrounding conditions including what types of interactions they have with the surrounding materials. The inorganic nanoparticles are seldom used by themselves, but often dispersed in other materials or blended with them. Therefore, the dispersion as well as the preparation methods of inorganic nanoparticles play important role in determining the performances of final products (Fendler & Dékány, 1996; Nogi, Naito, & Yokoyama, 2012).

Besides particle size, the shape of the inorganic nanoparticles themselves will influence the characteristic of the particle-packed bed as well. The nanoparticles shape can be studied from particles images observed using various types of microscopes such as scanning electron microscope (SEM), atomic force microscope (AFM) and transmission electron microscope (TEM). From the review of several scientific reports, it is found that one dimensional (1-D) nanorods may able to create percolated pathways in the polymer/inorganic nanoparticles blends. These pathways can improve the charge transport through the blend phase to the electrode (Huynh, Dittmer, & Alivisatos, 2002). Nevertheless, the nanorods have a tendency to lie on the plane of the films that result in inappropriate arrangement for electron transport to the cathode. Hence, some improvements in device efficiencies have been achieved by using the branched nanostructures. An efficiency of 2.2 % for solar cell consisted of dendritic CdSe

nanoparticles was reported to date by Gur et al (Gur, Fromer, Chen, Kanaras, & Alivisatos, 2007).

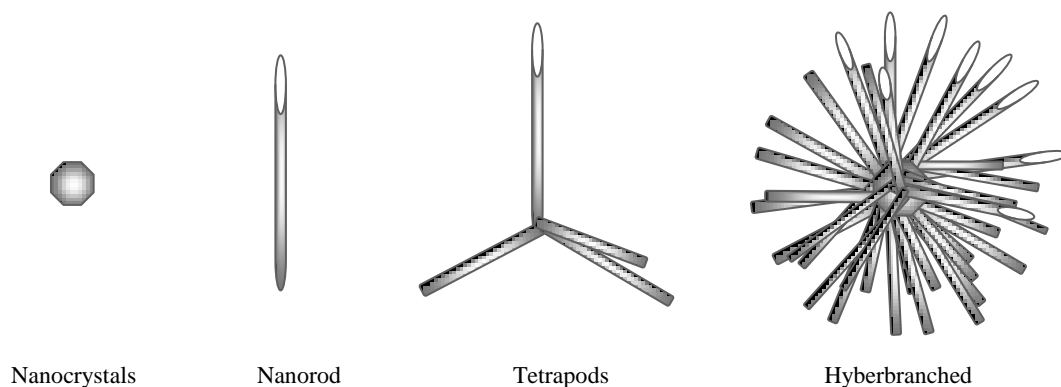


Figure 2.14: The structures and shapes of the inorganic nanoparticles that are widely used in hybrid polymer solar cells.

2.8.2 Physical Properties of Inorganic Nanoparticles

I) Optical Properties

Contrasting to the bulk materials, when inorganic materials are formed into nanoparticles, their surface area to volume ratio may increase. A smaller size of nanoparticle yields a larger specific surface area (surface area per unit mass) which leads to an increased absorption rate. By increasing the specific surface area of a nanoparticle, a corresponding increasing of significance of the physical behaviors of the surface atoms can be observed. Therefore, inorganic nanoparticles often exhibit unexpected optical properties which may be very different from their corresponding bulk counterpart since they are small enough in size to confine electron and yield quantum effects. It is reported to date that light absorption in solar cells consisted of inorganic nanoparticles is much higher than of the bulk materials (Fu & Qiu, 2011). And thus, the smaller the particle is, the higher the absorption achieved. The remarkably small size of the nanoparticles may induce quantum confinement of the photo-generated electron-hole pair, which leads to a blue shift in the absorption spectrum. Furthermore, due to the smaller size of nanoparticles than the wavelength of visible light, the light

scattering by nanoparticles become negligible, and thus higher transparency is often achieved (Nogi, et al., 2012).

II) Structural and Morphological Properties

As the atoms and molecules located at the surface of material become significant on nanometer order, and hence several structural properties of the material may drastically change such as the crystal structure of the material, lattice parameter, bond structure, atom coordination, strain, grain boundary as well as structural defects. From the morphological view point, the large specific surface area of inorganic nanoparticles is considered to be one of the crucial properties to the solubility, reactivity, sintering performance and so on of the material. Besides, the particle size may have certain effect as well to the aggregation extent and grain growth of the nanoparticles themselves according to (Nogi, et al., 2012).

III) Electrical Properties

The electronic structure of the inorganic nanoparticles may be very different than that of the bulk. When the dimensionality of the bulk semiconductor is reduced to a zero-dimensional nano-sized particle, the quasi-continuous nature of the energy dispersion of the charge carrier in the semiconductor is de-emphasized, and the discrete energy levels become dominant in the particle instead. The average spacing distance between the adjacent energy levels in an inorganic nanoparticle which also known as energy band gap is well related to the Fermi energy level of the material and the size of the nanoparticles. Due to the quantum confinement effect of charge carrier in the particle, the atomic-like electron energy levels are thereby formed which lead to a broadening of the energy band gap (or known as blue-shift) compared to that of the bulk semiconductor (Dhlamini et al., 2008; Madhusudan Reddy, Manorama, & Ramachandra

Reddy, 2003; Meulenkamp, 1998; H. Tang, Xu, Weng, Pan, & Wang, 2004), as shown in the Figure 2.15.

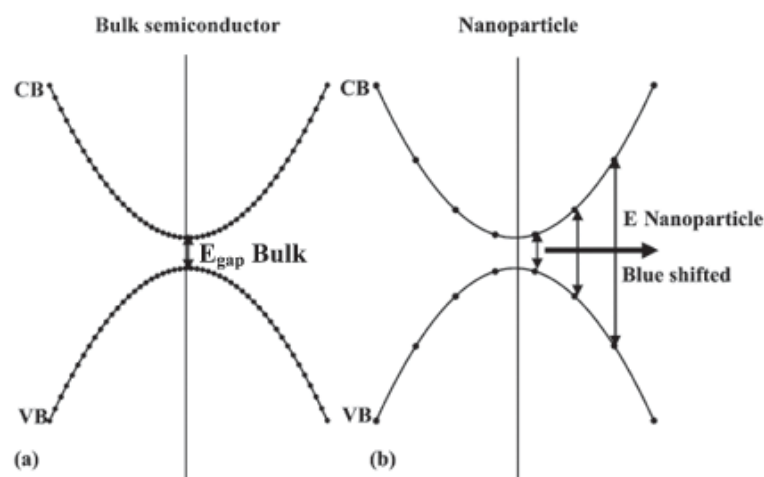


Figure 2.15: Energy dispersion for the (a) bulk semiconductor compared with that of (b) the nanoparticles (Dhlamini, et al., 2008).

2.8.3. Types of Inorganic Nanoparticles Used in This Research Work

I) Zinc Oxide

Zinc oxide is an inorganic compound with the chemical formula ZnO. It mostly appears as a white powder, known as zinc white or as the mineral zincite with very low solubility in water. Its structure is depicted in Figure 2.16. The bulk ZnO is a wide direct band gap semiconductor (E_g of ~3.0 to 3.5 eV at room temperature) of the II-VI semiconductor group of periodic table (Gupta, 1990; Lin, Cheng, Hsu, Lin, & Hsieh, 2005; Pearton et al., 2003; Srikant & Clarke, 1998; Tan et al., 2005). It exhibits n-type electrical conductivity due to its residual donors (Chiang, 2008). ZnO offers several favorable properties such as high electron mobility, wide band gap, good transparency and so on. Its usage cover a broad range of applications including light emitting diodes (Tsukazaki et al., 2005), photodetectors (Chen, Hung, Chang, & Young, 2009), solar cell devices (Senadeera, Nakamura, Kitamura, Wada, & Yanagida, 2003), gas sensor (Xu, Pan, Shun, & Tian, 2000) and so on. ZnO crystallizes in three forms, namely:

hexagonal wurtzite, cubic zinc blende, and cubic (rocksalt) structure. The wurtzite structure is found to be the most common form due to its high stability at ambient conditions whereas the rocksalt structure can only be observed at sufficiently high pressures (~ 10 Gpa) (Ozgur et al., 2005). ZnO can be further synthesized into different sorts of morphologies including nanorods, nanowires, tetrapods, nanoparticles and so on. Bulk ZnO has high electron mobility, even when measured in form of films based on ZnO nanoparticles. Electron mobility of ZnO greatly vary with temperature and able to reach up a maximum value of $\sim 2000 \text{ cm}^2 \text{V}^{-1} \text{s}^{-1}$ at temperature of $\sim 200^\circ \text{C}$ (Roest, Kelly, Vanmaekelbergh, & Meulenkaamp, 2002).

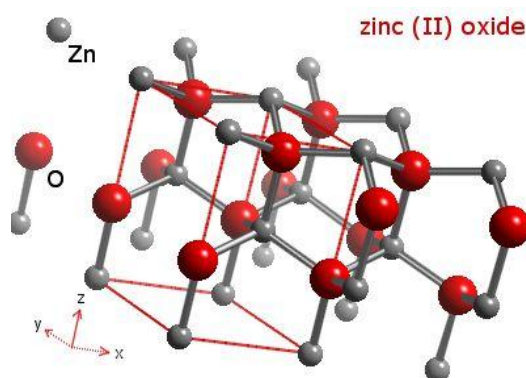


Figure 2.16: The chemical structure of ZnO.

II) Titanium Dioxide

Titanium dioxide, or sometimes denoted as titanium(IV) oxide or titania, is a naturally occurring oxide of titanium molecule with chemical formula of TiO_2 , as shown in Figure 2.17. Bulk TiO_2 may exist in nature as rutile, anatase or brookite phase, and rutile is the most common form among of them (Greenwood & Earnshaw, 1998), which is able to remain in equilibrium phase at any temperature (Banfield, Bischoff, & Anderson, 1993). The metastable anatase and brookite phases may have tendency to convert into rutile phase upon heating. Titanium dioxide has very high refractive index ($n = 2.7$), which makes it an excellent reflective optical coating for dielectric mirrors.

Besides, it can be used extensively as a good UV light absorber and capable to resist against discolouration under ultraviolet light that suitable to be applied for photovoltaic devices, catalysis and gas sensor applications as well (Paschotta, 2008).

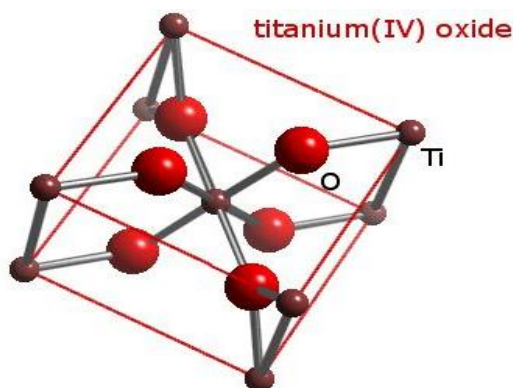


Figure 2.17: The chemical structure of TiO_2 .

III) Yttrium Oxide

The chemical formula of yttrium oxide is Y_2O_3 and its chemical structure is depicted in Figure 2.18. Y_2O_3 possess several peculiar properties. It has a higher melting point temperature of around 2430°C compared to other well-known metal oxides (Ünal & Akinc, 1996). It has a wide energy band gap ($E_g = \sim 5.0\text{--}6.0\text{ eV}$) (Andreeva, Sisonyuk, & Himich, 1994; Ivanic et al., 2001; Paumier, Gaboriaud, & Kaul, 2002), high values of electrical resistivity and electric strength of $10^8\text{--}10^9\text{ Vm}^{-1}$. It possesses a good transparency in a wide spectral range that allows little light diffusion (Andreeva, et al., 1994; Wu & Lo, 1998). Owing to all these properties, Y_2O_3 is a promising material used for antireflecting and protective coatings for mirror and for industrial components in integrated circuits (Andreeva, et al., 1994). In structural aspect, it has a cubic crystal structure with its lattice constant of 1.06 nm , which compatible to the lattice constant of silicon crystal of about 1.09 nm (Ivanic, et al., 2001)

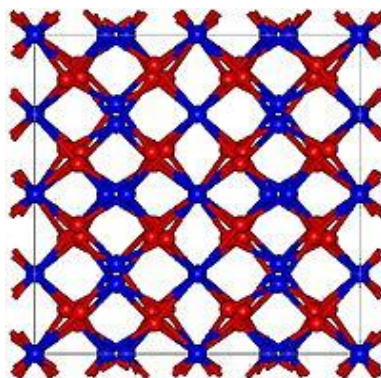


Figure 2.18: The chemical structure of Y_2O_3 .

2.9 Sol-Gel Synthesis Route:

Major efforts in synthesizing of inorganic nanoparticles can be classified into two broad areas, namely: gas phase synthesis and sol-gel processing. Inorganic nanoparticles with small size dimension (in range from 1-10 nm) with equivalent crystal structure and a high degree of monodispersity are able to be successfully processed via both gas phase and sol-gel technique. Sol-gel synthesis route is employed in order to improve the production of yield of nanoparticles. It offers many advantages such as simplicity of processing, easy control of the film deposition, cost effective and favorable for economical scale-up production (Dutta, Mridha, & Basak, 2008; Lee, Easteal, Pal, & Bhattacharyya, 2009).

This technique enables to synthesize material (typically a metal oxide) of high purity and homogeneity through a process initially take place in chemical liquid solution that acts as the precursor, which by means of involving hydrolysis and condensation reactions, leading to the formation of new phase, or so-called “sol” phase. The sol is made of solid particles with diameter of few hundreds of nm dispersed in liquid phase. Then, the particles may undergo condensation; agglomerate together forming a continuous, interconnected network extending throughout the liquid phase. The “sol” gradually evolves towards the formation of gel-like diphasic system that consisting of both liquid and solid phase with their morphologies range from distinct solid particles to

continuous chain-like polymer networks. Usually, the drying process of the gel can be achieved by means of low temperature annealing treatments (25°C–100°C) that favorable for polymer blend film deposition (Brinker, Keefer, Schaefer, & Ashley, 1982; Klein & Garvey, 1980). However, there are several parameters need to be considered seriously, such as the sol concentration (Dutta, et al., 2008; Kim, Tai, & Shu, 2005; O'Brien, Koh, & Crean, 2008), annealing temperature and time (Ghosh, Paul, & Basak, 2005; Musat, Teixeira, Fortunato, Monteiro, & Vilarinho, 2004; Zhu, Gong, Sun, Xia, & Jiang, 2008), substrate used (Chakrabarti, Ganguli, & Chaudhuri, 2004; Ghosh, Basak, & Fujihara, 2004) and film thickness (Aslan, Oral, Menşur, Gül, & Başaran, 2004; Mridha & Basak, 2007), which may greatly affect the properties of the resultant sol-gel itself.

2.10 Hybrid Polymer Solar Cells

Organic solar cell is a sort of photovoltaic device that based on conductive organic materials such as semiconducting (conjugated) polymer and small organic molecules. In recent years, a broad range of organic solar cells technology are being developed, using p-type conjugated polymers, in combination with either n-type polymer or with fullerenes. One alternative approach is a new generation of organic solar cells, so called the hybrid polymer solar cells which based on the mixture of both organic and inorganic semiconductors. Hence, they combine the unique properties of the organic or polymeric materials with the inorganic nanoparticles, such as solution-processibility of conjugated polymer and high electron mobility of inorganic semiconductors (Elif Arici et al., 2003). There are various kinds of hybrid polymer solar cells have been reported to date, using CdSe (Huynh, et al., 2002; B. Sun, Marx, & Greenham, 2003), TiO₂ (Kwong et al., 2004), ZnO (Beek, Wienk, Kemerink, Yang, & Janssen, 2005), PbS (McDonald et al., 2005), CuInS₂ (E. Arici, Sariciftci, & Meissner, 2003) and CuInSe₂ (E. Arici et al., 2004). Besides of cheaper fabrication, this solar cell

technology offers other attractive features, including excellent mechanical flexibility, processability and tunability of the optical band gap of the materials.

A schematic diagram of the structure of hybrid solar cell is depicted in Figure 2.19. Typically, a hybrid solar cell consists of at least four distinguishable layers. It has a transparent anode as the front electrode which allows light to pass through it. Indium tin oxide (ITO) coated glass substrate is popular anodic material due to its high transparency and wide availability with different resistivity in commercial market. Next, a layer of conductive polymer mixture of PEDOT:PSS may be favorably deposited between anode and the photoactive layer. The PEDOT:PSS works in different functions, including to serve as hole transporter, to smoothen the rough surface of ITO layer, to shield the photoactive layer from oxygen and moisture attack, and keeps the anodic material from diffusing through the photoactive layer (Huang et al., 2005; Skotheim, et al., 1998). Right after the PEDOT:PSS, an photoactive layer consisting of a blend of conjugated polymer and inorganic nanoparticles is deposited on top of it, which responsible for light absorption, exciton generation and dissociation, and charge carrier diffusion. The back electrode (cathode), usually made of aluminium (Al), silver (Ag), calcium (Ca), and gold (Au) is coated onto the photoactive layer.

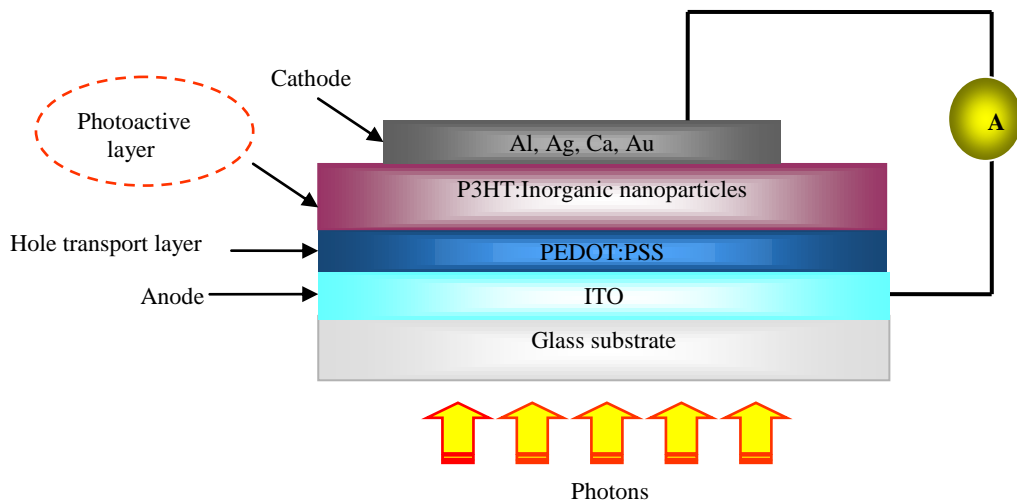


Figure 2.19: Schematic structure of hybrid solar cell.

2.10.1 Basic Working Principles of Hybrid Solar Cells

For hybrid solar cell, five important processes are involved to generate photocurrent, as depicted in Figure 2.20 (N. S. Sariciftci, Smilowitz, Heeger, & Wudl, 1993):

- 1) Photon absorption
- 2) Electron excitation from HOMO to LUMO
- 3) Exciton diffusion across the donor (D)/acceptor (A) interface
- 4) Exciton dissociation and charge transfer from Donor to Acceptor
- 5) Charge collection at respective electrode

Upon photon ($h\nu$) absorption within the photoactive layer, an electron is excited from HOMO to the LUMO of the donor material. A bound electron-hole pair, so called the exciton is therefore created. The excitons diffuse within their lifetime in their diffusion length, which is typically limited to 5–20 nm (Halls, Pichler, Friend, Moratti, & Holmes, 1996). If the exciton does not dissociate into its component electron and hole, it will tend to recombine by emitting photon or decaying via thermalization (or so-called the non-radioactive recombination). Thus, an efficient exciton dissociation mechanism is needed by overcoming the exciton binding energy which ranging from 0.1-1.0 eV (Pope & Swenberg, 1999; N.S. Sariciftci, 1997). Subsequently, the dissociated electron will be transferred to the LUMO of the acceptor, resulting in an extra electron on the acceptor and leaving a hole in the donor. The driving force which required for facilitating the charge transfer is the difference in ionization potential I_D of the donor and the electron affinity E_A of the acceptor, minus the coulombic binding energy of the exciton (N. S. Sariciftci, Smilowitz, Heeger, & Wudl, 1992). The photogenerated charges are then transported and collected at the respective electrode before they recombine. When all these processes continue, a photocurrent will be

generated. In the means to obtain optimum power conversion efficiency, a fast charge-transfer process and longer lifetime of charge-dissociated state are preferred.

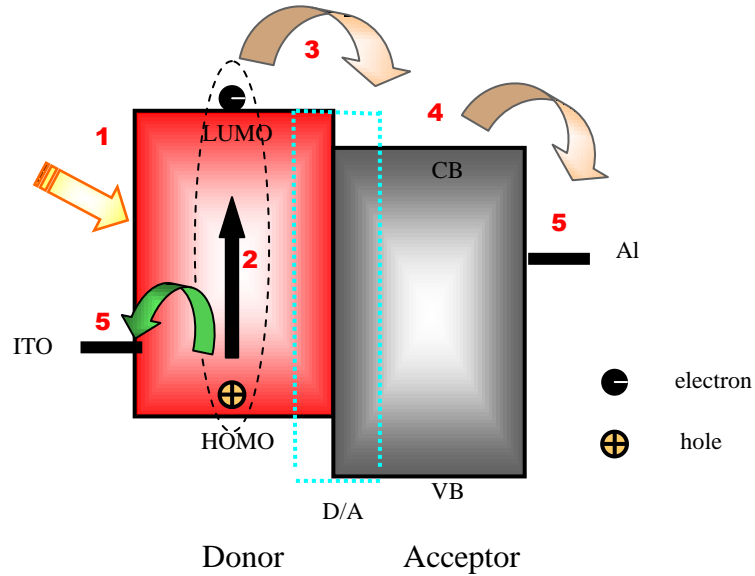


Figure 2.20: The working principle of hybrid polymer solar cell consisting of an electron donor and acceptor pair.

2.10.2 Key Parameters of the Hybrid Solar Cells

The current density-voltage curve (J-V curve) is used to characterize a hybrid solar cell as illustrated in Figure 2.21. The solar cell exhibits a diode behavior under dark condition. As the cell is illuminated by a light source, the J-V curve shifted down and the short-circuit current density (J_{sc}) is defined as the current density which crosses the cell at zero applied voltage. The open circuit voltage (V_{oc}) is measured when the current density in the cell turns to zero. The maximum power point, P_{max} (or defined as P_{out}) is determined when the product between the current density, J_{max} and the voltage, V_{max} is the maximum value. To obtain the power conversion efficiency of a solar cell, this power is compared with the power of incident light, P_{in} . The power conversion efficiency (PCE) is:

$$\eta_{power} = \frac{P_{out}}{P_{in}} = \frac{J_{max} V_{max}}{P_{in}} = \frac{FF \times J_{sc} V_{oc}}{P_{in}}$$

where fill factor (FF) is defined as:

$$FF = \frac{V_{\max} J_{\max}}{V_{oc} J_{sc}}$$

All these four quantities, J_{sc} , V_{oc} , η and FF are the key parameters for a solar cell and have to be determined under particular illumination condition, which is so-called the standard test condition (STC). Under STC, a room temperature of 25°C and a white light irradiance of 100mWcm⁻² with an air mass 1.5 spectrum are specifically set up (Testing & Materials, 2002).

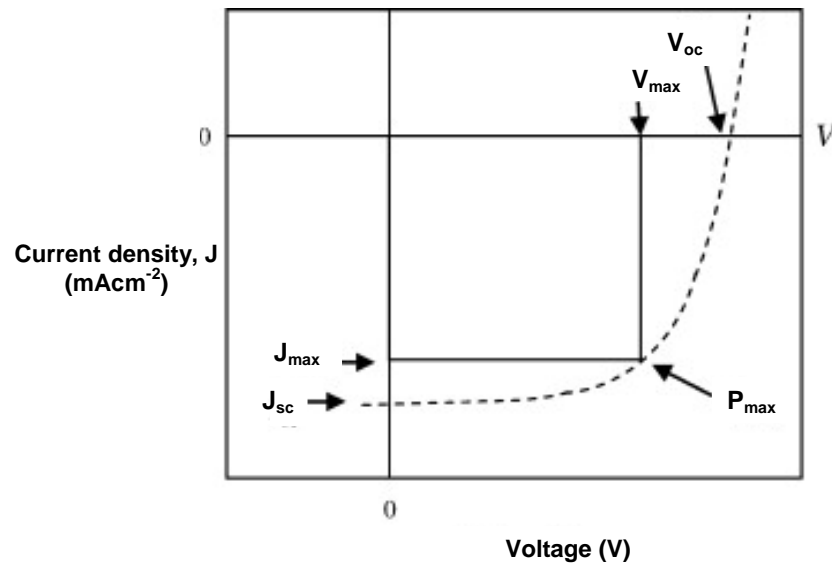


Figure 2.21: The current density-voltage curve (J-V curve) of a hybrid solar cell under illuminated condition (dash line).

2.10.3 Types of Device Architectures for Organic Solar Cells

In order to improve the charge transport within the organic solar cell, several kinds of device architectures based on different types of junctions have been developed. Further explanations of the types of junctions are elaborated as below:

I) Single Layer Organic Solar Cell

A single layer cell consists of one single semiconducting material which is sandwiched between two metallic electrodes of different work functions. The basic structure of such a cell is depicted in Figure 2.22(a). It is sometimes referred to a Schottky type device as the charge separation takes place at the Schottky junction (rectifying junction) with one electrode. Another electrode interface is supposed to behave as ohmic behaviour in nature. In Figure 2.22(b), the situation for the case of a Schottky junction built between the electrode with lower work function and organic semiconducting layer is figured out. A band bending from the Schottky contact lies in the depletion region as depicted, which corresponds to a built-in electric field arising from the difference in work functions that is required for exciton dissociation. Upon light illumination, the exciton will be separated and the free charge carriers will transport to the respective electrodes. However, a light absorption covering the whole visible range is rare based on the merely single type of material. Photogenerated excitons can only be dissociated within the depletion regions that seriously limit the exciton diffusion length. Since both positive and negative charges may travel through the thin photoactive region, recombination losses are therefore relatively high, resulting in low power conversion efficiency (Shrotriya, 2010). Such a cell is preferably suitable to be used for screening and evaluation purposes, rather than photovoltaic application (International, 2004). To address these problems, bilayer and bulk heterojunction solar cells have been developed.

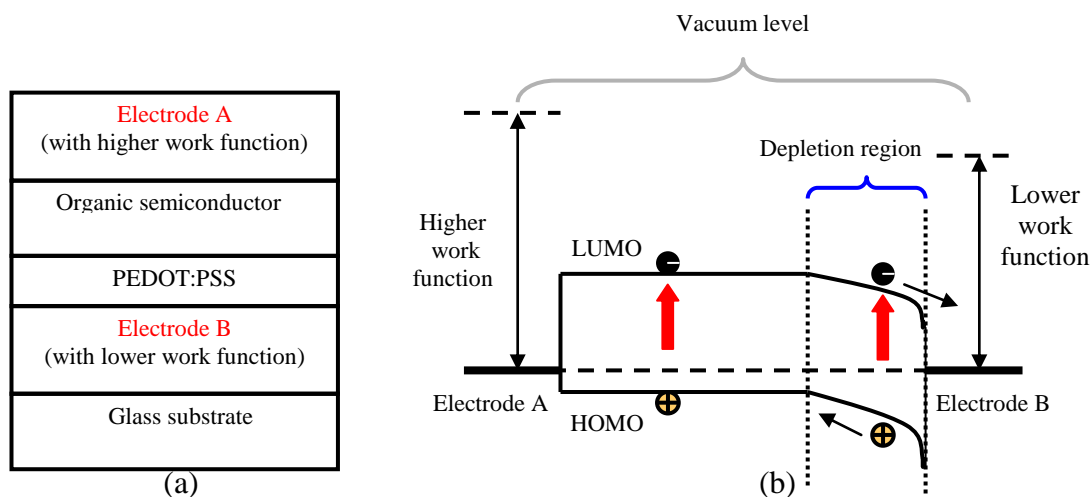


Figure 2.22: (a) The basic structure of a single layer solar cell. (b) Schematic of a single layer solar cell with a Schottky contact at the lower function electrode B contact. Photogenerated excitons can only be dissociated within a narrow depletion layer, and thus the device is exciton diffusion limited.

II) Bilayer Solar Cell

In a bilayer solar cell, two layers of materials which differ in electron affinity and ionization energy, typically one is an electron donor and the another is electron acceptor are stacked together with a planar heterojunction interface (C. W. Tang, 1986), as depicted in Figure 2.23(a). The bilayer material is sandwiched between two electrodes which are well-match to the HOMO level of donor and the LUMO level of acceptor for efficient charge extraction. Hence, a large potential drop between donor and acceptor is generated to enable the charge separation to occur at the interface. The structure is schematically depicted in Figure 2.23(b), in which all sorts of band bending effects are negligible due to the energy level alignment. A big advantage of this cell over single layer solar cell is the monomolecular charge transport. Saricffici et al. reported a C₆₀:MEH-PPV bilayer solar cell has achieved a device efficiency of 0.04 % under monochromatic illumination (N. S. Sariciftci et al., 1993). Since the diffusion length of exciton in organic material is on the order of 10 nm, the photoactive layer thickness need to be in the same range with the length as well. Nevertheless, for a

polymer film, a layer thickness of at least 10 nm is required to maximize the light absorption. At such a large extent of thickness, only excitons that are able to reach the interface are successfully dissociated, and thus the photocurrent generation is limited. To deal with this critical issue, a new type of heterojunction solar cell is developed, which is so-called the disperse bulk heterojunction organic solar cell.

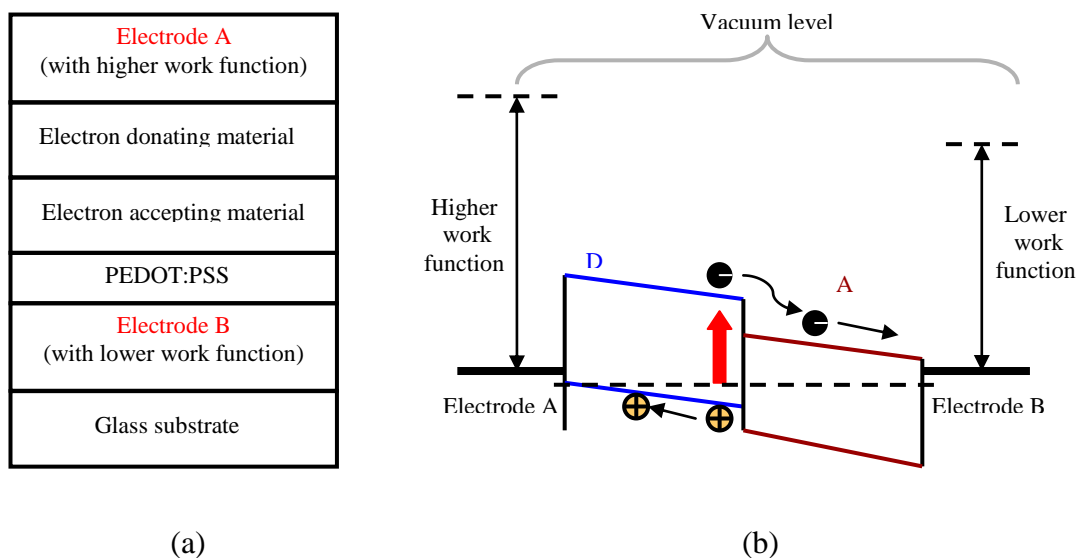


Figure 2.23: The basic structure of a bilayer solar cell. (b) Schematic of a bilayer heterojunction solar cell. The donor (D) contacts the higher work function electrode A and the acceptor (A) contacts the lower work function electrode B, in order to achieve charge carrier collection, respectively. Excitons can only be dissociated within the region at the D/A interface.

III) Bulk Heteronjunction (BHJ) Solar Cell

For BHJ solar cell, the donor and acceptor components are intimately mixed together in a bulk volume, in which the acceptor molecules are well dispersed throughout the entire donor phase, forming dispersed heterojunctions as depicted in Figure 2.24(a). This type of cell is similar to bilayer solar cell in the sense of donor/acceptor (D/A) concept application, but it exhibits larger interfacial area where charge separation occurs due to the dispersed heterojunctions. For such a cell, D/A interface is built within the distance less than the exciton diffusion length of each site. Most of the excitons generated in either material may be able to reach the interface, within

their life time, produce efficient exciton dissociation yield (Halls et al., 1995; Yu, Gao, Hummelen, Wudl, & Heeger, 1995; Yu & Heeger, 1995). In Figure 2.24(b), the situation for BHJ solar cell is depicted, again neglecting all kinds of energy alignments and band bending effects. The cell provides percolated pathways for both electron and holes to reach their respective electrode more efficiently, by forming bi-continuous and interconnecting D and A phases. Hence, recombination losses can be reduced intensively and result in higher photocurrent production. It was reported to date that an power conversion efficiency of 5.2 % has been obtained for BHJ device based on P3HT and fullerene derivative (Ko, Lin, Chen, & Chu, 2007). However, BHJ solar cells require sensitive control over the nanoscale morphology of each material. There are a variety number of processing parameters that may remarkably affect the formed BHJ structure, including choice of materials, choice of solvents used, blend composition and so on. Thus, parameters optimizations need to be addressed properly so that highly performed solar cell devices can be developed.

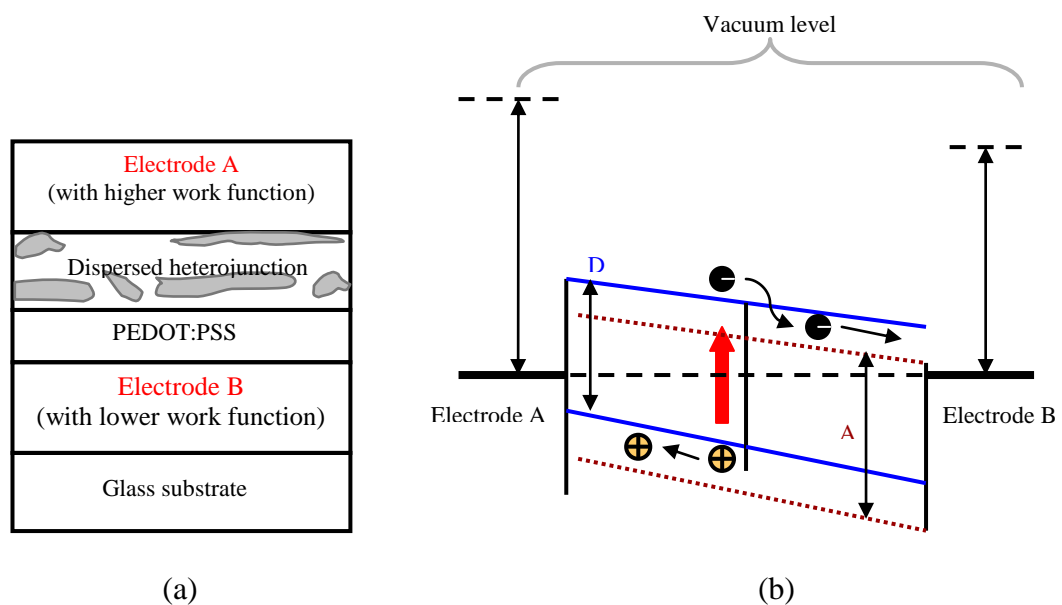


Figure 2.24: (a) The basic structure of a bulk heterojunction solar cell. (b) Schematic of a bulk heterojunction solar cell device. The excitons can be dissociated throughout the volume of material as the D is well blended with A.

CHAPTER 3

EXPERIMENTAL METHODOLOGY

3.1 Overview

This chapter explains the experimental methodology involved in this research work. The thin films preparation and device fabrication will be explained in this chapter, beginning from preparing the chemical solutions to deposit them onto different clean substrates. The spin-coating technique is basically used to fabricate the active layer of hybrid solar cells. Besides, this chapter also explains several characterization methods employed in this work, including the utilizing of UV-VIS-NIR spectrophotometer, surface profilometer, X-ray diffraction (XRD), atomic force microscopy (AFM), field-effect scanning electron microscopy (FESEM), and photovoltaic characterization using Keithley 236 Source Measurement Units (SMUs) under AM1.5 G-filtered white light irradiation with a power intensity of 100 mWcm^{-2} from Oriel 67005 solar simulator.

3.2 Chemicals and Materials

To get started with the study of thin films and hybrid solar cells consist of P3HT:inorganic compound, a number of chemicals and materials are required to be in hand. These include the organic materials, several types of inorganic compounds, solvents, substrates as the base for thin film deposition and the appropriate electrodes for device fabrication. The procedures used for preparing the chemical solutions derived from as-purchased materials and sol-gel synthesis route as well as the substrates and electrodes preparation and cleaning processes are explained in the sub-sections of 3.2.1, 3.2.2, and 3.2.3.

3.2.1. Chemicals and Solutions Preparation

I) P3HT:As-Purchased Inorganic Nanoparticles Blends:

Before producing the thin film, the sample solution has to be well prepared. Both donor regioregular poly(3-hexylthiophene) (P3HT) and acceptor inorganic metal oxides in nanoparticles forms (ZnO , TiO_2 and Y_2O_3), with particle size less than 100 nm are purchased from Sigma Aldrich. The masses of P3HT powder and inorganic compounds are measured using a weighing machine. Blend solutions with different compositions of both components are then prepared in chloroform (CHCl_3) with a solution concentration of 10mgml^{-1} . Up to date, chloroform is one of the non-aromatic solvents that capable for providing a good solubility for P3HT based compounds (Siraj, 2012). Next, the solutions are vigorously stirred for at least 24 hours at room temperature to maximize blending capability. Table 3.1 tabulates the blends composition and the masses of the materials dissolved in 1 ml chloroform solvent. Figure 3.01 shows the photograph of the pristine solutions and the P3HT:inorganic nanoparticles blend solutions.

Table 3.1: Blend compositions and the respectively masses of P3HT:inorganic nanoparticles blends.

Materials	Composition	Mass ($\text{mg}\pm 0.1$)
P3HT + inorganic nanoparticles (XO^*) in chloroform solvent	P3HT + 0 % XO	P3HT = 10.0, XO = 0.0
	P3HT + 1 % XO	P3HT = 9.9, XO = 0.1
	P3HT + 2 % XO	P3HT = 9.8, XO = 0.2
	P3HT + 3 % XO	P3HT = 9.7, XO = 0.3
	P3HT + 4 % XO	P3HT = 9.6, XO = 0.4
	P3HT + 5 % XO	P3HT = 9.5, XO = 0.5
	P3HT + 10 % XO	P3HT = 9.0, XO = 1.0

XO^* = either any types of the chosen inorganic metal oxides in nanoparticles forms, namely ZnO , TiO_2 and Y_2O_3 .

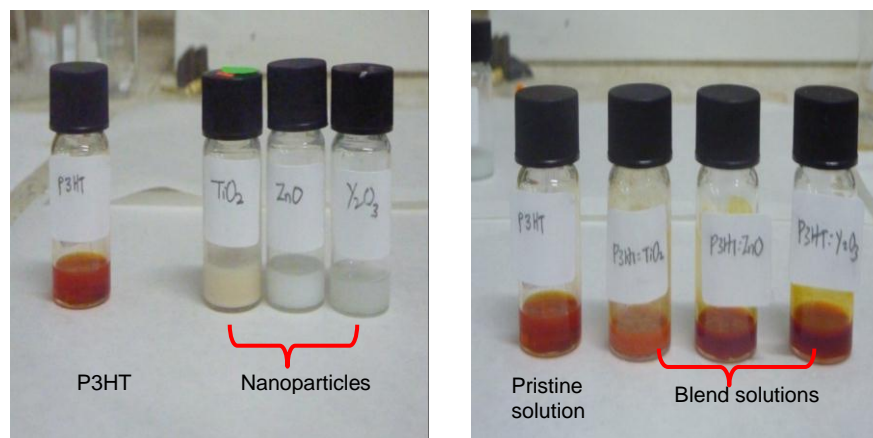
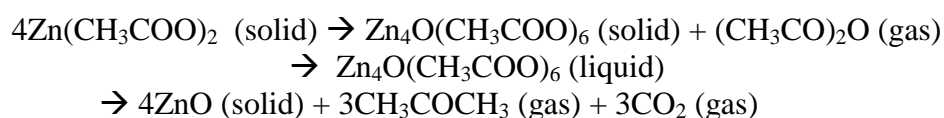


Figure 3.01: Pristine solutions and the P3HT:inorganic nanoparticles blend solutions.

II) P3HT:As-Synthesized Sol-gel ZnO Blend Solutions:

In the synthesis of ZnO crystals, zinc acetate dihydrate, ethanol and diethanolamine (DEA) are used as the starting materials, solvents and sol stabilizers, respectively. High purity zinc acetate dihydrate ($\text{Zn}(\text{CH}_3\text{COO})_2 \cdot 2\text{H}_2\text{O}$, 99.0%) and DEA [$\text{HN}(\text{CH}_2\text{CH}_2\text{OH})_2$] are purchased from Sigma-Aldrich. Zinc acetate dehydrate is preferred to be used in sol-gel route due to its unique property as a source of both zinc and oxygen which is known to be a “mono-precursor” (Wójcik, Godlewski, Guziejewicz, Minikayev, & Paszkowicz, 2008). Being a “mono-precursor” means that the material does not require an oxygen precursor to grow ZnO since the zinc acetate dihydrate itself may decompose to produce ZnO. This chemistry reaction mechanism is shown as below (Wójcik, et al., 2008)]:



To synthesize the ZnO, approximately 0.4 g of zinc acetate dehydrate is first mixed with 25 ml ethanol ($\text{C}_2\text{H}_5\text{OH}$) in a vial so as to prepare a sol precursor with concentration of 0.75 M. Then, an appropriate quantity of DEA is added drop by drop into the solution until it turned from milky to transparent color. This DEA is used as a sol stabilizer and to ensure a good solubility of zinc acetate in organic medium (Zhou,

Zhao, Ren, Song, & Han, 2011). The molar ratio of DEA to zinc acetate dehydrate is maintained at 1:2. Next, the procedure is followed by a thorough stirring process via ultra-sonication at 60 °C for 30 minutes, and then it is again stirred for 2 hours at room temperature using magnetic stirrer in order to yield a clear, homogenous ZnO sol. To ensure a better stability of the as-synthesized sol, it is required to be aged for at least one day (Hayat, Gondal, Khaled, Ahmed, & Shemsi, 2011). Finally, blend solutions with different sol contents are prepared by adding different volumes of sol from the as-synthesized sol precursor (e.g., 0.05 ml, 0.1 ml, 0.2 ml and 0.3 ml) into several vials consisting of chloroform-based P3HT solutions (each concentration is set at 10 mgml⁻¹). Table 3.2 lists the five different sets of blend compositions and Figure 3.02 shows the photographs of P3HT:sol-gel ZnO blend solutions.

Table 3.2: Blend compositions of P3HT:sol-gel ZnO.

Solutions	P3HT concentration (mgml ⁻¹)	Amount of ZnO sol precursor added into P3HT solution (ml)
P3HT + sol-gel ZnO in different compositions	10.00 mgml ⁻¹	0.00
		0.05
		0.10
		0.20
		0.30

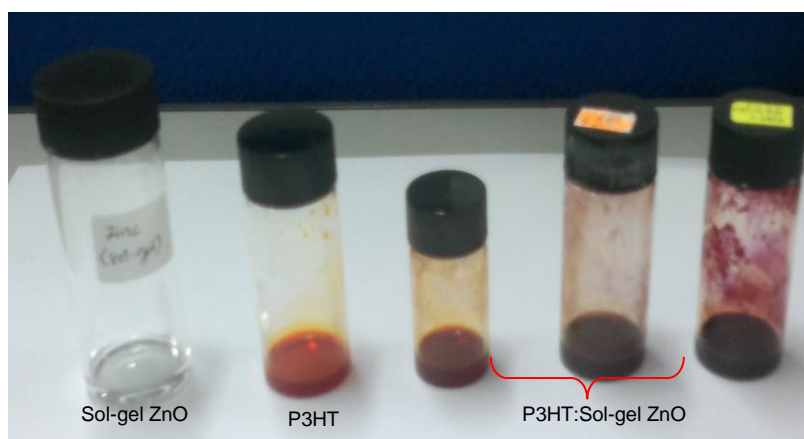


Figure 3.02: P3HT:sol-gel ZnO blend solutions.

3.2.2 Substrates and Electrodes Preparation

The substrates used for the purpose of thin film characterization in this work are quartz and glass substrates, while that utilized for the solar cell device fabrication is indium tin oxide (ITO) coated glass substrate. Glass substrates are employed in X-ray diffraction (XRD), atomic force microscopy (AFM) and field-effect scanning electron microscopy (FESEM) measurements, whereas the quartz substrates are utilized in optical characterization due to its higher transparency and feasibility to probe absorption properties of the films in the ultraviolet wavelength region compared to that of the glass substrates (Guzzi et al., 1992). All these substrates are purchased from H. W. Sands Co., Ltd. The substrates are required to be cut and patterned according to the desired size, dimension and shapes prior to substrates cleaning and thin film deposition procedures. In this work, the prepared substrates are cut out into pieces of 2.5 cm × 2.0 cm (length × width) rectangular dimension using diamond glass cutter.

For the device fabrication, a transparent anode of ITO electrode and an opaque cathode electrode of Al are usually required. Both types of electrodes are convenient to offer low-cost hybrid solar cells fabrication due to their wide availability in markets and their excellent electrical properties. The as-purchased ITO electrode with a sheet resistance of $\approx 10 \Omega \text{sq}^{-1}$ (for the ITO coated layer side) is highly conductive and provides excellent transparency of >90% to allow the illuminated light to pass and to reach into the photoactive thin film readily (Pandey & Samuel, 2010).

3.2.3 Substrates Patterning and Cleaning

Cleaning the substrates prior to thin film deposition is required to be accomplished properly in order to erase any residual contamination from the surface of the substrates. However, in the case of ITO substrate, a specific patterning procedure by etching a desired portion of the substrate area before cleaning is required in order to

avoid the risk of short-circuit between the positive and negative contacts of the device through the photoactive film. In this work, an approximately $\frac{1}{5}$ of the ITO area is covered by nail polish (see Figure 3.03) and the unwanted conductive area is etched using hydrochloric acid (HCl) solution at an annealing temperature of $\approx 90^{\circ}\text{C}$ for 20 minutes.

The cleaning procedure is different and depends on the types of substrates. For quartz and glass substrates, firstly, the substrates are immersed in DECONTM foam solution which has been diluted with deionised water. Later, they are sonicated in ultrasonic bath for 10 to 15 minutes to remove foam from the substrates. After that, they are rinsed using deionised water, acetone solution, ethanol solution, and then rinsed again in the deionised water sequentially in order to erase off the traces of organic substances, chemical solutions, oil and dirt. Lastly, the cleaned substrates are dried using nitrogen gas flow. However, for the etched ITO substrates, they are initially immersed in acetone for 10 to 15 minutes in ultrasonic bath to remove the traces of nail polish and then rinsed with deionized water to remove the acetone residuals. Next, the substrates are immersed in isopropanol to further remove any organic substances and contaminant from the substrates. Before drying with nitrogen gas, the substrates have to be rinsed again with deionized water.

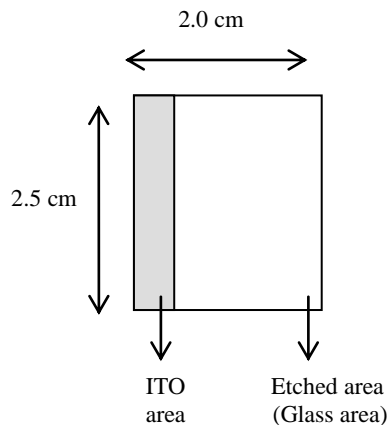


Figure 3.03: ITO substrates patterning.

3.3 Thin Films Preparation via Spin Coating Technique

Spin coating technique is one the most common and convenient techniques to produce uniform thin films of well-controlled thickness. It is a solution processed method which is suitable for organic thin film deposition as it does not require elevated temperature that might cause the organic substances to decompose upon heating compared to thermal evaporation method. In this work, a model of WS400B-6NPP-Lite spin coater processor is used to deposit the film layers (see Figure 3.04). The film thickness is well controlled by the spin speed and spin time. For thin film fabrication, the spin speed and spin time are set at 2000 rotations per minute (rpm) and 30 seconds, respectively. The accelerator is set at the maximum state in order to ensure that the spin speed is started at the required speed. Several steps involved in this spin coating process (Meyerhofer, 1978) are illustrated in Figure 3.05.

Firstly, a cleaned substrate is placed at the centre of the disk plate. There is a small hole at the centre of the plate which serves as a vacuum chuck to firmly hold the substrate. Hence, the substrate does not randomly move away when the disk plate is spinning. Thereafter, a quantity of chemical solution (about 100 μ l) is deposited onto the substrate. When the vacuum is switched on and start button is pressed, the disk plate begins to spin at the required speed. After 30 seconds, the vacuum is switched off and the sample is taken off. Lastly, the film is dried in an oven under room temperature for few hours to ensure that the residual solvent has been completely evaporated. Later, the film is taken for further experimental steps and/or characterization measurements.

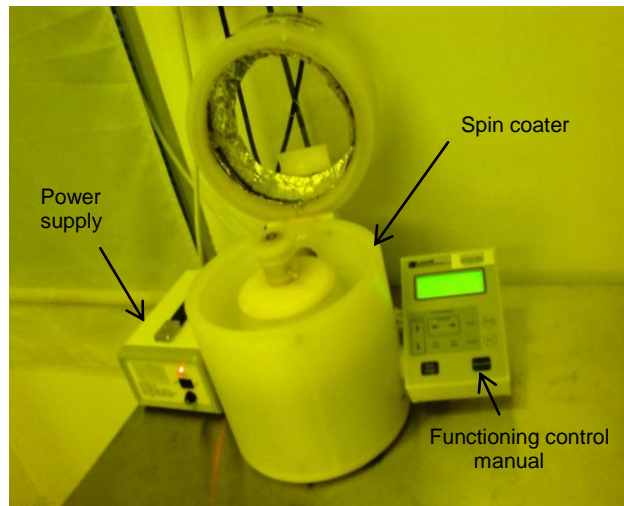


Figure 3.04: The spin coating machine which is used for thin films deposition.

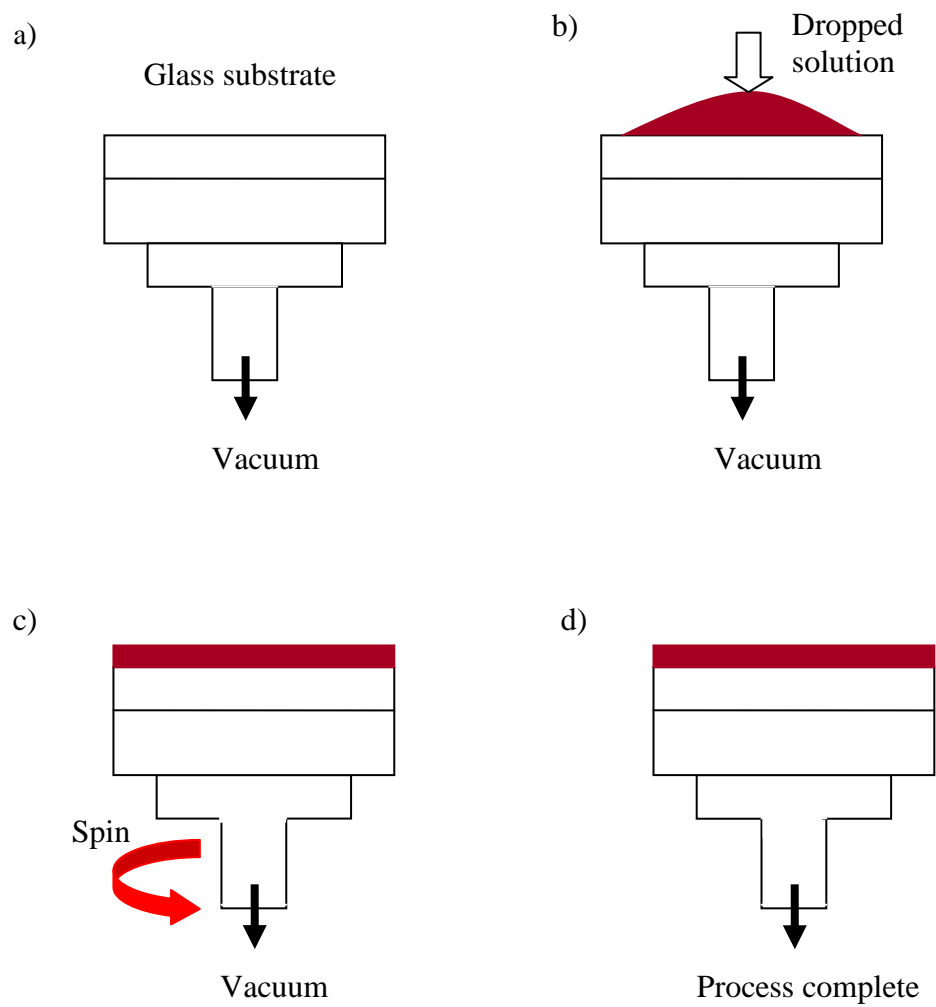


Figure 3.05: Schematic representation of the spin coating technique.

3.3.1 P3HT:ZnO Sol-Gel Films Preparation via Thermal Annealing Treatment

For the films derived from sol-gel route, they are required to be thermally annealed under a certain range of temperature before taken out for characterization measurements. This is to allow the complete formation of ZnO through decomposition of zinc acetate dehydrates and to determine the optimum annealing temperature (Ivanova, Harizanova, Koutzarova, & Vertruyen, 2010). Figure 3.06 shows the flow chart of the preparation of P3HT:sol-gel derived ZnO films.

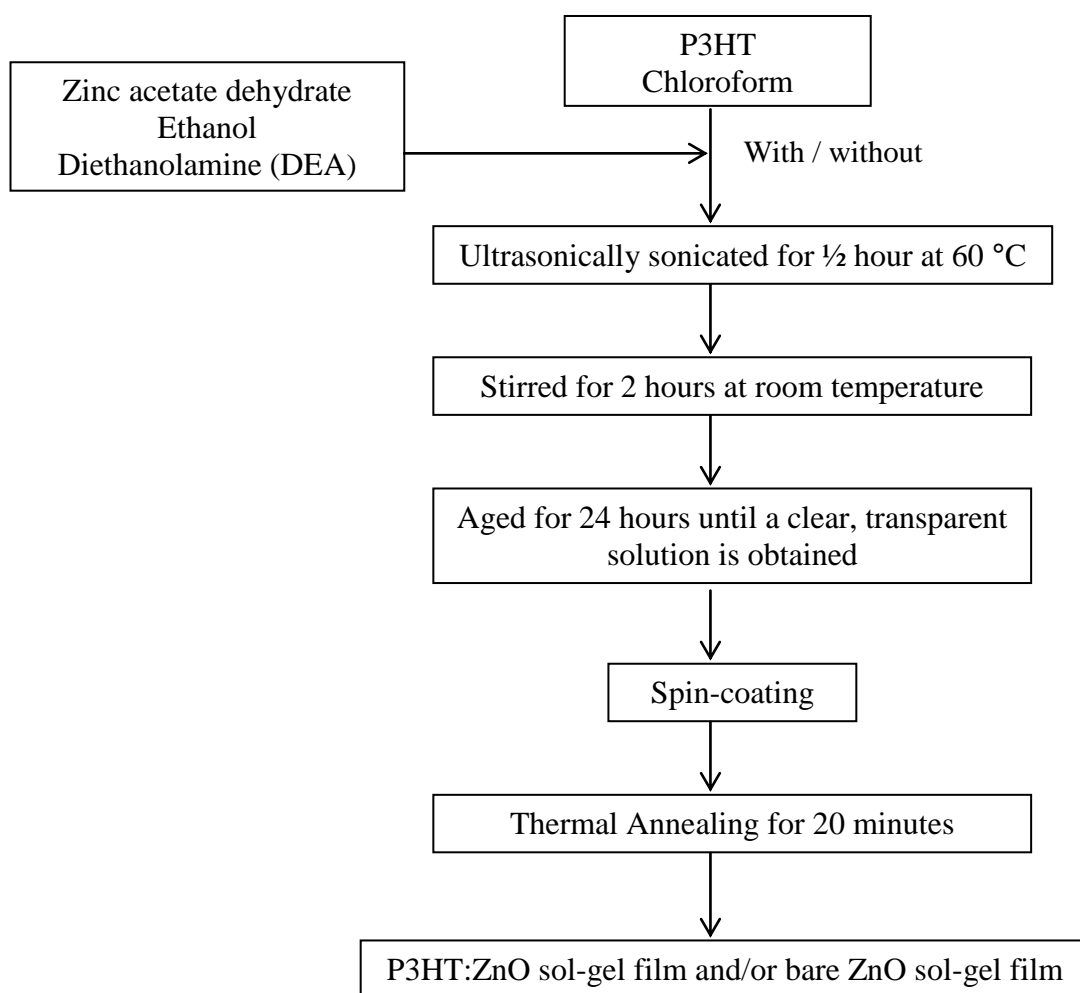


Figure 3.06: The flow chart for the preparation of the P3HT:sol-gel ZnO films.

3.4 Devices Fabrication

In the previous sections, the methodology of chemicals, solutions, substrates, ITO electrodes preparation, substrate patterning and cleaning, together with the thin film preparation procedure via spin-coating technique have been demonstrated. This section will describe briefly the fabrication procedure for solar cell devices based on different types of materials and a variety of processing parameters.

3.4.1 Single Layer and Bulk Heterojunction (BHJ) Structures

The design of the single layer and bulk heterojunction structure solar cell devices are in the form of a sandwich structure of the photoactive thin film between an anode electrode of ITO and a metal cathode of aluminum (Al). The device construction of ITO/PEDOT:PSS/photoactive thin film/Al is therefore formed. The hole transporting material, poly(3,4-ethylenedioxythiophene):poly(styrenesulfonate) (PEDOT:PSS) is purchased in solution form (H. C. Starck, Baytron P VPAI 4033). Before the thin film deposition, the PEDOT:PSS is spin-coated on top of the patterned ITO at a spin speed of 7000 rpm for 20 seconds. Then, it is baked at temperature of 110 °C for 20 minutes in order to reduce the roughness of ITO surface (Huang et al., 2005). After that, the thin film is deposited above the PEDOT:PSS layer via spin-coating technique at speed of 2000 rpm for 30s. Lastly, Al electrodes (≈ 100 nm) are thermally evaporated onto the films under vacuum condition at a pressure of 10^{-5} mbar through a designed shadow mask to produce an active area of 0.10 cm^2 ($0.02 \text{ cm} \times 0.05 \text{ cm}$).

For comparison with P3HT:ZnO devices, hybrid systems consisting of different types of as-purchased inorganic metal oxide nanoparticles (TiO_2 and Y_2O_3) as well as sol-gel derived ZnO are fabricated and investigated. To further enhance the devices performance, an additional insertion of n-type ZnO buffer layer with different thickness on top of the P3HT:ZnO sol-gel derived film is also employed. The device construction

of the single layer and BHJ solar cells based on different device geometries and hybrid systems are schematically illustrated in Figure 3.07((a)-(d)).

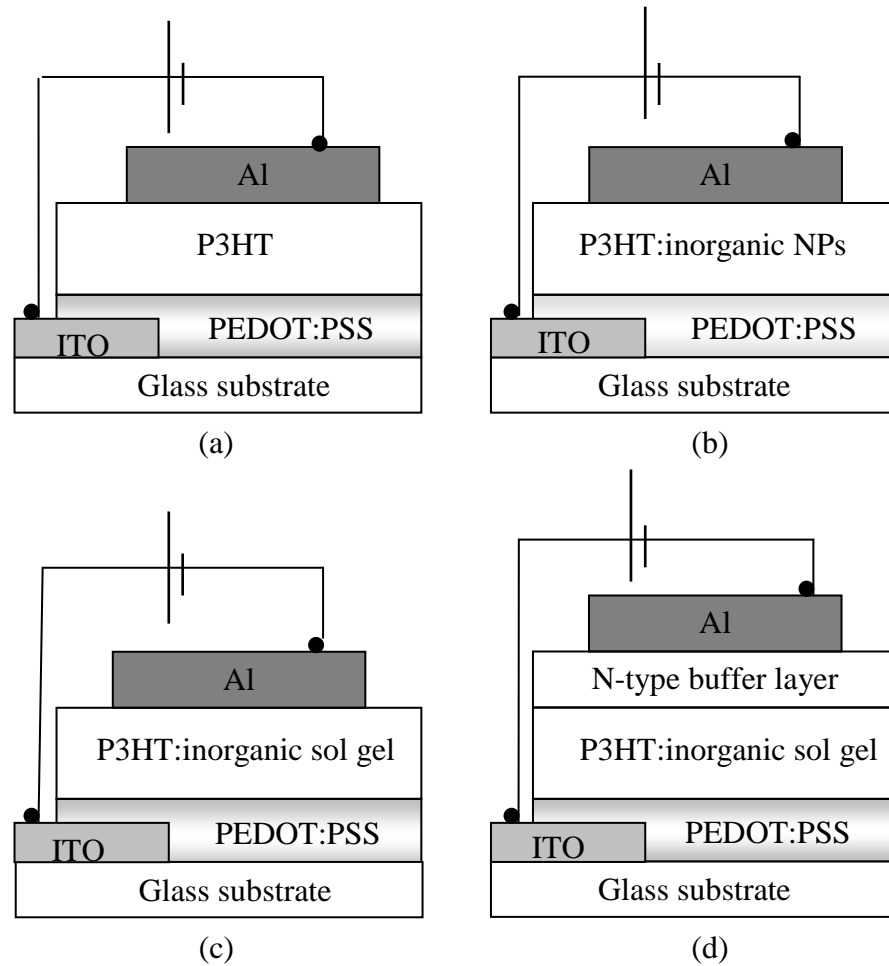


Figure 3.07: The device construction of solar cells based on different device geometries and hybrid systems.

3.4.2 Aluminum (Al) Electrodes Deposition via Thermal Evaporation

Thermal evaporation is one of the most commonly utilized metal electrode deposition techniques. The photograph of an Edwards 306 thermal vacuum evaporator used in this work is shown in Figure 3.08. This technique requires the process of evaporating a metal by heating it to sufficiently high temperature and then condensing it onto a cooler target to obtain a film with the desired metal electrode pattern. Figure 3.09 shows the schematic diagram of the evaporation system within a vacuum chamber. Before evaporation taking place, few metal deposits (aluminum) are clamped onto a

filament that typically made of tungsten due to its high melting temperature and low cost. The tungsten filament is well-connected to a high current source. The films are then placed in a designed shadow mask (see the inset of Figure 3.08) which is mounted on top of a substrate table, in order to obtain a desired metal electrode pattern on the films.

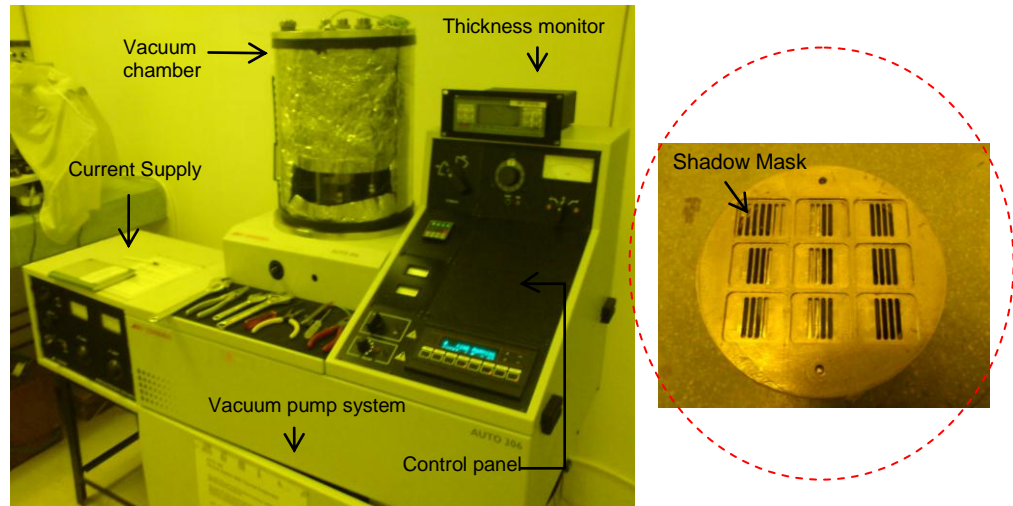


Figure 3.08: Thermal evaporation system for Al electrode deposition. The inset shows the designed shadow mask used in this work.

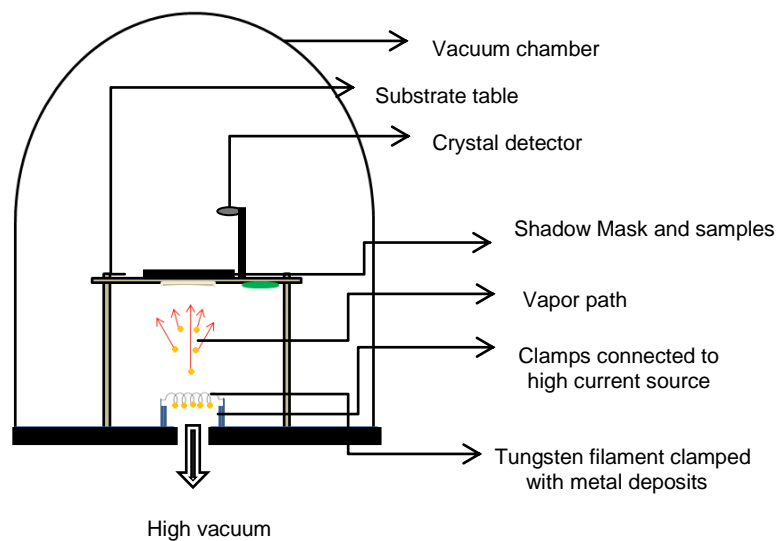


Figure 3.09: The schematic diagram of the evaporation system arrangement within the vacuum chamber.

After film loading and metal deposition, the evaporator system is required to be fine-pumped to provide a good vacuum condition inside the chamber. By applying a sufficient high current through the filament, the metal deposits may undergo sublimation and evaporate onto the target film. Typically, during an evaporation process, the metal vapour may easily undergo collisions with the surrounding gas molecules inside the chamber. Consequently, a fraction of the vapor is scattered within a certain distance during their movement through the gas. The mean free path for air molecule at room temperature is around 45 and 4500 cm at pressures of $\approx 10^{-4}$ and 10^{-6} mbar, respectively. Hence, pressures lower than 10^{-5} mbar are necessary to ensure a straight path for most of the evaporated metal to reach the target films in the vacuum chamber (metal-to-film distance of approximately 10 to 50 cm). A good vacuum condition is therefore a prerequisite for producing contamination free metal deposits (Chopra & Kaur, 1983; Stuart, 1983).

Besides, the evaporator system is fitted with a crystal detector which is connected to the Edwards thickness monitor to control the amount of metal deposits. Since there is always a lateral distance between the crystal detector and the target films, it is necessary to determine the tooling factor of the metal deposits which is referred to the ratio of respective amounts of evaporated metal deposits between the two different surfaces. It is a unique quantity for a particular evaporator that strongly depends on the dimension of the system and the types of metal deposits. Table 3.3 lists the experimentally determined parameters for the Al deposition used in this work. The deposition rate of the Al electrodes depends on the applied current in which a larger current produces a thicker layer of Al due to a faster evaporation rate.

Table 3.3: The deposition parameters of Al electrodes.

Metal	Tooling Factor	Pressure (10^{-5} mbar)	Current (A)	Evaporation Rate (A/s)	Thickness (nm)
Al	1.71	2.0-2.5	22-24	0.1-0.3	100-150

3.5 Characterization Techniques

In this section, several experimental techniques and instruments have been employed to characterize and investigate the properties of the thin films and devices, as discussed in the following sub-sections.

3.5.1 Ultraviolet-Visible-Near Infrared (UV-VIS-NIR) Spectrophotometer

In general, ultraviolet-visible spectroscopy involves the absorption ability of photons by the molecules in the UV-visible wavelength region of the electromagnetic spectrum which results in a transition of electrons from the HOMO to the LUMO level. In this process, the molecules may undergo several possible electronic transitions involving π , σ or n electrons, namely $\sigma \rightarrow \sigma^*$ transitions, $n \rightarrow \sigma^*$ transitions, $n \rightarrow \pi^*$, and $\pi \rightarrow \pi^*$ transitions (see Figure 3.10). For organic materials, the absorption spectroscopy is mainly based on the transition of n or π electron from bonding state to π^* excited antibonding state ($n \rightarrow \pi^*$, and $\pi \rightarrow \pi^*$ transitions), whereby the absorption peaks for these types of transitions typically fall in a range between 200 to 700 nm (Course, 2011). Additionally, these transitions require an unsaturated compound in the molecules to provide π electrons which is different from $n \rightarrow \sigma^*$ transitions that is undergone by saturated compounds containing atoms with non-bonding free electrons. Both $n \rightarrow \sigma^*$ and $\sigma \rightarrow \sigma^*$ transitions requires an absorption of photon with a shorter wavelength less than 200 nm. Thereby, merely $n \rightarrow \pi^*$ and $\pi \rightarrow \pi^*$ transitions that take place at a longer wavelength in the UV-vis region are noticeable.

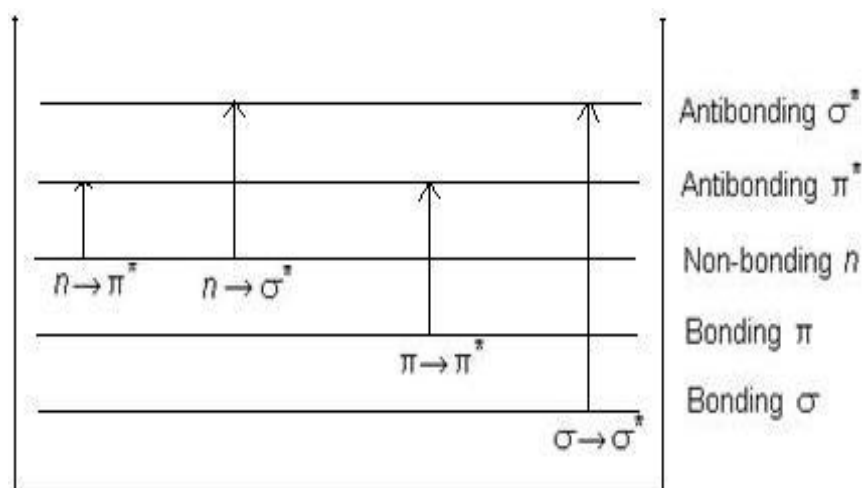


Figure 3.10: Possible electronic transitions of π , σ or n electrons.

The optical absorption spectra of the spin coated thin films are obtained by using the UV-VIS-NIR Spectrophotometer, model Jasco 570 UV-VIS/NIR. The photograph of this instrument is shown in Figure 3.11. Based on the absorption spectrum data, a variety of optical functions can be determined including absorption coefficient, types of optical transition, optical band gap, and so on. Typically, a spectrophotometer measures direct transmittance in percentage (%T), which is representing the percentage of incident light beam transmitted by a sample. This value can be converted into absorbance (A), whereby $A = \log (1/T) = \log (I_0/I)$ (Beer, 1852) according to Beer's law, where I_0 and I are the light intensities before and after passage through the sample, respectively.

A schematic diagram of the components of a UV-Vis-NIR spectrophotometer is shown in Figure 3.12. Basically, there are 3 main components of a UV-Vis-NIR spectrophotometer, namely a light source (visible and/or UV light source), a monochromator which is used to select the light beam with a desired wavelength and a detector to examine the light intensity. For Jasco V-570 UV-VIS-NIR spectrophotometer used in this work, two different types of light sources are employed, namely a deuterium discharge which is used in the ultraviolet region and a tungsten iodine lamp that is used in the visible and near-infrared regions. First, the light beam

from the source passes through a monochromator. The monochromatic light beam (with a single wavelength) is then split into two beams with equal intensities by a beam splitter system. One beam, referred as the sample beam passes through the sample holder, whereas another beam, referred as the reference beam passes through a reference holder containing only the base substrate. The intensities of these light beams are then examined using photodiodes detectors. Before the light beams reach the detector, the variation in the amount of light that passes through the sample and reference cells has to be amplified using differential amplifier. When the sample molecules are incident by light beam with an energy that matches a possible electronic transition, the molecules may favorably absorb part of the photon energy, $h\nu$. This results in an excitation of the molecules from ground state, E_0 to a higher energy state, E_1 , in which $h\nu = E_1 - E_0$. The wavelengths at which absorption occurs, together with the absorption intensity at each wavelength are processed and recorded by the computer software. Lastly, the optical spectrum is displayed through the computer screen. Table 3.4 shows the set parameters of the UV-VIS-NIR measurement. Lastly, the optical spectrum is displayed through the computer screen. Table 3.4 shows the set parameters of the UV-VIS-NIR measurement.



Figure 3.11: Photograph of Jasco V-570 UV-VIS-NIR Spectrophotometer.

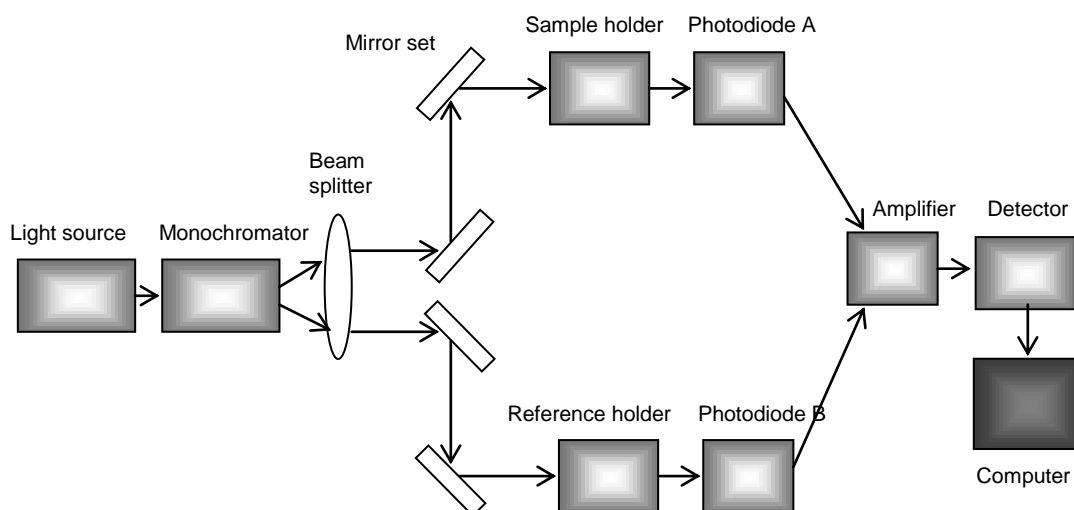


Figure 3.12: Schematic diagram of the components of a UV-VIS-NIR spectrophotometer.

Table 3.4: Parameters of UV-VIS-NIR spectrum.

Photometric mode	A
Response	Fast
Band width	5.0 nm
Scanning speed	2000 nm/min
Start wavelength	1000 nm
End wavelength	190 nm
Data pitch	2.0 nm

3.5.2 X-ray Diffraction (XRD) Technique

X-ray diffraction (XRD) is a non-destructive, rapid analytical technique primary used for phase identification and quantitative determination of a crystalline sample. The fundamental principle of X-ray diffraction is based on the occurrence of constructive interference of monochromatic X-ray beams upon the crystal planes in a crystalline sample. The X-rays, which are generated by a cathode ray tube, tend to collimate and are directed towards the sample. The interaction of the X-rays with the sample results in constructive interference when the condition satisfies Bragg's Law, namely $n\lambda = 2d\sin\theta$, where n is an integer represents the order of diffraction, λ is the radiation wavelength, d

and θ are the interatomic spacing distance and diffraction angle, respectively (see Figure 3.13). In other words, it means diffraction will only occur when the distance taken by the rays reflected from successive crystallographic planes differs by a whole number n of wavelength (Callister, 2007).

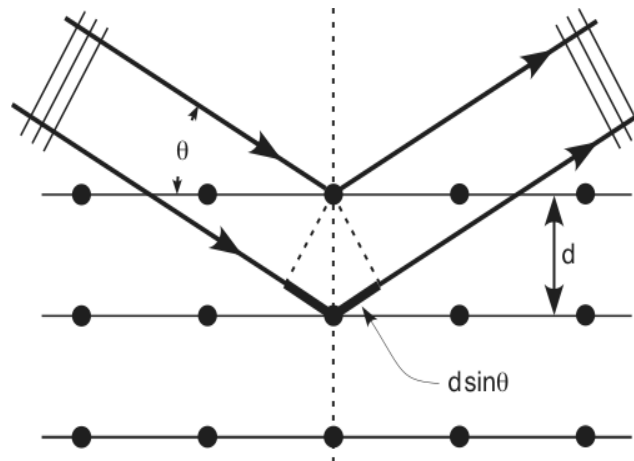
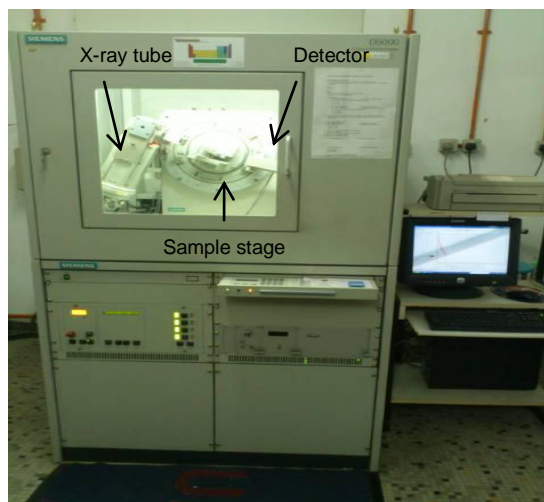


Figure 3.13: The diffraction pattern of X-rays by planes of atoms.

Figure 3.14 (a) and (b) shows the photograph of the X-ray diffractometer (Bruker AXS model) used in this work and a schematic diagram of the basic components of a X-ray diffractometer, respectively. A typical X-ray diffractometer comprises of three main components: a monochromatic X-ray tube, a sample holder, and an X-ray detector. The X-ray tube is evacuated and consists of a copper block with a metallic target anode, and a tungsten filament cathode with a relatively high voltage between them. By heating the filament to produce electrons, the large potential difference between the filament cathode and target anode drives the electron to accelerate towards the anode and bombards upon it. When the electrons have sufficient energy to dislodge inner shell electrons of the target material, X-ray spectra can be readily produced. Peak positions in XRD spectra can be observed where the X-rays have been diffracted by the crystal lattice. A detector is used to record and process the

X-ray signals, then to convert them into count rate before the signals are output to a device such as a computer monitor.

Basically, these XRD spectra consist of several components and the most common one is found to be K_{α} which is caused by the electronic transition from the L shell to K shell in an atom. One of the common target anode used for X-ray tube is copper (Cu), producing Cu radiation with a wavelength of 1.54 \AA (Krishnaswamy, Orsat, & Thangavel, 2012). The radiation wavelength is ideally suitable for probing the structural arrangement of atoms in a crystalline material since it is comparable to the atomic distance in a crystal. The geometry of an X-ray diffractometer is such that the tested sample is rotated in the path of the collimated X-ray at an angle of θ while the detector is mounted on an arm to record the diffracted X-rays by rotating at an angle of 2θ . The incident angle is then increased over time whereas the diffracted angle remains at 2θ above the source path. The instrument works for maintaining the angle and rotating the sample is known as a goniometer. Table 3.5 shows the scanning parameters of XRD measurement.



(a)

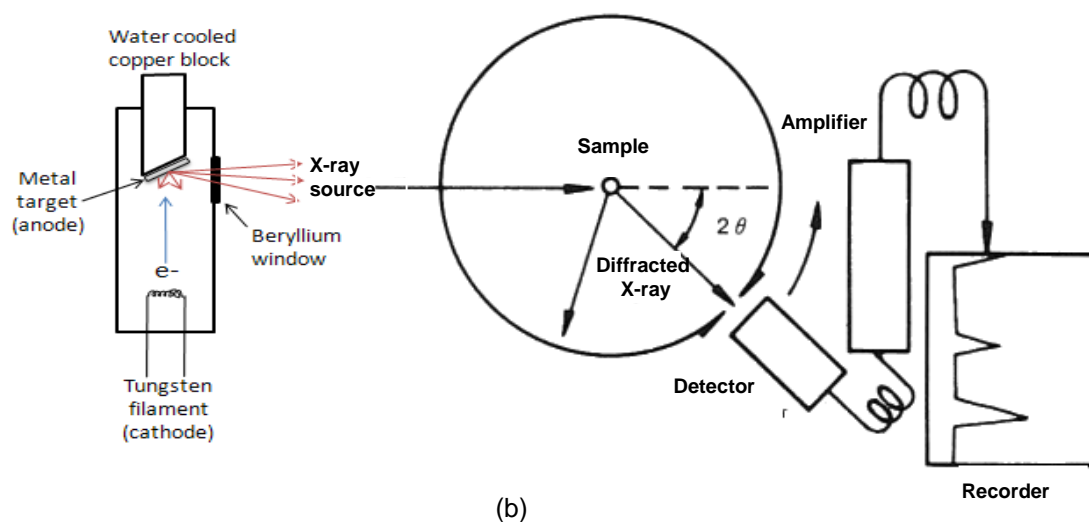


Figure 3.14: (a) Photograph of the XRD instrument (Bruker AXS). (b) The basic components of an X-ray diffractometer.

Table 3.5: Scanning parameters of XRD measurement.

Step size	0.04°
Step time	2 seconds
Applied voltage	40 kV
Scan range	2° - 60°

X-ray powder diffraction is most widely utilized for the identification of unknown materials with crystalline structure (e.g. inorganic compounds and minerals). The analyzed sample is required to be finely-grounded, homogenized, and the average bulk composition is determined. Regarding the known materials, there is a standard database corresponds to their structural characteristics including their crystalline structure, diffraction peak position and their relative intensity, miller-index, d-spacing and so on. The database is provided by an organization so-called “Joint Committee on Powder Diffraction Standards (JCPDS)”. By comparing the diffraction patterns and data, the identity of an unknown material is therefore can be determined (Langford & Louër, 1996). On the other hand, thin film diffraction is commonly utilized for the characterization of the crystallographic structure, composition, dislocation density, internal strain, and preferential orientation of substrate-based thin films. The nature of

thin film is strongly dependent on their crystal qualities, in which the processing parameters have to be well monitored and optimized.

3.5.3 Atomic Force Microscopy (AFM)

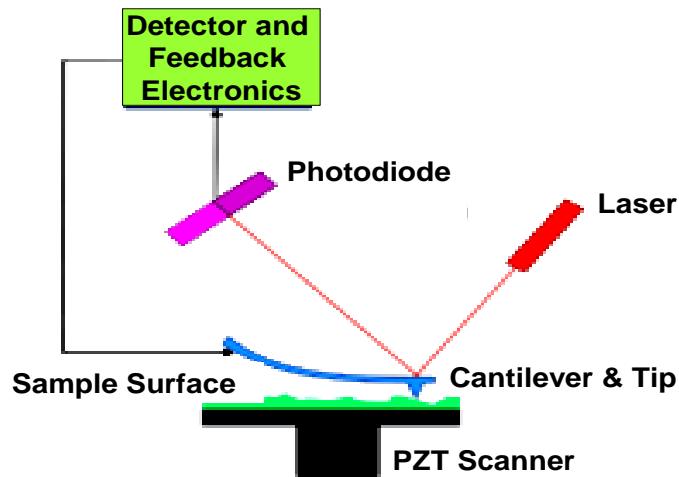


Figure 3.15: Schematic diagram of an atomic force microscope.

To study the morphological properties of the spin coated thin films, atomic force microscope (AFM) is employed, which is one of the high resolution types of scanning probe microscope that able to produce an image resolution up to the order of nanometer range. That is much better than the optical diffraction limit. The schematic diagram of an atomic force microscope is illustrated in Figure 3.15. The fundamental working principle of an AFM is based on the deflection of the cantilever due to the response to interactive force between the cantilever tip and sample surface according to Hooke's law. Depend on the conditions, these forces measured by AFM may include Van der Waals forces, electrostatic forces, mechanical force, and so on. Typically, the deflection is measured using a laser light beam that reflected from the top surface of the cantilever into a photodiode. By measuring the deviation of signals that has been detected using detector and feedback electronics, any changes in the deflection of cantilever can be measured. The scanning movement of the tip in x, y and z directions is well performed

by extremely precise piezoelectric transducers. The computer system is used to control the xyz translations and records the detected laser beam signals (Geisse, 2009). Originally, the AFM can be worked in several types of operation modes, depending on the applications. Possible operation modes are divided into static modes (also known as contact modes) and dynamic modes (non-contact or tapping modes) which require the vibration of cantilever to allow high resolution topographic imaging of easily damageable or soft sample surface. In this research work, contact mode AFM is employed whereby the tip is brought in close contact to the sample surface during the scanning process. In this mode, the deflection of cantilever is detected and compared to a certain desired deflection value in a digital current (DC) feedback electronics. If the detected deflection deviates from the desired value, the feedback electronics may react by applying a voltage to the piezoelectric transducers to adjust the position of the sample relative to the cantilever in order to restore the desired deflection value. In other words, the AFM is always operated under a constant force between the tip and sample surface by maintaining a constant deflection of cantilever (Eaton & West, 2010). After the data is collected, it is then constructed by specific software based on the set parameters to turn into a topographic picture of the scanned sample. The photograph of the AFM (Veeco Dimension 3000) used in this present work is shown in Figure 3.16 and the related measurement parameters of AFM are indicated in Table 3.6.

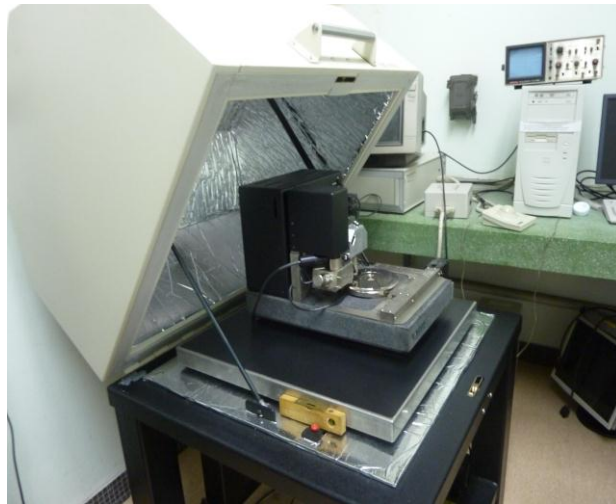


Figure 3.16: Photograph of Veeco Dimension 3000 AFM instrument.

Table 3.6: Parameters of the AFM measurement.

System name	Veeco D3000 AFM
Scan size	10.00 μm
Scan rate	2.00 Hz
Image data	Height
Data scale	10.00 nm, 250.00 nm & 500.00 nm

3.5.4 Field-Emission Scanning Electron Microscopy (FESEM)

In order to further visualize the surface morphology of the films, field-emission scanning electron microscope (FESEM) images are obtained using a Leo Supra 50VP microscope equipped with an Oxford INCA 400 energy dispersive microanalysis system, as shown in Figure 3.17. In general, scanning electron microscope (SEM) is a sort of electron microscope that capable of producing image of a sample by using energetic electron beam to scan across the sample on a fine scale. The interaction between the electrons and the atoms that make up the sample results in a signal generation that contains information about the physical properties of the sample such as the sample's surface topography, composition, distribution pattern, shape and size dimension of the grains as well as its crystallographic feature (Amelinckx, 1997).

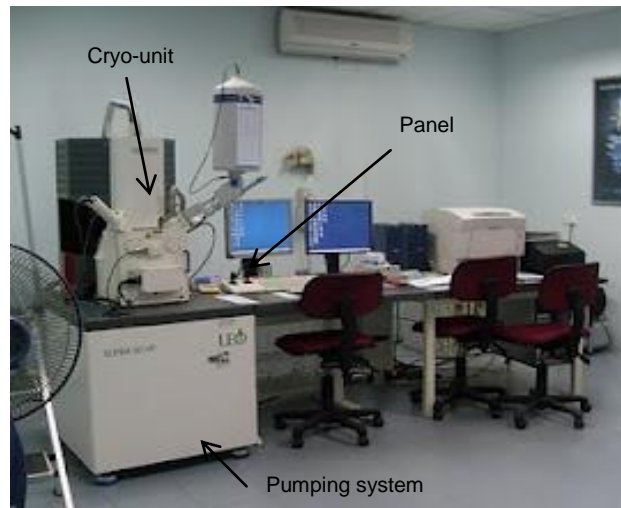


Figure 3.17: Field-emission scanning electron microscope (FESEM).

The working principle of a typical SEM is schematically shown in Figure 3.18. It consists of an electron gun that fitted with a filament cathode. In conventional SEM, a tungsten filament cathode is used due to its highest melting point and low vapor pressure compared to other metals. Upon heating, an electron beam is thermionically emitted from the electron gun. The beam which typically possesses an energy ranging from 0.2-40.0 keV is focused to a spot about 0.4–5.0 nm in size by few set of condenser lenses. As the beam passes through pairs of deflection coils in the electron column (typically in the final lens), it is then deflected into the x and y axes. Accordingly, a scanning in a raster pattern over a rectangular area of the sample surface can be performed. Upon the interaction of the primary electron beam with the sample, the electrons lose energy by continuous random scattering and absorption within the sample. The energy exchange between the beam and the sample produces reflections of highly energetic electrons by elastic scattering and emissions of secondary electrons by inelastic scattering that can be well detected by specialized detectors (Bogner, Jouneau, Thollet, Basset, & Gauthier, 2007). The beam current absorbed by the sample can be detected and it is used to produce images of the distribution of sample current. The

generated signals is then can be altered and amplified by electronic amplifiers, which are displayed as variations in brightness mode on a computer screen.

Regarding FESEM, it comprises of a field-emission cathode in the electron gun which provides narrower probing beam at low and/or high electron energy. It offers several peculiar advantages over the conventional SEM (PhotoMetrics, date unknown). First, it is capable of producing less electrostatically distorted, clearer images with improved spatial resolution down to 1.0-0.5 nm, which is 3-6 times much better than the conventional SEM. Secondly, contamination spots in smaller size dimension can be examined at electron accelerating voltages that makes FESEM to be compatible with energy dispersive X-ray spectroscopy (EDX). Thirdly, it enables to produce high quality, low voltage images with minimized electrical charging effects. Additionally, the probability of the sample damage is lower than that of the conventional SEM due to the reduced penetration of electrons with low kinetic energy (accelerating voltage ranges from 0.5-30.0 kV) closer to the sample surface.

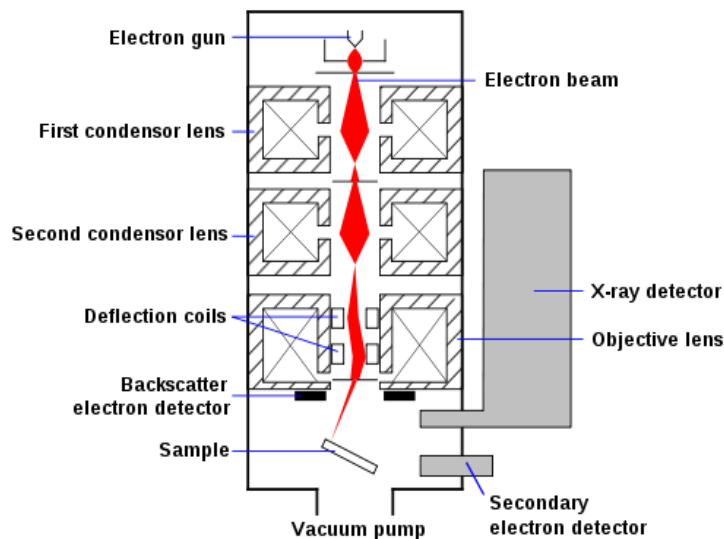


Figure 3.18: Principle features of a SEM instrument.

3.5.5 Surface Profilometer

Surface profilometer is one of the common measurement tools that is used to probe the surface profile and topography of a sample. Typically, similar to other scanning probe microscopes (Kalinin et al., 2007), a profilometer utilizes the same imaging fundamentals, but with a mass cantilever system to maintain the tip force while scanning. It has a larger probe tip in a radius dimension range of 20 nm up to 25 μm , which is usually made of diamond to reduce tip wear. The larger tip may limit the vertical and horizontal resolutions. A profilometer can perform several functions including surface roughness or film thickness measurement. Nowadays, modern types of profilometer may even capable of producing 3-dimensional topographic maps rather than common, traditional line scans (single horizontal direction scan during feature height) (David, 2004).

Basically, there are two types of surface profilometers, namely contact and non-contact profilometers. Contact profilometer, also known as probe tip-based profilometers, performs the surface measurement by dragging the sharp tip vertically in contact with the sample surface and then moving laterally across the sample surface at a specified contact force. For the film thickness measurement, scratching traces have to be formed on the film surface in order to generate height difference between the substrate and the film. Generally, it can measure small surface variations in vertical tip displacements as a function of position ranging in height from 10 nm up to 1 mm. The height variation of the tip generates an analog signal which is then converted into a digital signal to be analyzed and displayed in form of surface profile, as shown in Figure 3.19(b). This is where, the horizontal resolution is monitored by means of the scan speed and data signal sampling rate. On the other hand, a non-contact method is specially used for optical profilometers. It is used to measure the surface texture by optically scanning the sample surface using a light or laser beam (Stout & Blunt, 2000).

The working mechanism is schematically shown in Figure 3.19 (a). It can provide as many as information like a tip-based profilometer.

In this work, a contact surface profilometer instrument with a model of KLA Tensor P-6 is used to measure the thickness of spin-coated thin films (see Figure 3.20). To obtain a more precise film thickness measurement, several scratching traces are made upon the film surfaces and the average thickness of all these traces is then measured. The parameters used for the film thickness measurement are tabulated in Table 3.7.

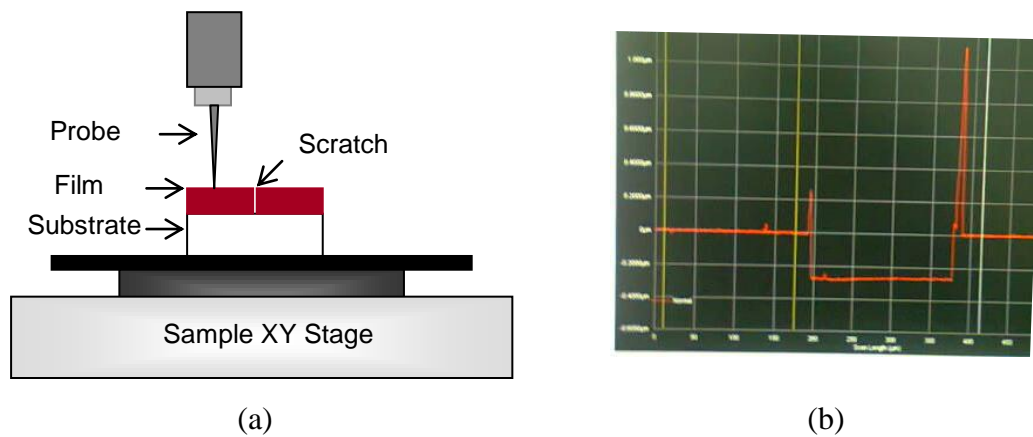
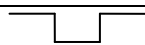


Figure 3.19: (a) The schematic diagram of a contact profilometer. (b) Resultant surface profile that is generated based on the tip deflection.



Figure 3.20: KLA Tensor P-6 surface profilometer for film thickness measurement.

Table 3.7: Scanning parameters of film thickness measurement.

Scan type	2D
Scan length	1000 μm
Scan speed	100 μmsec^{-1}
Sampling rate	20 Hz
Applied force	1.00 mg
Pattern scanning	

3.5.6 Photovoltaic (PV) Measurement

The photovoltaic performance of the fabricated hybrid solar cell devices is measured using Keithley 236 Source Measurement Units (SMUs) under AM1.5 G–filtered white light irradiation with a power intensity of 100 mWcm^{-2} from Oriel 67005 solar simulator. The solar simulator is a device which is able to provide illumination of approximately identical to the natural light. It is applicable in performing indoor test measurements under laboratory condition, such that it can be used for testing solar cells, plastics, sunscreen and other materials or devices. There are several types of solar simulators, varying in spectral power distribution and irradiance geometry. The type of lamp source used in solar simulators may significantly determine the spectral power distribution, whereas the beam optics determines the irradiance geometry and efficiency. The Oriel 67005 solar simulator (see Figure 3.21(a)) used in this work capable of providing a spectrum well-matched to the solar spectra under ambient condition by using high pressure Xenon arc lamp source. The internal structure of the Oriel solar simulator is shown in Figure 3.21(b). The Xenon arc lamp is able to emit an approximately 5800K blackbody-like spectrum with occasional line structure. In order to realize the Air Mass (AM) 1.5 global reference spectrum at ambient condition for PV measurement, an AM1.5 filter is used to modify and refine the spectral distribution of the Xenon arc lamp source. The small high radiance arc enables efficient beam collimation which thereby yields a continuous output with a solar-like spectrum in homogenous collimated beams (Yass & Curtis, 1974).

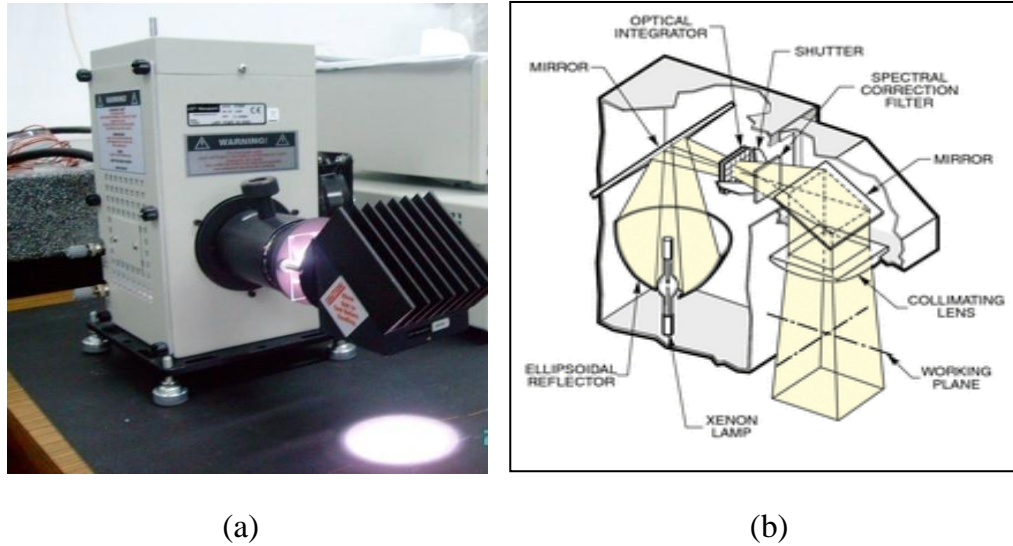
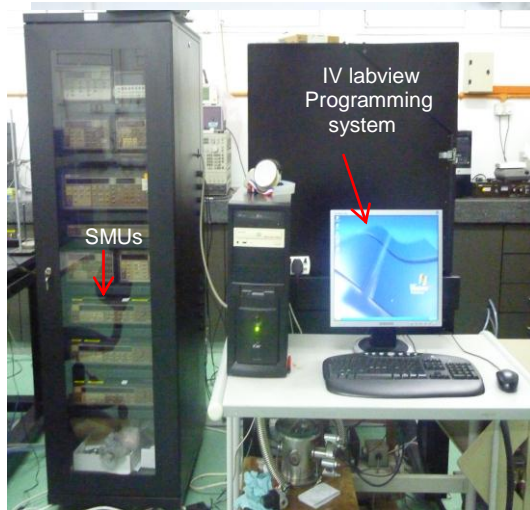


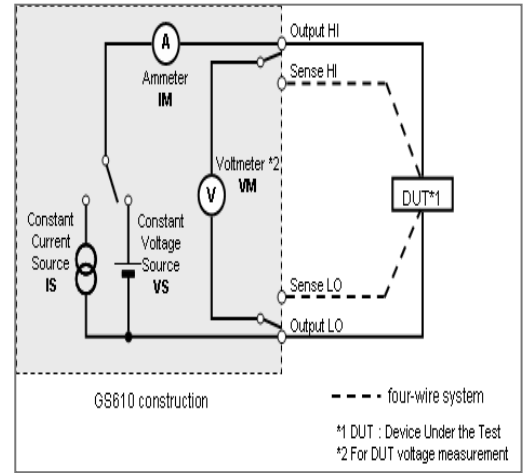
Figure 3.21: (a) An Oriel 67005 solar simulator. (b) The internal structure of the Oriel solar simulator.

The Keithley 236 SMUs are well programmable instruments which are capable of sourcing and measuring both current and voltage simultaneously. These systems comprised of 4 instruments in one; namely voltage source, voltage meter, current source and current meter. They typically source voltage from $100\ \mu\text{V}$ to $110\ \text{V}$ and current from $100\ \text{fA}$ and $100\ \text{mA}$ (Keithley, 1990). Besides, they offer four quadrant source capabilities to handle a wide range of tests under bipolar voltages and to sink power. Additionally, SMUs able to perform sweeps of both current and voltage. Figure 3.22(a) and (b) show the photograph of the SMU instruments and a device connection circuit to its appropriate terminals under I-V measurement, respectively. As indicated in Figure 3.22(b), one side of the device is connected to the Output HI and Sense HI terminals of SMU1; the other side is connected to the Output LO and Sense LO terminals of the ground unit. A voltage is allowed to be sourced across the device through the four-wire connection system by using the test leads between Output HI and Output LO. Whereas, the variation in voltage across the device is measured via the test leads across Sense HI and Sense LO in which both the sense leads are responsible to make sure the voltage across the device is the output yield (*Electronic design*, 1989). Lastly, a measured I-V

plot is obtained. In order to determine the current density (J) through the device, the obtained current value has to be divided by the active area of the device. Accordingly, a J-V characteristic curve is derived and the major photovoltaic parameters can be extracted from it, as has been discussed in section 2.10.2 of Chapter two.



(a)



(b)

Figure 3.22: (a) A Keithley 236 SMU instrument. (b) A solar cell device connected to its appropriate terminals under I-V measurement.

CHAPTER 4

CHARACTERIZATION OF P3HT:ZNO HYBRID THIN FILMS AND SOLAR CELL DEVICES

4.1 Overview

This chapter discusses about the effects of blend composition on the optical, structural, morphological as well as the electrical properties of the P3HT:ZnO hybrid systems-based thin films and solar cell devices.

4.2 Optical Characterization: Ultraviolet-Visible-Near Infrared (UV-Vis-NIR) Spectra Analysis

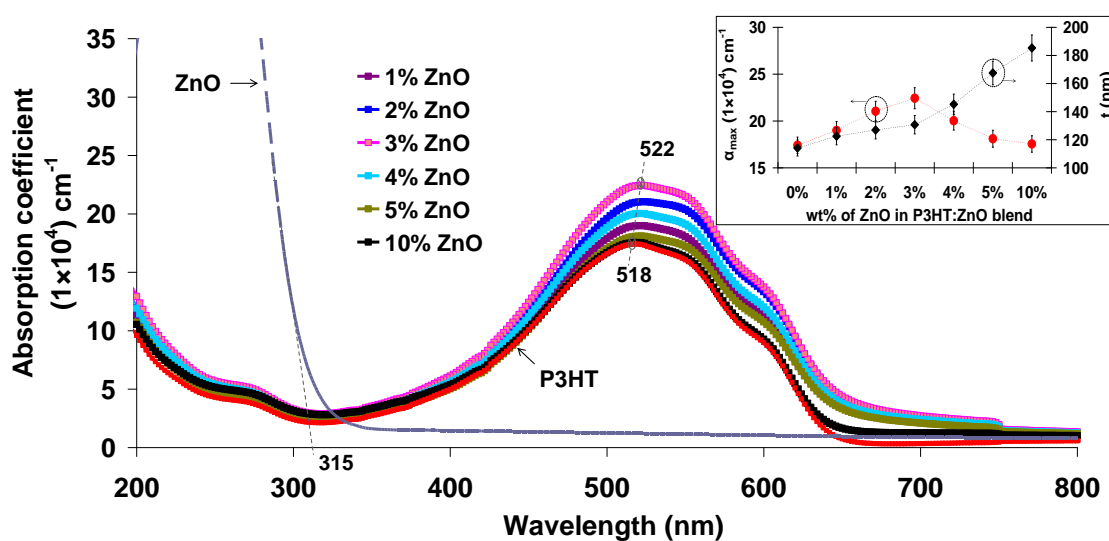


Figure 4.01: Absorption coefficient of pristine P3HT, ZnO and P3HT:ZnO blend films with different contents of ZnO nanoparticles. The inset shows the variation of maximum absorption coefficient peak values, α_{max} and film thickness, t as a function of blend composition.

To determine the optical properties of the pristine P3HT, ZnO and P3HT:ZnO blend films, ultraviolet-visible-near infrared (UV-Vis-NIR) absorption spectra measurements have been carried out. Figure 4.01 shows the absorption coefficient spectra of the pristine P3HT, ZnO and P3HT:ZnO blend films with different concentration of ZnO. The absorption coefficient values of the peaks together with the

corresponding peak positions at the particular wavelengths are tabulated in Table 4.1. It can be observed that the pristine P3HT film exhibits a strong absorption in the visible wavelength range from 450-650 nm with an absorption peak at 518 nm. This absorption band is the characteristic which is ascribed to the π - π^* transition of the P3HT conjugated backbone system. The development of a vibronic feature of P3HT can be observed as well from the shoulder peak around 600 nm, implying a good ordering of intra-chain interactions within the polymer chains (Jiang et al., 2002). It is noted that ZnO film is preferable to absorb light in the UV wavelength range from 200-400 nm with an absorption onset around 315 nm.

Upon the incorporation of a small amount of ZnO nanoparticles into P3HT (light ZnO doping), the results show that the absorbance in UV-Visible range has been increased. This can be proven by comparing the absorption coefficient peak values of the P3HT:ZnO blends with the variation of ZnO contents, as displayed in the inset of Figure 4.01. This suggests that the presence of ZnO in P3HT polymeric film may aid in photon harvesting mechanism, thereby gradually enhances the absorption intensity. The peak value reaches the highest point for blend film consists of 3% of ZnO nanoparticles. However, as the ZnO nanoparticles content is increased up to 4% in composition, the absorption intensity drops, especially at the wavelength longer than 400 nm. This can be clearly observed from the decreased absorption coefficient peak values for the P3HT:ZnO blend films consist of more than 3% of ZnO nanoparticles. This implies that the ordered intermolecular packing structure of the P3HT polymer chains is preserved in the blends over this range of composition.

However, upon addition of ZnO nanoparticles of more than 3% in blends (heavier ZnO doping), the intermolecular packing in P3HT chains has been disrupted by the excess inorganic nanoparticles loadings. This disordering of the P3HT polymer chains may reduce the interchain interaction within the polymer and result in a slight

bleaching of π - π^* absorption in the blend film. This fact can be supported by data tabulated in Table 4.1 in which the wavelength positions of the peaks are slightly red-shifted from 518 nm to 524 nm for blend films consist of less than 3% of ZnO nanoparticles, but later it begins to cause a blue-shift gradually from 524 nm to 520 nm beyond this composition range. The occurrence of blue-shift here implies a disrupted interchain interaction within the polymer chains (Brown, Sirringhaus, Harrison, Shkunov, & Friend, 2001; Y. Kim et al., 2005). Furthermore, the existence of these loadings may favorably cause a reduction in the volume occupied by benzene ring of the P3HT polymer within the blend film, and thus diminish the contribution of P3HT itself to the light absorption in the visible wavelength spectral region (Y. Kim, et al., 2005).

Table 4.1: The comparison of the absorption coefficient peak values and the corresponding wavelength positions for pristine P3HT and P3HT:ZnO blends.

Samples	Maximum absorption coefficient, α_{\max} (1×10^4) cm^{-1}	Position of absorption peak, λ (nm)
Pristine P3HT	17.4	518
P3HT + 1% ZnO	19.0	522
P3HT + 2% ZnO	21.0	524
P3HT + 3% ZnO	22.4	522
P3HT + 4% ZnO	20.0	522
P3HT + 5% ZnO	18.1	522
P3HT + 10% ZnO	17.5	520

Table 4.2: The values of average thickness for pristine P3HT, ZnO and P3HT:ZnO blend films.

Samples	Film thickness			
	Spot 1	Spot 2	Spot 3	Average thickness (nm)
Pristine P3HT	111.0	120.8	110.6	114.1 ± 0.1
Pristine ZnO	160.9	178.9	153.4	164.4 ± 0.2
P3HT + 1% ZnO	123.2	118.7	125.5	122.5 ± 0.5
P3HT + 2% ZnO	126.2	115.8	138.6	126.9 ± 0.2
P3HT + 3% ZnO	125.6	127.5	139.0	130.7 ± 0.1
P3HT + 4% ZnO	135.9	159.7	140.1	145.2 ± 0.1
P3HT + 5% ZnO	152.4	173.5	176.6	167.5 ± 0.5
P3HT + 10% ZnO	182.3	179.5	194.2	185.3 ± 0.1

Table 4.2 shows the average thickness of the photoactive film layer. It can be observed that the thicknesses of the P3HT:ZnO blend films increase from 122.5 nm to 185.3 nm with the increasing content from 1 to 10% of ZnO nanoparticles. Basically, the film thickness has a major effect on the device performance as well. If the photoactive layer is too thin, then the photovoltaic device may produce a low efficiency (Moule, Bonekamp, & Meerholz, 2006). In this study, the results (see Figure 4.2) show that the absorption coefficient peak values of the blend films decrease gradually from $22.4 \times 10^4 \text{ cm}^{-1}$ to $17.5 \times 10^4 \text{ cm}^{-1}$ with the film thickness, especially for the blend composition above 3% of ZnO nanoparticles. It has been reported by Moule et al., (2007) about the effects of film thickness to the device performance in which too thin film may unfavorable for high photon absorption. In fact, the number of photogenerated exciton increases with the film thickness, owing to a greater absorption of light. However, the recombination rate of charge carriers may increase with increasing film thickness as well, due to a longer distance taken by the charge carrier to diffuse to reach their respective electrodes. Furthermore, if the film is too thick, then it may induce high optical interference effects within the solar cell comprised of reflective cathode surface, owing to its comparable thickness to the wavelength of light (Moulé & Meerholz, 2007). Moule et al. reported that a minimum efficiency was obtained for P3HT:PCBM solar cells when the film thickness was around 150 nm, owing to the interference effects (Moule, et al., 2006). Thereby, an optimal film thickness is also one of the prerequisites for a good solar cell performance and need to be taken account as well. Here, in my research work, it is found that the optimal film thickness is around 120-140 nm, as indicated by the high values in absorption coefficient spectra (see the inset of Figure 4.01).

In most of the semiconducting materials, their optical properties such as the optical energy gap, E_g can be well analyzed at the fundamental absorption edge in terms

of band-to-band transition concept according to Fujii et al's report (Fujii, Nishikiori, & Tamura, 1995; Gagandeep, Singh, Lark, & Sahota, 2000). One of the considerable key parameters in estimating the E_g of the photoactive thin film is the absorption coefficient, α which defines the amount of light absorbed by a material when the light incident upon it. It can be obtained from the absorbance raw data and film thickness value by applying the Beer Lambert Law equation (Al-Faleh & Zihlif, 2011):

$$I = I_o \exp(-\alpha t) \quad (4.1)$$

Since the transmission of light is well related to the absorbance, A , where $A = \log\left(\frac{I_o}{I}\right)$,

equation (4.1) consequently turns into the following equation:

$$\alpha = \frac{2.303}{t} \log\left(\frac{I_o}{I}\right) = \frac{2.303A}{t} \quad (4.2)$$

where I_o and I are the intensities of incident and transmitted light, respectively and t is the thickness of absorber. By assuming the absorption edge tends to possess a parabolic variation with the photon energy, hence the E_g of a material can be calculated by the Tauc's relationship (Muhammad & Sulaiman, 2011; Souri, 2011):

$$\alpha h\nu = \alpha_o (h\nu - E_g)^n \quad (4.3)$$

in which α_o is an energy-independent constant and E_g is the optical band gap and n is a value to determine the type of the involved optical transition, in which $n = \frac{1}{2}$ or 0.5 for direct allowed optical transition while $n = 2$ for indirect allowed transition. By applying the natural logarithm and the derivation of equation (4.3), a new equation can be expressed as below:

$$\frac{d\ln(\alpha h\nu)}{dh\nu} = \frac{n}{h\nu - E_g} \quad (4.4)$$

By referring to equation (4.4), the plots of $d\ln(\alpha h\nu)/dh\nu$ versus $h\nu$ for both pristine P3HT and ZnO nanoparticles films are shown in Figure 4.03. The peak of the plot at a particular energy value gives the approximate value of the optical band gap

where $h\nu = E_g$. It can be clearly observed that the peaks of the graphs (a) and (b) in Figure 4.3 occur at $h\nu = E_g$ of ~ 1.93 eV for P3HT and E_g of ~ 4.00 eV for ZnO nanoparticles films.

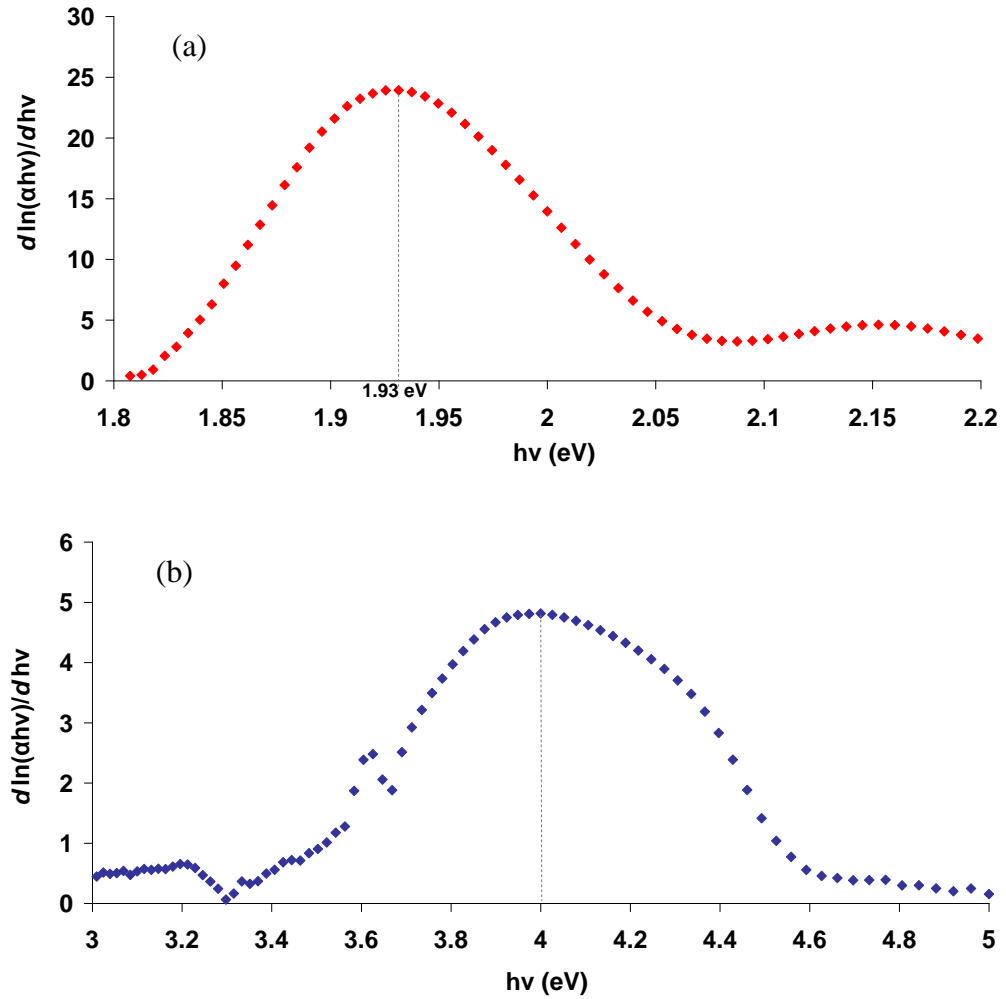
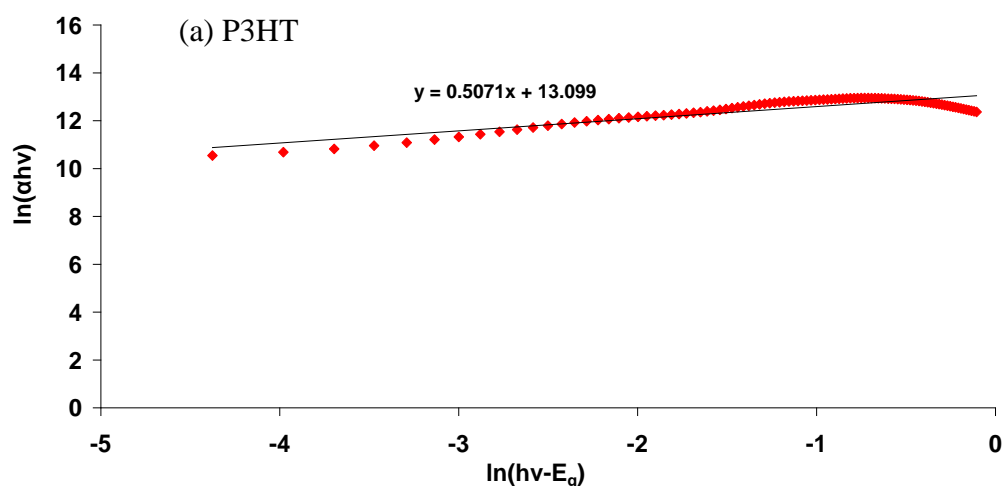


Figure 4.02: The pre-estimated E_g of the pristine (a) P3HT film and (b) ZnO nanoparticles film using plots of $d \ln(\alpha h\nu) / d h\nu$ versus $h\nu$.

Using the initial values of E_g , graphs of $\ln(\alpha h\nu)$ versus $\ln(h\nu - E_g)$ are plotted for the sake of determining the n value, as shown in Figure 4.03. The slope of the curves produce an estimated value of $n \approx 0.5$ for both the pristine P3HT and ZnO nanoparticles films, indicating that both materials undergo direct allowed optical transitions. This estimation successfully provides evidence for the existence of a direct band gap between the energy bands in P3HT which is in agreement with other findings of organic materials (T.-A. Chen, Wu, & Rieke, 1995; Coakley & McGehee, 2004; Merhari, 2007;

Smestad et al., 2003; Xiang, Wei, & Gong, 2009). On the other hand, several literature reports reveal that ZnO nanoparticles films are favourable to undergo direct allowed optical transitions as well (Norton et al., 2004; Olson et al., 2007; Xiang, et al., 2009). In order to evaluate the E_g more precisely, graphs of $(\alpha h\nu)^2$ against $h\nu$ are plotted as exhibited in Figure 4.04. By extrapolating the straight linear portion of the plot to $(\alpha h\nu) = 0$, E_g of ~1.97 eV and ~4.20 eV are obtained for P3HT and ZnO, respectively.

The E_g value obtained for pristine P3HT is considerably consistent with some of the reported data (Dicker, de Haas, Siebbeles, & Warman, 2004; Shrotriya, Ouyang, Tseng, Li, & Yang, 2005). However, the E_g (1.97 eV) of ZnO nanoparticles film is found to be higher than that of the reported values of bulk ZnO film ($E_g \approx 3.2$ -3.5 eV at room temperature) (Ravirajan et al., 2006; Srikant & Clarke, 1998). This may be ascribed to the variation of ZnO nanoparticles size that responsible for tuning the E_g compared to its bulk substitute (Yadav, Mishra, & Pandey, 2010; Zhuravlev, Pietryga, Sander, & Schaller, 2007). Besides, the processing conditions and environmental factors including the changes in ambient temperature may also contribute to this considerable difference in E_g value. The typical energy band diagram of P3HT and ZnO is illustrated in Figure. 4.05. The HOMO and LUMO level of P3HT are located at ~5.2 eV and ~3.2 eV, respectively, whereas the energy level of conduction band and valence band of ZnO are positioned at ~4.3 eV and ~8.5 eV, respectively.



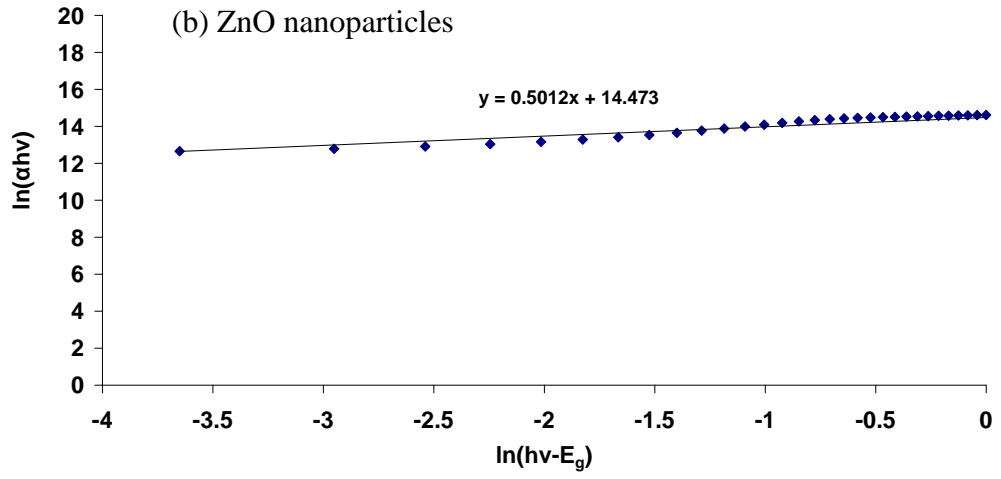


Figure 4.03: Plots of $\ln(\alpha h\nu)$ versus $\ln(h\nu - E_g)$ to determine the n value for (a) P3HT and (b) ZnO nanoparticles films, respectively.

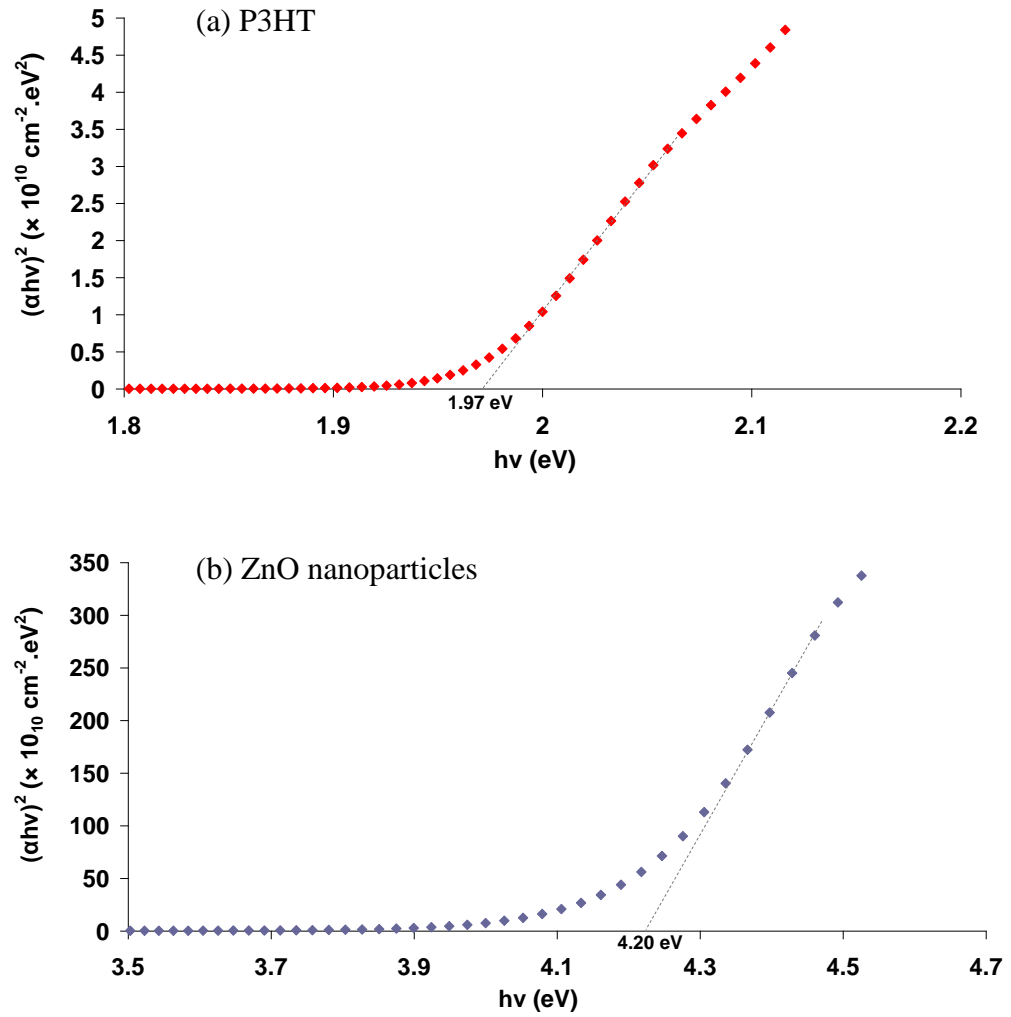
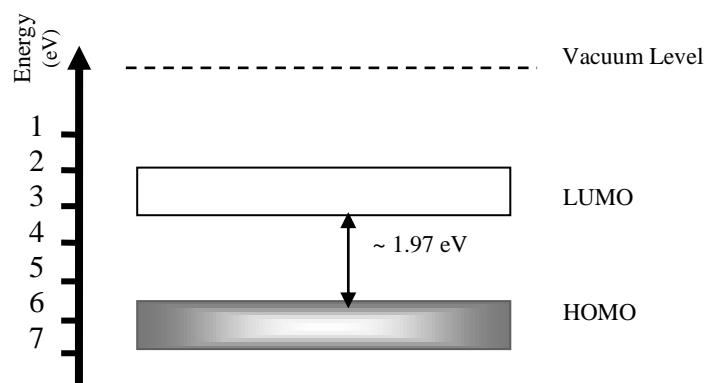
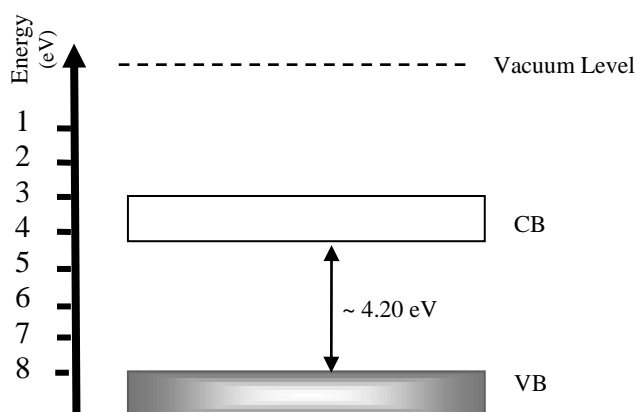


Figure 4.04: Plots of $(\alpha h\nu)^2$ against $h\nu$ for (a) P3HT and (b) ZnO films.



(a) P3HT



(b) ZnO nanoparticles

Figure 4.05: The typical energy band diagram of (a) P3HT and (b) ZnO nanoparticles films where the conduction band of ZnO is tunable due to the variation in nanoparticles size.

By utilizing the same method, the E_g for P3HT:ZnO blend films with different concentration of ZnO nanoparticles are able to be determined as well, as shown in Figure 4.06 and Figure 4.07. All the obtained values of the E_g for the pristine P3HT, ZnO and P3HT:ZnO blend films are tabulated in Table 4.3. The results show that the value of E_g (more precisely, based on the plots of $(\alpha h\nu)^2$ against $h\nu$) is reduced upon the incorporation of ZnO nanoparticles into P3HT which is found to be in accordance with several other research reports (Cook, Katoh, & Furube, 2009; Takahashi et al., 2012). The narrowing of the band gap indicates a broader absorption spectrum has been

achieved whereby more photons throughout the entire solar spectrum can be harvested. This can be further supported by the results of absorption coefficient spectra shown in Figure 4.01 and data tabulated in Table 4.1, which explains the occurrence of a red-shift in visible wavelength range for blend films at lower ZnO concentration. Upon the intervention of low concentration of dopants into P3HT, the chemical structure of the P3HT chain is transformed from benzoid into quinoid form, which favors a linear or expanded-coil conformation. The quinoid geometry of the P3HT yields an increase in the double bond character of the coplanar inter-ring bonds, and hence causes an increment in the extent of π -conjugation. Therefore, the red-shift of the absorption peak is reasonable. The longer the extent of conjugation, the lower the separation distance between the adjacent energy levels, which in turn means a smaller E_g is resulted. (Nalwa, 2001; Sandberg et al., 2002). However, the E_g value rises again from 1.94 eV until reaches the critical value of 1.97 eV which is comparable to the E_g of P3HT \sim 1.97 eV for films consist of $>3\%$ ZnO nanoparticles in blends, as indicated in Table 4.3. This suggests that the heavier ZnO loadings have no further significant effect on the optical band gap of the blend composite films.

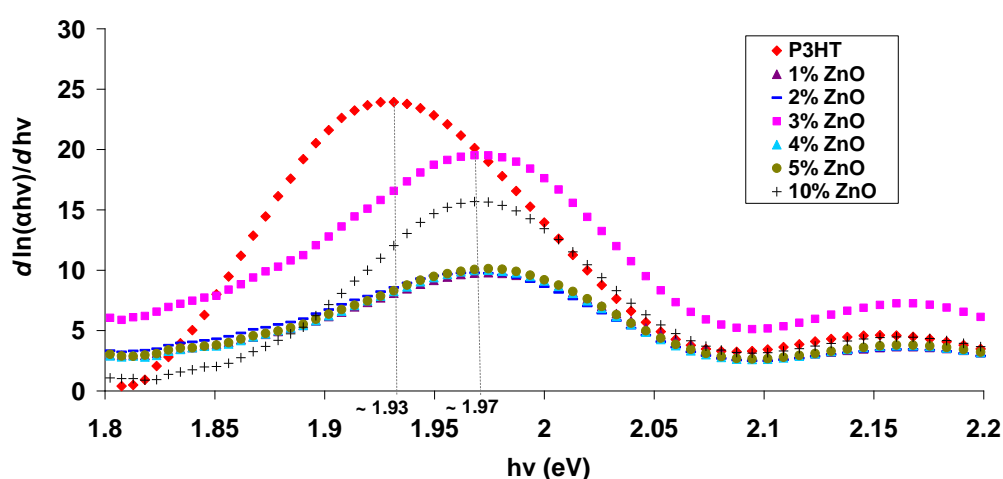


Figure 4.06: Plots of $d\ln(\alpha hv)/dhv$ versus $h\nu$ to pre-estimate the E_g of the P3HT:ZnO blend films with different contents of ZnO.

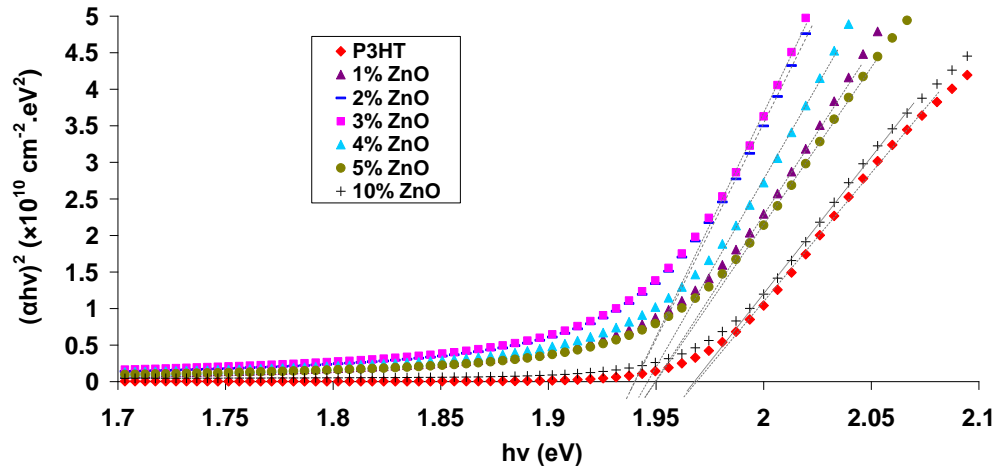


Figure 4.07: Plots of $(\alpha h\nu)^2$ against $h\nu$ for P3HT:ZnO blend films with different contents of ZnO.

Table 4.3: The values of E_g for pristine P3HT, ZnO and P3HT:ZnO blend films based on two different types of functions, in which the later one gives a more precise estimation value of E_g .

Samples	Functions	
	$\frac{d\ln(\alpha h\nu)}{dh\nu}$ $E_g (\pm 0.01 \text{ eV})$	$(\alpha h\nu)^2$ $E_g (\pm 0.01 \text{ eV})$
Pristine P3HT	1.93	1.97
Pristine ZnO	4.00	4.20
P3HT + 1% ZnO	1.97	1.95
P3HT + 2% ZnO	1.97	1.94
P3HT + 3% ZnO	1.97	1.94
P3HT + 4% ZnO	1.97	1.94
P3HT + 5% ZnO	1.97	1.95
P3HT + 10% ZnO	1.97	1.97

4.3 Structural Characterization: X-ray Diffraction (XRD) Spectra Analysis

To determine the structural properties of the pristine P3HT, ZnO and the P3HT:ZnO blend films, X-ray diffraction (XRD) measurements have been carried out. Figure 4.08 shows the XRD spectrum of ZnO nanoparticles in powder form within the angle 2θ ranges between 10° and 80° . The XRD spectrum exhibits several diffraction peaks at scattering angles (2θ) of 31.7° , 34.4° , 36.2° , 47.5° , 56.6° , 62.8° , 66.5° , 67.9° , 69.2° , 72.7° and 77.0° that correspond to the reflection from (100), (002), (101), (102), (110), (103), (200), (112), (201), (004), and (202) crystalline planes, respectively (Yang,

Wang, Tang, Wang, & Zhang, 2005). The data obtained are found to be consistent with the Joint Committee on Powder Diffraction Standard (JCPDS) data of standard ZnO. This XRD pattern indicates that ZnO nanoparticles exhibit wurtzite structure.

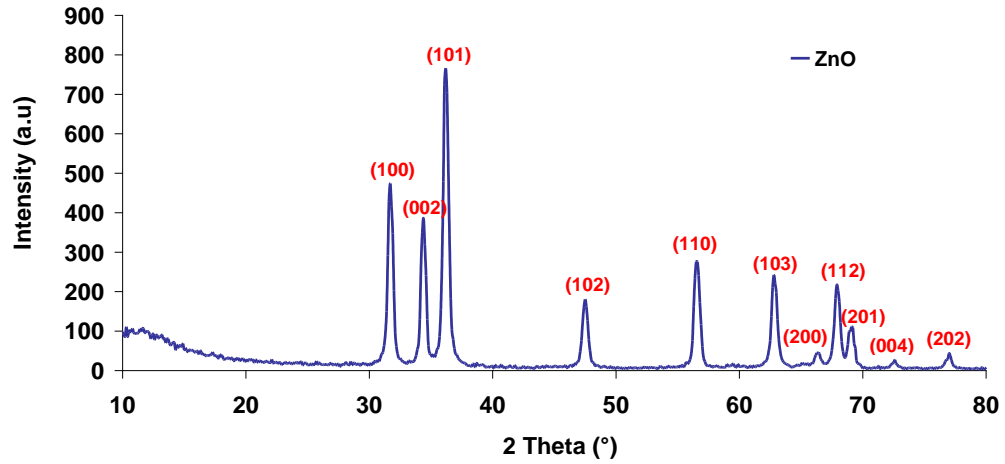


Figure 4.08: The XRD pattern of ZnO nanoparticles in powder form.

The separation distance between the lattice plane (d-spacing) which corresponds to the strongest peak at crystallographic plane (101) of ZnO is determined and found to be 0.25 nm by applying Bragg's equation (T. Erb et al., 2005; Zhokhavets, Erb, Hoppe, Gobsch, & Serdar Sariciftci, 2006) which is:

$$n\lambda = 2d \sin \theta \quad (4.5)$$

where n is an integer representing the order of XRD diffraction peak, d is the spacing distance between the lattice planes, θ is the Bragg diffraction angle, and λ is the wavelength of the X-ray radiation source (Here, $\text{CuK}\alpha$ radiation of 0.154 nm is used).

Typically, the broadening of peaks in the XRD spectrum shows that the particle size of ZnO is in the nanometer range. The size of the crystalline domain of the ZnO nanoparticles is determined according to the Debye-Scherrer formula (Warren, 1989):

$$t_c = \frac{C\lambda}{B \cos \theta} \quad (4.6)$$

where t_c is the crystallite size, B is the full width at half maximum (FWHM) of the diffraction peak which corresponding to (101) plane in radians, λ is the wavelength of

CuK α radiation (0.154 nm), θ is the Bragg angle, and C is a correction factor or known as the Scherrer constant which is taken as 1. Usually, the value of C depends on the shape and geometry of the particles, in which it is 0.94 for FWHM of spherical nanoparticles with cubic symmetry; 0.89 for spherical nanoparticles without cubic symmetry, or more often is taken as 1, as 0.94 and 0.89 both round up close to a value of 1 (Langford & Wilson, 1978). The estimated average crystallite size of ZnO nanoparticles at crystallographic plane (101) is found to be around ~20 nm.

In certain cases, the estimated crystallite size may not completely precise due to XRD peak broadening. The peak broadening profile can be ascribed to the presence of inhomogeneous microstrain that is usually produced by non-uniform lattice distortions, or intrinsic grain boundary dislocations as well (Budrovic, Van Swygenhoven, Derlet, Van Petegem, & Schmitt, 2004). In order to distinguish whether the peak broadening is induced by crystallite size or microstrain at FWHM of the XRD spectrum, the Williamson-Hall plot (Williamson & Hall, 1953) is exhibited in Figure 4.09. The strain and crystallite size can be determined from the intercept at the slope and y-axis, respectively, according to the given equation:

$$B \cos \theta = \frac{C\lambda}{t_c} + 2\varepsilon \sin \theta \quad (4.7)$$

where ε is the strain.

From Figure 4.09, the crystallite size and strain of the ZnO sample are found to be 19.49 nm and 2.50×10^{-4} . It is worth noting that this obtained crystallite size value is well-matchable to the previous data value determined from Scherrer's formula. Despite this, as it can be seen from the Williamson-Hall plot, the strain value is considered to be very small, and thus its effect on the peak broadening can be negligible.

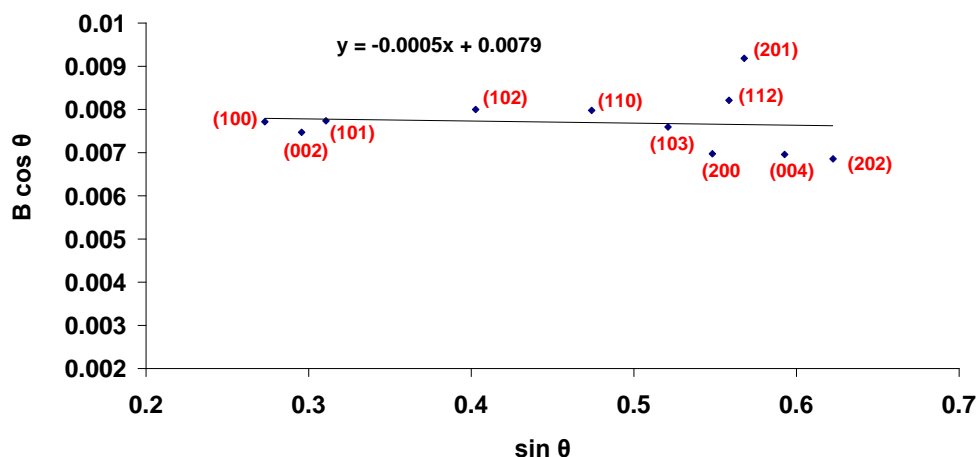


Figure 4.09: Williamson-Hall plots to determine the microstrain of ZnO.

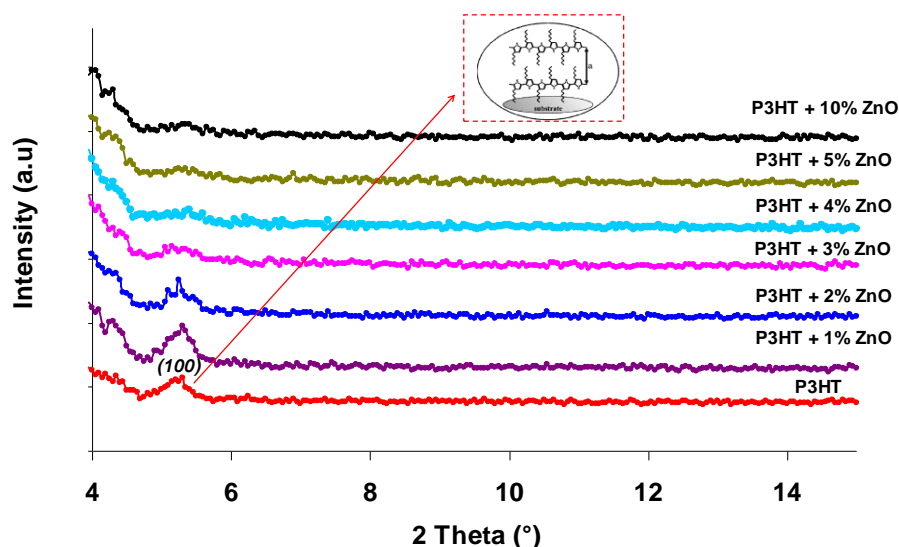


Figure 4.10: The XRD spectra of pristine P3HT and P3HT:ZnO blend films. The inset illustrates the orientation of P3HT crystallites with respect to the substrate.

Figure 4.10 illustrates the XRD patterns of pristine P3HT as well as the blends of P3HT:ZnO with different ZnO content. It can be observed that pristine polymer P3HT prepared in chloroform exhibits a peak around a 2θ value of 5.4° . In the measurement range between 0° to 15° , only one crystallographic plane of (110) is observed at that particular peak. This diffraction pattern corresponds to an organized lamellae structure with an interchain d-spacing which is formed by the polymer chains parallel to each others that divided by alkyl side-chains which fill the in-between spaces

(T. Erb, et al., 2005; Vanlaeke et al., 2006). Similarly, using the Bragg equation, the d-spacing for pristine P3HT and the blends, correspond to the primary (100) crystalline plane are calculated, as shown in Table 4.4. It is found that the values of d-spacing for the P3HT and its blends are between 1.68 and 1.70 nm. By comparing these values with the reported data of some literature reviews (Tobias Erb et al., 2006; Youngkyoo Kim et al., 2006; Warren, 1989), it suggests that the (100) peak originates from P3HT polymer crystallites with a-axis orientation, whereby the P3HT backbone structure is parallel to the glass substrate while the side chains tend to be perpendicular with respect to the substrate, as illustrated in the inset in Figure 4.10. However, the crystallite size along the b and c axis are hard to be identified based on this XRD measurement (T. Erb, et al., 2005). It can be observed from the obtained XRD spectra, the P3HT:ZnO nanoparticles blend films exhibit considerably small diffraction peak, which is mainly due to the crystallites phase of P3HT. The films mostly present as amorphous phase upon heavier doping of ZnO nanoparticles (>2% ZnO). Hence, the crystallization process upon the ZnO nanoparticles doping is considered to be negligible.

Table 4.4: Summary of the XRD properties of the P3HT:ZnO nanoparticles blend films with different ZnO content.

Samples	Bragg diffraction angle, 2θ ($\pm 0.01^\circ$)	d-spacing (± 0.01 nm)
Pristine P3HT	5.21	1.69
P3HT + 1% ZnO	5.26	1.68
P3HT + 2% ZnO	5.25	1.68
P3HT + 3% ZnO	5.22	1.69
P3HT + 4% ZnO	5.22	1.69
P3HT + 5% ZnO	5.22	1.69
P3HT + 10% ZnO	5.20	1.70

4.4 Morphological Characterization: Atomic Force Microscopy (AFM) and Field Emission Scanning Electron Microscopy (FESEM) Analysis

4.4.1 AFM Characterization

Basically, the BHJ hybrid film is a space-filling aggregated dispersion of nanoparticles throughout the polymer donor phase. In other hand, the BHJ can be referred as a bi-continuous solid dispersion of semiconducting components in terms of colloid. The dispersion of nanoparticles within the blend usually comprises of more than 90 vol. % solvent prior to solvent evaporation. In general, P3HT is more soluble in the organic solvent of CHCl_3 than that of inorganic nanoparticles. However, the nanoparticles remain dispersed, and hence a so-called binary nanoparticle-solvent system exists, until the volume fraction of nanoparticles surpasses a critical value which strongly depends on the nanoparticle geometry, composition, and nanoparticle-solvent interaction. Upon solvent evaporation, phase separation may begin to take place throughout the entire composite (Saunders & Turner, 2008).

In P3HT:inorganic nanoparticle solar cells, electron and hole transport through an interpenetrating network to reach the respective collecting electrodes are strongly responsible for a variation in solar cell efficiency. The quality of the donor and acceptor pathway networks can be reflected from the morphology of the blend film. To achieve an efficient charge transfer and charge transport, the film morphology should be of good quality. It should be likely free from pinholes, kinks and entangling of chains. Hence, the composition of donor and acceptor has to be optimized appropriately (Rait et al., 2007). Typically, a key challenge for hybrid solar cells is to well-control the aggregation scale within the nanoparticle phases in order to form optimal submicron or nanoscale phase separations to provide effective bicontinuous interpenetrating pathways for the charge transport to reach their respective electrodes, meanwhile the interfacial area of the D/A heterojunction has to be maximized to diminish the recombination losses (Beek, Wienk, Kemerink, Yang, & Janssen, 2005).

An important parameter in organic solar cells is the average distance taken by an exciton to travel before it decays to the ground state, or more preferentially is known as exciton diffusion length, which is basically dependent on the smoothness of the interface between the acceptor and donor phases (Huijser, Savenije, Shalav, & Siebbeles, 2008). The exciton diffusion length, Λ_E can be defined as follows:

$$\Lambda_E = (D_E \tau_E)^{\frac{1}{2}} \quad (4.8)$$

where D_E is the exciton diffusion coefficient and τ_E is the exciton lifetime. For P3HT, the exciton lifetime and diffusion coefficient are taken from the literature (Shaw, Ruseckas, & Samuel, 2008) as $\tau_E = 400$ ps and $\tau_E = 1.8 \times 10^{-7} \text{ m}^2 \text{ s}^{-1}$. As calculated using the equation (4.8), the Λ_E for P3HT is about ~9 nm. Hence, the average dimension size of phase separation is preferentially required to remain in nanometres range for better charge transport to take place.

To correlate the morphological properties of the blend films to the photovoltaic performances, atomic force microscopy (AFM) imaging studies with $10 \times 10 \text{ } \mu\text{m}^2$ scan in 3-dimension are performed to investigate the surface morphology of the pristine P3HT and its blend films, as shown in Figure 4.11((a)–(g)). The pristine P3HT shows a relatively smooth surface with a root-mean-square (RMS) roughness of only 1.1 nm as displayed in Figure 4.11(a). However, upon ZnO nanoparticles doping into P3HT, the surface roughness values of the blend films increase with the ZnO contents, as indicated in Table 4.5. This increment in roughness indicating an occurrence of phase separation between the P3HT donor and ZnO acceptor domains in the blends. With 1% ZnO added into P3HT, the blend film possesses a surface roughness of 4.5 nm, implying a good miscibility of P3HT and ZnO at low content of ZnO nanoparticles. In the case of the P3HT doped with 2% ZnO, the film morphology is slightly coarser than previous film (1% ZnO). Such blend composition dependent morphology has been clearly observed

for other composite films as well, according to the reported literature (Y. Kim, et al., 2005; van Duren et al., 2004).

A lower ZnO content (<4%) may yield in a finer phase separation and the molecules are closely arranged in the blend film. Thereby, it should be a higher probability for free charge carriers to recombine again before they manage to reach their respective electrodes due to the too closely arranged donor and acceptor domains with each others in a strongly fine composite (Koeppel & Sariciftci, 2006). In turn, the charge carriers may become more susceptible for charge trapping owing to the absence of clear, identified percolation paths for both charge transport to respective electrodes. On the other hand, at the moderate degree of fine phase separation, the ZnO clusters may preferably act as electron sinks, which aid to generate higher photocurrent due to an increased fraction of photogenerated charge carriers that able to escape from recombination. In this study, it is found that the optimum moderate degree of fine phase separation occurs at light ZnO doping of less than 4% in P3HT. The critical transport movement involved is not the diffusion of the exciton to the D/A interface but is the lateral movement of the electrons towards the nanoparticles clusters, as reported by Geens, W and his co-researchers (Geens et al., 2004).

Above 3% ZnO in blend, the films morphologies drastically change as can be seen from Figure 4.11((e)–(g)). For blend with 4% ZnO, the surface appears to be very inhomogeneous with the formation of uneven size of “islandlike” big clusters in the height above 50 nm with a surface roughness of 8.6 nm. This indicates that the ZnO-rich domains begin to agglomerate, resulting in large-scale phase separation and hence produce a higher surface roughness (Oosterhout et al., 2009). It is worth noting that upon heavier ZnO doping (>5%), the morphologies are much more different than that of the others. The coarse phase separation is clearly visible for sufficiently high content of ZnO nanoparticles in blends with the surface roughness up to 20.5 nm. As evidenced by

few research reports (Hoppe et al., 2004; Hoppe & Sariciftci, 2006), the coarse nanoscale morphology is unfavourable for high device efficiency. Thus, the large surface roughness for high loading ZnO (>5%) may yield in poor electrode contact and a higher number of defects on the films (Kwong et al., 2004), as supported by the previous XRD defects analysis results. Furthermore, the extensive nanoparticle aggregation leads to a larger scale of phase separation that builds up non-equilibrium blend film morphology. In the highly coarse surface morphology, the D/A interfacial area at which the exciton can be separated into free electron and hole becomes much more smaller. Since an important portion of light absorption is in the ZnO phase, the amount of photogenerated charge carriers are therefore reduced in the coarsely phase separated blend films. In such a condition, the efficiency of hybrid solar cells are seriously affected (Saunders & Turner, 2008). Therefore, a certain degree of nanoscale phase separation is desirable to form a better bicontinuous pathways network for efficient charge transport (Ma, Yang, Gong, Lee, & Heeger, 2005).

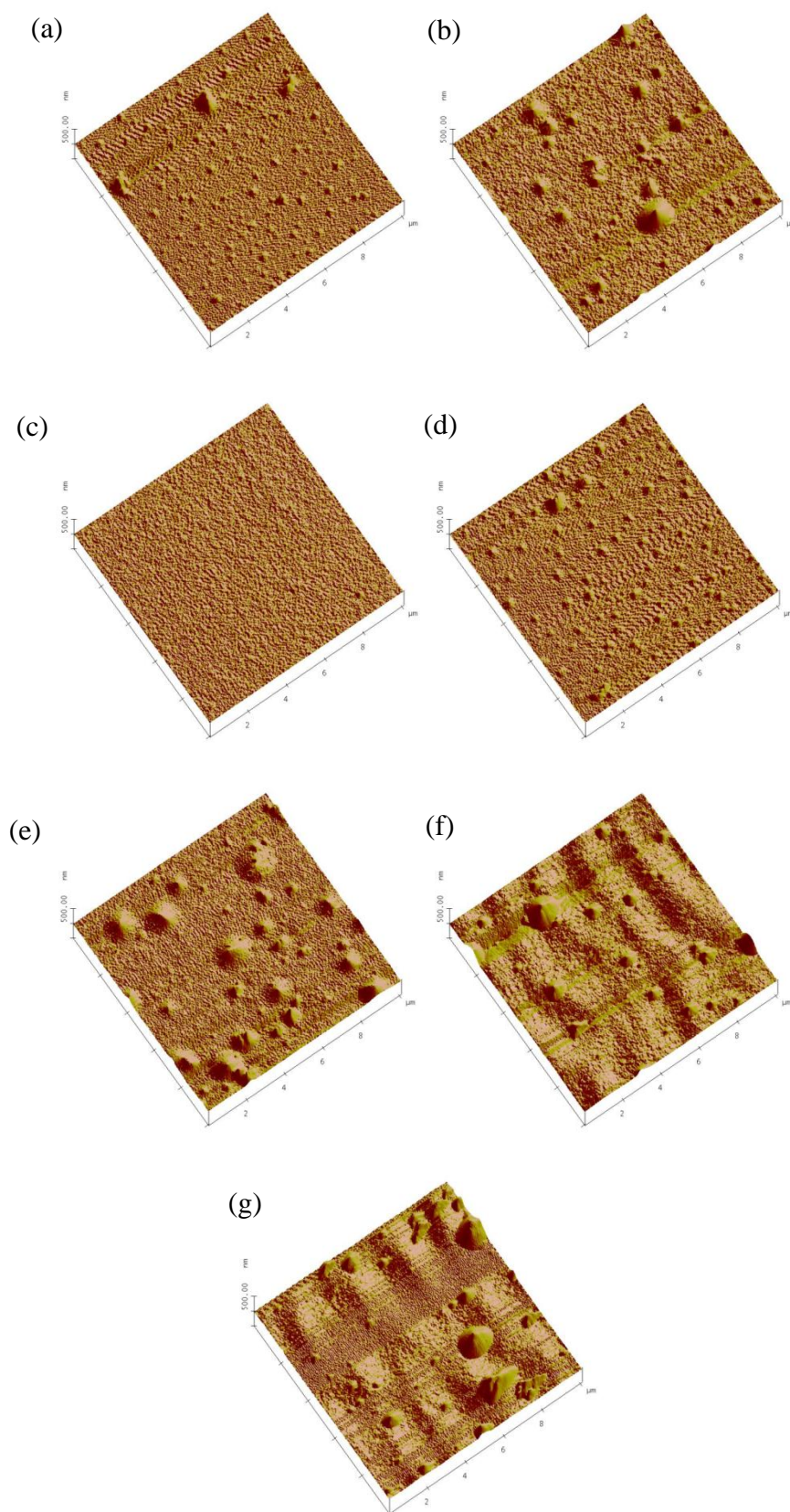


Figure 4.11: Three-dimensional AFM images by $10 \times 10 \mu\text{m}^2$ scan for (a) pristine P3HT and the blend films in different compositions with (b) 1%, (c) 2%, (d) 3%, (e) 4%, (f) 5%, and (g) 10% ZnO.

Table 4.5: The mean surface roughness and root-mean-square roughness of the films obtained from AFM for Figure 4.11.

Samples	Mean surface roughness, Ra (± 0.1) nm	Root-mean-square roughness, RMS (± 0.1) nm
Pristine P3HT	0.9	1.1
P3HT + 1 % ZnO	1.9	4.5
P3HT + 2 % ZnO	2.6	7.9
P3HT + 3 % ZnO	3.1	8.6
P3HT + 4 % ZnO	5.0	10.5
P3HT + 5 % ZnO	5.8	12.3
P3HT + 10 % ZnO	10.3	20.5

It is virtually not sufficient to judge the film quality solely by the film roughness. In certain cases, using post-treatment methods such as thermal annealing (Ma, et al., 2005; Padinger, Rittberger, & Sariciftci, 2003) and solvent annealing (Gang Li et al., 2005; G. Li et al., 2007) result in higher film roughness than the pristine film, but the device performances can be drastically improved as well. Hence, the main key point is possibly to be the formation of appropriate submicron or nanoscale phase separation.

Figure 4.12 shows all the obtained 2-dimensional (2D) contact mode AFM images for pristine P3HT film and its blends. For pristine P3HT film, there seem to be some small irregular objects on the film which most probably are some dust particles or other impurities (as indicated by light blue-colored dashed circles). Otherwise, it virtually exhibits a flat, homogenous topographical feature as shown in Figure 4.12(a). In contrast, the blend films in Figure 4.12((b)-(g)) show the topographical features of phase separation in different size dimension scales with surface textures varying drastically with blend composition. Even though the composition of the clusters are unable to be resolved solely based on AFM, it is still plausible to identify the bright areas of these contact mode AFM images in Figure 4.12 as the harder material of ZnO nanoparticles clusters and the dark areas as the softer material of P3HT polymer. In

addition, a few spherical-like ZnO aggregations can be obviously visualized in the AFM images (see Figure 4.12(b)-(g)) compared to that of the polymer film without ZnO (see Figure 4.12(a)). The visible darker stripe feature on the blend films is most likely due to the scratch-induced damages by the AFM probe tip, as indicated by the red-colored dashed circle in Figure 4.12(b).

As the concentration of ZnO increases and reaches 2% in blend, the AFM images of Figure 4.12(c) displays a bimodal size distribution of ZnO aggregates which can be attributed to the nucleation of a number of much smaller aggregates, forming ZnO clusters in diameter between ~130 nm to ~530 nm. These ZnO clusters are non-continuous with an average nearest neighbor distance (the separation distance between adjacent ZnO clusters) in submicron meter range. For example, the blend film with 3% ZnO (Figure 4.12(d)), it can be found that a few numbers of larger clusters are formed whereas smaller aggregates disappear. However, by increasing ZnO content of more than 3%, the larger island-like domains are formed by the extended, agglomerated ZnO clusters, as shown in Figure 4.12(e). Hence, these agglomerations of ZnO-rich domains are beneficial to the electron transport, as each separated electron may require less frequent transit or hopping movement between the adjacent domains. In fact, the excitons generated are within the diffusion range of a D/A interface which by the electron transfer take places merely within picoseconds time scale (Sariciftci, Smilowitz, Heeger, & Wudl, 1992). Once separated, the electron transport relies on non-conductive mechanism to travel from one domain to another domain (Hirsch, 1979; Nabok, 2005).

However, as the ZnO content increases up to 10% in blend, it can be observed from Figure 4.12(g) that the ZnO-rich domains have been agglomerated into micron-scaled domains. Consecutively, larger domain sizes of acceptor phases are formed. The estimated diameter of individual ZnO-rich domains varied from ~200 nm to ~2 μm .

Meanwhile, the average nearest neighbour distance of ZnO domains increased up to micrometer range, which indicates that the traveling distance taken by an exciton to reach the next domain has been prolonged to a longer extent and far exceeded their diffusion length. Hence, excitons generated in such domain are unable to diffuse towards the interface during their lifetime and have to decay before being dissociated into free charge carriers. Simultaneously, the extended ZnO phases cause the P3HT donor phase to shrink into a smaller volume, and hence destruct the percolation pathway for hole transport, yielding in an unbalanced charge transport for a hybrid solar cell (Yu, Liu, & Peng, 2008). This evolution process can be well-understood based on Ostwald mechanism where larger aggregates are favorably to grow and expand at the expense of the smaller aggregates in order to minimize the total energy of the interfacial surfaces. Hence, it leads to a reduction in the effective D/A interface area. These AFM studies clearly show an important correlation between film morphology and blend composition. It can be inferred that films below 3% ZnO offer better morphology qualities than of the films with higher ZnO content. This optimum ZnO content in the blend film has produced more uniform nanoparticles dispersions in the blends, meanwhile sufficiently large interface areas are still preserved over this range of compositions.

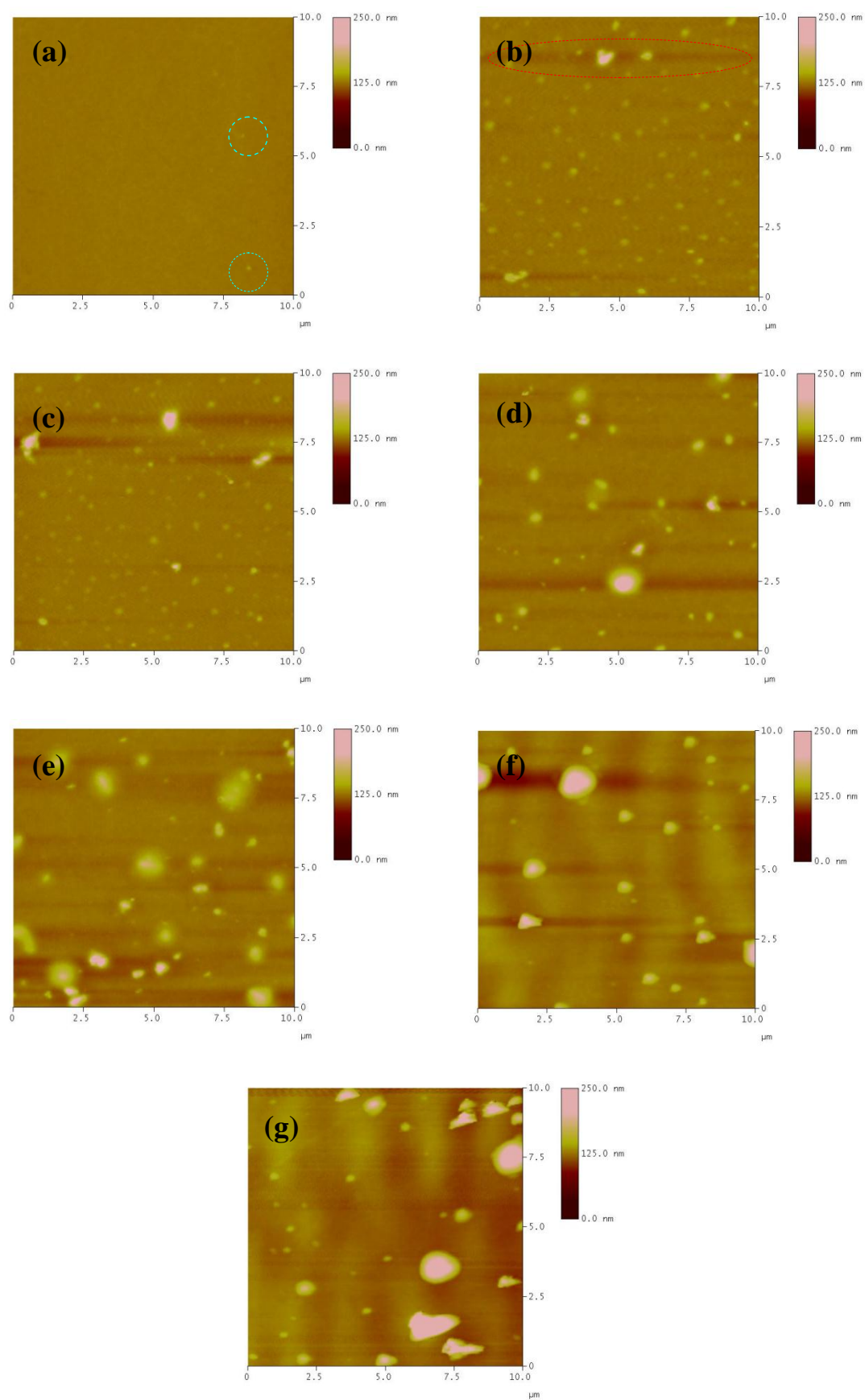


Figure 4.12: 2-dimensional AFM images of the (a) pristine P3HT and its blends with (b) 1%, (c) 2%, (d) 3%, (e) 4%, (f) 5%, and (g) 10% ZnO.

As a conclusion here, a clear explanation for some morphologies that most likely have been achieved for the P3HT:ZnO nanoparticle blends are schematically illustrated in Figure 4.13. The black dots of the figure represent nanoparticles that are tend to aggregate by the Van der Waal attractive force within the film, which are brought to be close enough to allow efficient electron hopping between particles. Figure 4.13(a) shows the optimal bicontinuous morphology for the blend film with small aggregates of nanoparticles separated by P3HT phase, upon the addition of a moderate content of ZnO nanoparticles. The formation of nice percolation pathways for both electron and hole to transport to the respective electrode improve the charge transport yield. However, if the ZnO content is too low as schematically illustrated in Figure 4.13(b), a limited extent of phase separation is formed with more isolated nanoparticles in film. Consequently, free electrons become more easily to be trapped at the dead end of pathways that affected the electron transport to cathode. On the other hand, the morphology shown in Figure 4.13(c) corresponds to the formation of extensive aggregation within the film with the increasing content of ZnO nanoparticles. In this case, inefficient charge separation may take place due to the resulted large extent of phase separation that destroying the percolation pathways for hole transport within the donor phase.

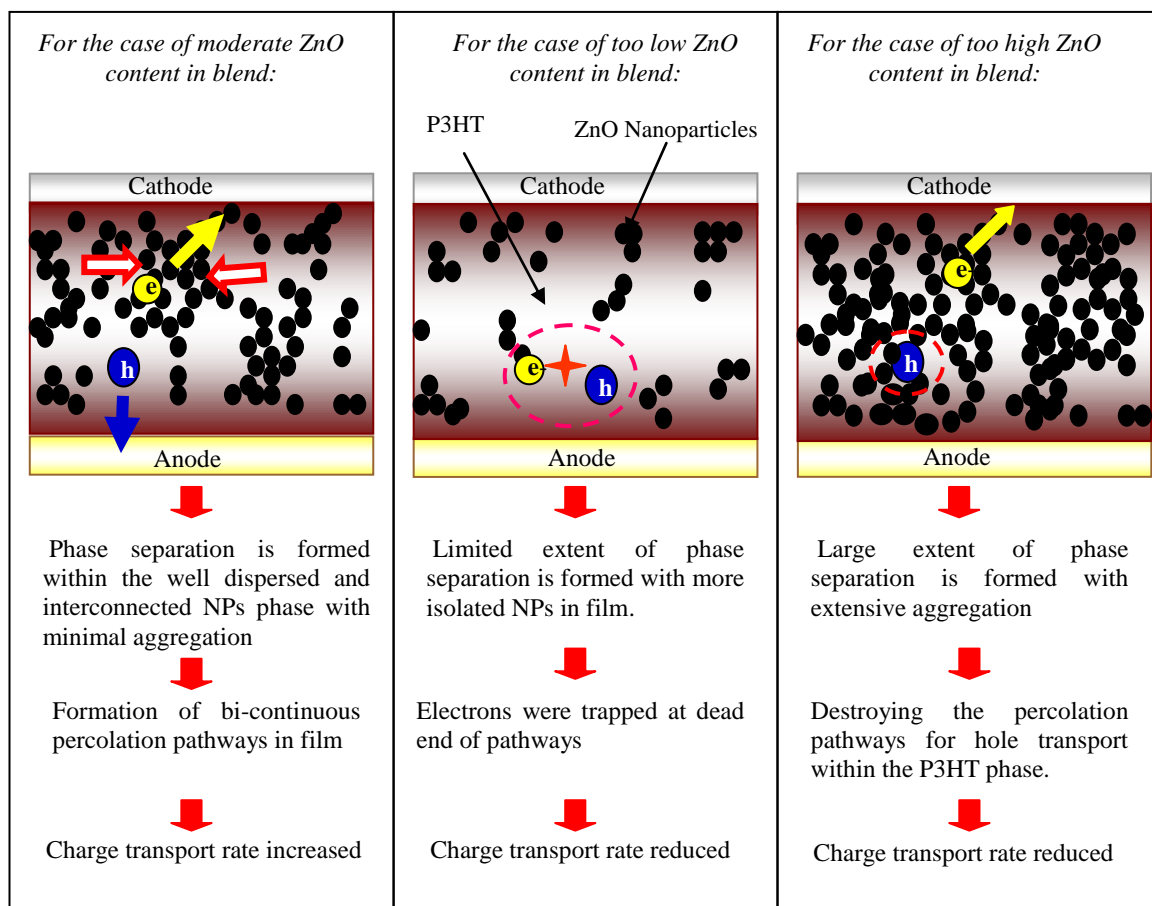


Figure 4.13: The schematic illustration of some possible morphologies that most likely have been achieved for the P3HT:ZnO blends incorporated with different amount of ZnO contents.

4.4.2 FESEM Imaging

The morphological properties of the blend films are studied via Ultra High Resolution Field-Emission Scanning Electron Microscopy (FESEM). Figure 4.14(a), (b), (c), (d) and (e) represent the FESEM images with the high resolution scale of 200 nm at magnification magnitude of 30k for pristine P3HT film and the blend films incorporated with 1% ZnO, 3% ZnO, 5% ZnO and 10% ZnO, respectively. From the results, it can be observed that P3HT films incorporated with different ZnO contents reveal slightly different patterns. The pristine P3HT film exhibits a nanoporous fiber-like structure with a fiber size in range between 40-130 nm, as displayed in Figure 4.15(a). After adding ZnO into P3HT, it is found that the sizes of nanoporous of the films become bigger with ~200 nm in diameter, as it can be obviously seen from the

images in Figure 4.14((b)–(e)). This can be deduced that the P3HT tends to agglomerate within the polymer phase due to the presence of extrinsic molecules of ZnO, which leads to an increased separation distance between the polymer chains themselves. Observing further from the blue circles in the images of Figure 4.14(e), it is worth identifying there are some nearly spherical particles with a diameter in nanometer range between 18-60 nm which are well-attached to the polymer fibers, as displayed in the focused image of Figure 4.14(e(ii)). This suggests that the ZnO inorganic nanoparticles have been homogeneously dispersed in the P3HT matrix, building up an interconnected donor and acceptor pathways network structure as it can be well-related to the formation of phase separation of D/A phases. Upon filling the space between the P3HT chains by the ZnO nanoparticles, the exciton dissociation interface area has been essentially enlarged, and more photogenerated excitons can reach the interface before geminate and bimolecular recombination (Saunders & Turner, 2008).

Nonetheless, the excess ZnO aggregates (>5%) in the film have seriously distorted the polymer chains structure of P3HT (see Figure 4.14(e)) which is in good agreement with the aforementioned optical absorption and XRD results. Figure 4.15 shows the FESEM image of pristine ZnO nanoparticles film (without P3HT) prepared from chloroform at a concentration of 10 mgml^{-1} via ultrasonication technique. This image reveals that the pristine ZnO nanoparticles are mostly in spherical shape and strongly aggregate in clusters form, hence yielding a larger diameter size in range around 60 nm up to 200 nm. Obviously, the particle size of individual nanoparticles is found relatively non-uniform and difficult to be estimated precisely due to their strong aggregation.

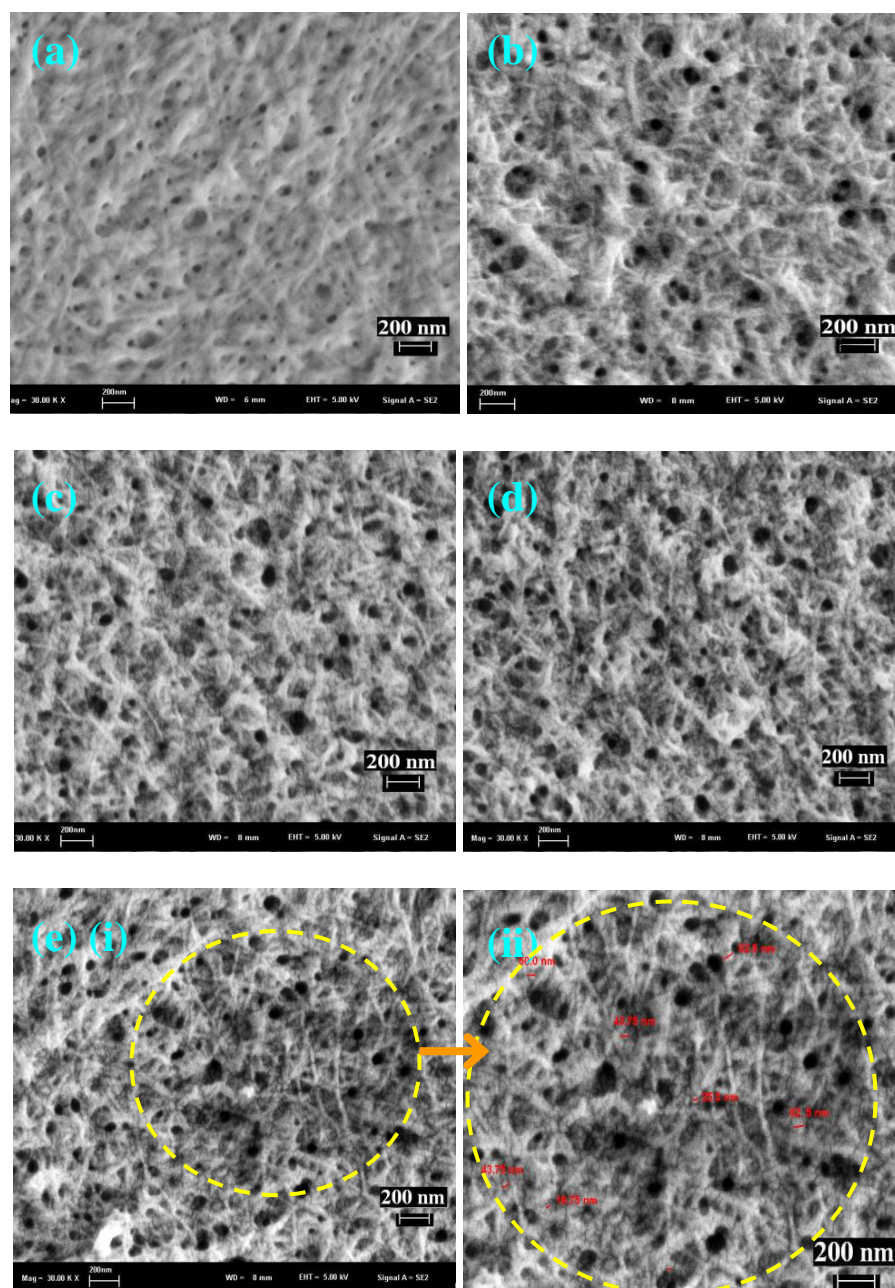


Figure 4.14: FESEM images of (a) P3HT and its blends with (b) 1%, (c) 3%, (d) 5% and (e) 10% ZnO ((e(ii)) shows the focused zone area of image (e)).

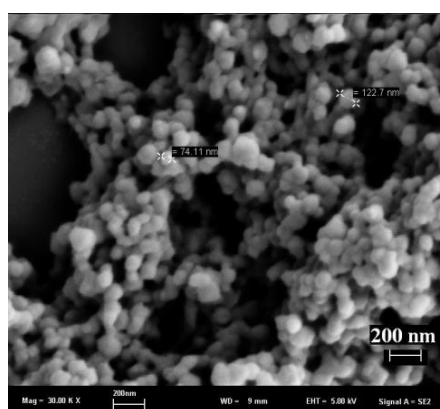


Figure 4.15: The FESEM images of pristine ZnO nanoparticles film.

4.5 Electrical Characterization: Current Density-Voltage (J-V) Curve Analysis

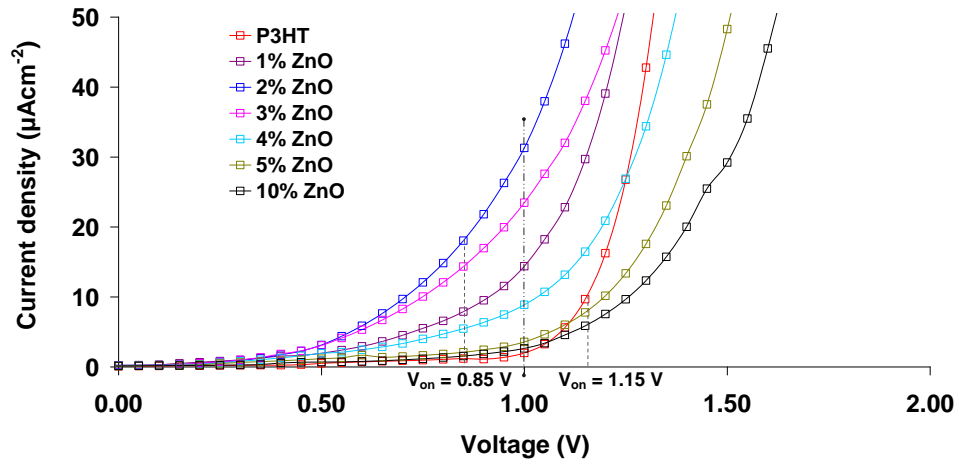


Figure 4.16: The current density–voltage (J-V) characteristics of solar cell devices based on pristine P3HT and P3HT:ZnO blends in different blend compositions under dark condition.

Figure 4.16 exhibits the current density–voltage (J-V) characteristics curves of the ITO/PEDOT:PSS/P3HT/Al and ITO/PEDOT:PSS/P3HT:ZnO/Al devices with different ZnO contents in the dark condition. Without light illumination, the devices exhibit the common diode-like characteristics. From the J-V curves, it can be seen that the pristine P3HT based device obtains the lowest electrical current than that of the P3HT:ZnO blend film based devices at the same applied positive bias voltage (for example, at +1.00 V). It should be noted that the device consist of P3HT blended with 2% ZnO, achieves the highest electrical current than the other devices and the value is greater by a factor of 15.7 compared to that of without ZnO. This suggests that P3HT:ZnO-based devices possess a higher charge mobility than the pristine P3HT-based device since it is virtually well-related to a better electrical conduction characteristic. In addition, it can be observed from Figure 4.16 that the turn-on voltage of the blend devices with less than 4% ZnO is significantly reduced. For example, devices with 2% and 3% ZnO in the blends exhibit a smaller turn-on voltage, V_{on} of around 0.85 V, whereas pristine P3HT device has a higher V_{on} of 1.15 V. This reduced

value of V_{on} upon introducing ZnO into P3HT has decreased the barrier height at the interface between photoactive layer and the collecting electrode. Besides, this smaller V_{on} value can be ascribed to the better charge injection from the blends which comprising of both hole (donor P3HT) and electron-conducting (acceptor ZnO) components through the electrode contact as well, and hence yields a higher electrical conduction than the device consist of solely hole-conducting component of P3HT (Sulaiman & Fakir, 2011).

However, it is worth noted that for blend devices consist of $>4\%$ ZnO, the V_{on} values become larger and exhibit considerably low electrical current contribution at the applied voltage of $+1.00$ V than the blend devices with $<4\%$ ZnO. This is presumably because of an increased built-in potential due to a band gap shift under Burstein-Moss effect. The Fermi energy level is pushed towards valence band as the density of occupied states increases upon heavier ZnO doping (p-type doping) (Grundmann, 2006).

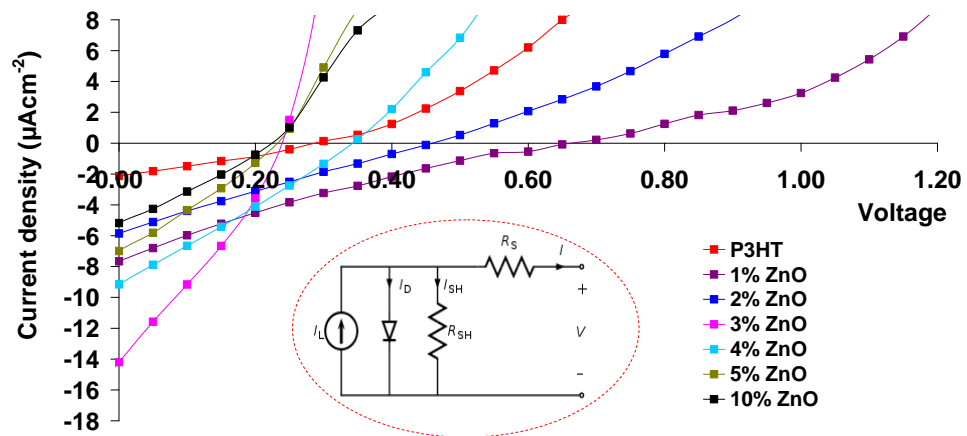


Figure 4.17: Current density-voltage (J-V) characteristic curves of the solar cell devices under light illumination. The inset displays an equivalent circuit diagram of solar cells which consists of series resistance, R_s and shunt resistance, R_{sh} .

Table 4.6: The comparison of device characteristics parameters for pristine P3HT and P3HT:ZnO solar cells with different ZnO concentration.

Samples	J_{sc} (μAcm^{-2})	V_{oc} (V)	FF	η ($10^{-3}\%$)
Pristine P3HT	2.13	0.28	0.29	0.17
P3HT + 1 % ZnO	5.86	0.47	0.23	0.63
P3HT + 2 % ZnO	7.67	0.66	0.20	0.97
P3HT + 3 % ZnO	14.20	0.24	0.30	1.1
P3HT + 4 % ZnO	9.16	0.32	0.28	0.82
P3HT + 5 % ZnO	7.00	0.23	0.27	0.44
P3HT + 10 % ZnO	5.18	0.22	0.26	0.31

Figure 4.17 shows the current density-voltage (J-V) characteristic curves of the solar cell devices under white light illumination at $100mWcm^{-2}$. The device parameters of the short-circuit current density (J_{sc}), open-circuit voltage (V_{oc}), fill factor (FF) and device efficiency (η) that corresponding to the solar cells made of pristine P3HT and P3HT:ZnO blends with different ZnO contents are tabulated in Table 4.6. As shown in Figure 4.17 and Table 4.6, the photovoltaic properties of the hybrid solar cells exhibit interesting changes with the variation in blend composition. The J_{sc} of the pristine P3HT device is $2.13 \mu Acm^{-2}$ and the V_{oc} is 0.28 V, with a FF and η of 0.29 and 0.17E-3%, respectively. Upon the ZnO doping into P3HT, the blend devices exhibit enhanced device performance. Among all the devices, device made of P3HT with 3% ZnO achieves the best photovoltaic performance with a high J_{sc} of $14.20 \mu Acm^{-2}$ and a V_{oc} of 0.24 V, and thus the corresponding FF and η increase to 0.30 and 1.10E-3 %, respectively. This indicates that this device possesses a more balanced and rapidly charge transport than devices with other blend composition (Huynh, Peng, & Alivisatos, 1999).

Typically, the charge mobility rises with increasing the nanoparticle concentration as reported in other references by Choudhury and his co-researchers (Choudhury, Winiarz, Samoc, & Prasad, 2003). However, a balance point between the

electron and hole transport is still a prerequisite for efficient device performance since electron typically possesses much higher mobility than that of hole. Here, the value of FF of the device is used as a measure for the balance of charge transport (Beek, et al., 2005). The high FF value of 0.30 achieved by P3HT with 3% ZnO-based device is an indicator of the better solar cell performance, which implying that both electron and hole mobility have reached the required balance point, and hence results in more efficient charge transport. A larger FF value is thereby able to yield a more square-like I-V sweep which results in higher device efficiency, as indicated in Figure 4.17.

Another possible reason for the enhancement in η is the increase in exciton dissociation interfacial area through the dispersion of ZnO nanoparticles within the P3HT phase. One of the most crucial parameters which determine the exciton dissociation yield and overall device performance is the alignment of the energy levels of the blend components as well as the electrode contacts. A deduced schematic energy band diagram for the P3HT:ZnO nanoparticle hybrid system, inserted between anode ITO and cathode Al is presented in Figure 4.18.

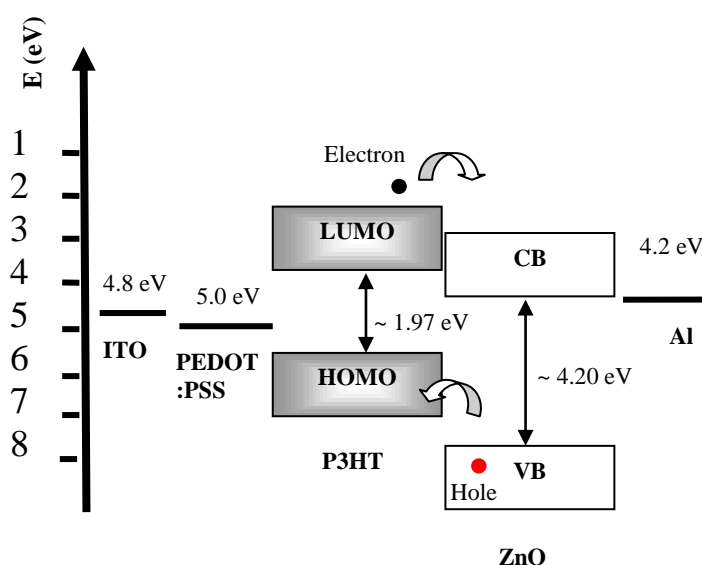
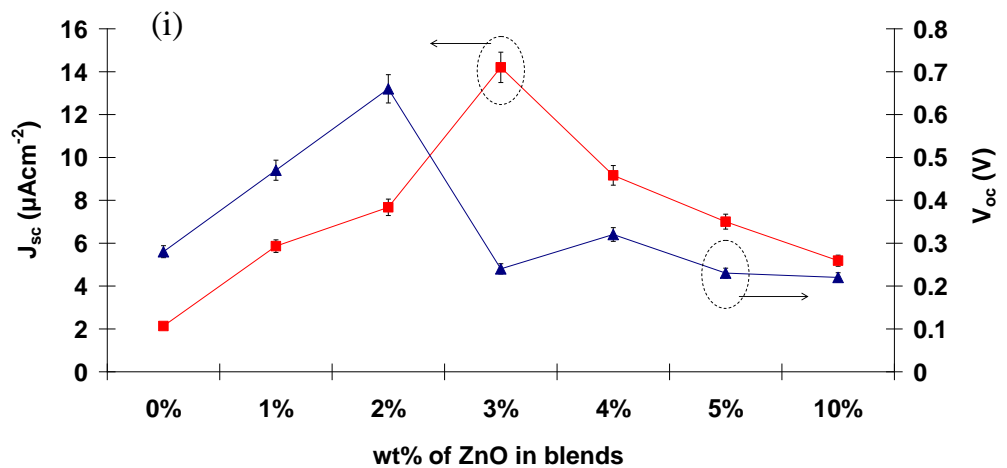


Figure 4.18: The schematic energy band diagram of ITO/PEDOT:PSS/P3HT:ZnO/Al devices.

From Figure 4.18, it can be observed that P3HT possesses the lowest unoccupied molecular orbital (LUMO) at around 3.2 eV, whereas ZnO has a CB energy value of around 4 eV. Apparently, there is a considerably large energy offset of the LUMO levels for both materials, indicates that the created driving force for exciton dissociation and charge transfer is large enough to overcome the exciton binding energy in P3HT, and hence a larger potential gain in V_{oc} can be obtained compared to that of pristine P3HT device (Boucle, Ravirajan, & Nelson, 2007). It is interesting to notice from Table 4.6 and Figure 4.19(i) that both of the J_{sc} and V_{oc} remarkably change with the variation in blend composition. Upon the ZnO doping, the J_{sc} drastically increases up to blend with 3% ZnO from $2.13 \mu\text{Acm}^{-2}$ to $14.20 \mu\text{Acm}^{-2}$, which can be attributed to the enlarged exciton dissociation interface area and improved charge transport. In addition, an optimal increment in film thickness and absorption coefficient can be considered to be partly responsible for the increase in J_{sc} due to the enhanced absorption and photogeneration rate (L.-M. Chen, Hong, Li, & Yang, 2009).



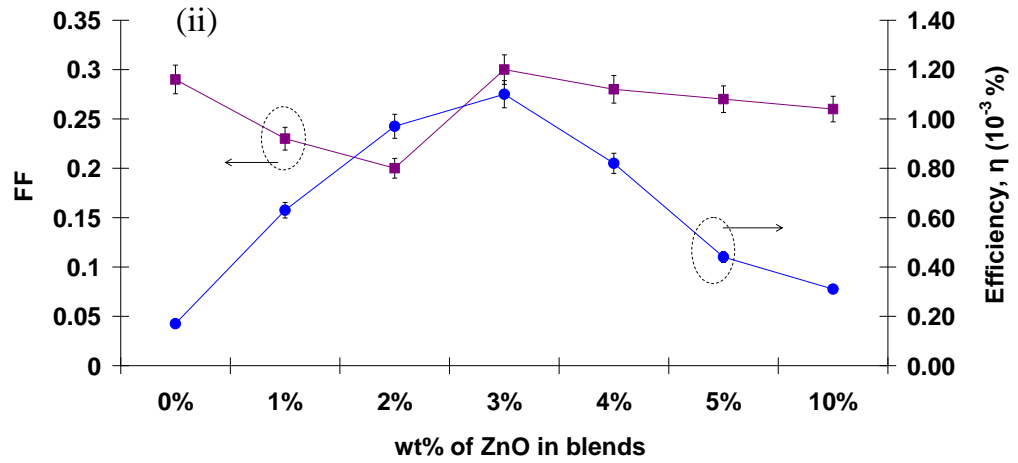


Figure 4.19: The variation of (i) J_{sc} and V_{oc} , (ii) FF and η with the blend composition.

For device consists of >4% ZnO doping, both the J_{sc} and V_{oc} are found substantially drop from $14.20 \mu\text{Acm}^{-2}$ to $5.18 \mu\text{Acm}^{-2}$ and 0.66 V to 0.22 V , respectively. Even though the variation trend in V_{oc} is still hard to be explained in this hybrid system, it is still found to be in partly agreement with other reported results (Beek, et al., 2005; Zhu et al., 2008). A reasonable explanation of this ZnO concentration dependence of V_{oc} is most likely related to the formation of shunt paths (or known as alternative high-conducting paths across the heterojunction solar cell or around the cell edge) in the blend devices. These types of shunt are mainly due to the existence of defects, impurities or crystal damage in device and are seriously detrimental to the solar cell performances (McMahonx & Bennett, 1996). Upon heavier ZnO doping, a larger number of electron-conducting ZnO nanoparticles are brought to contact with the hole-collecting anodes of PEDOT:PSS/ITO interface layer that result in more shunt paths for charge carriers to transport within the blend devices. This can be evidenced from a sharp decrease trend in shunt resistance (the resistance in the shunt path) which will be discussed in advance later. Accordingly, it yields a higher rate of photocurrent loss and the V_{oc} of the hybrid device is therefore has been significantly reduced (see the equivalent circuit diagram of solar cell in the inset of Figure 4.17).

Moreover, both the J_{sc} and V_{oc} are essentially affected by different films morphologies as well (Liu, Shi, & Yang, 2001). This can be observed for device with >3% ZnO contents, it is found that the photocurrent generation is still relatively low (Table 4.6 and Figure 4.19(i)) which is more likely due to the recombination of the isolated free charge carriers. As discussed previously, when the ZnO concentration is too low, isolated nanoparticles may favorably cause charges build up and hinder further charge transfer to take place within the interface vicinity (Arango, Carter, & Brock, 1999). The electrons are more easily trapped at isolated ZnO nanoparticles due to discontinuities in the ZnO percolation pathways and eventually may recombine with the holes in the P3HT matrix, and hence result in a lower efficiency (Moule, Chang, Thambidurai, Vidu, & Stroeve, 2012). With increased ZnO content (devices with ZnO content above 5% ZnO), even though the recombination rate might possibly be reduced, but poor quality film morphologies with the formation of large-scale phase separation that cause a disruption to the interpenetrating donor pathway are obtained, as evidenced in the AFM and FESEM images. As a result, the device performances begin to deteriorate and low efficiencies are obtained (Huynh, et al., 1999).

Typically, during the photovoltaic operation in a real solar cell, the device efficiency can be significantly reduced by the power dissipation through the bulk internal resistances of the photoactive layer and the contact resistance between the electrode and photoactive layer and through the surface leakage currents around the device circuit. These effects correspond to two types of parasitic resistances, namely are series resistance (R_s) and parallel shunt resistance (R_{sh}), respectively. Table 4.7 and Figure 4.20 indicate the variation of both R_{sh} and R_s values of the solar cell devices which have been estimated from the J-V curves under light illumination condition. Often, both R_s and R_{sh} are important key factors for high fill factor and good device performance. To achieve efficient cell, R_{sh} should be as large as possible in order to

reduce the leakage current through alternative path, while R_s is required to be small to prevent further voltage drop before the load. Thus, by decreasing R_s and increasing R_{sh} , the FF and efficiency can be improved. An excess decrease of the R_{sh} may cause the V_{oc} drops, while increasing R_s too intensely may reduce the value of J_{sc} . R_{sh} is determined from the inverse slope near to the bias voltage of 0 V (the slope at J_{sc}) whereas the R_s can be obtained from the inverse slope at a positive bias voltage (the slope at V_{oc}). Thereby, the following expressions are derived (Bouzidi, Chegaar, & Bouhemadou, 2007; Chan, Phillips, & Phang, 1986):

$$R_{sh} = -\frac{dV}{dI} \bigg|_{V=V_{oc}} \quad (4.9)$$

$$R_s = -\frac{dV}{dI} \bigg|_{J=J_{sc}} \quad (4.10)$$

Table 4.7: The variation of R_{sh} and R_s with the blend composition.

Samples	$R_{sh} (\pm 0.1 \text{ k}\Omega\text{cm}^{-2})$	$R_s (\pm 0.1 \text{ k}\Omega\text{cm}^{-2})$
Pristine P3HT	152.9	106.1
P3HT + 1 % ZnO	53.8	92.8
P3HT + 2 % ZnO	62.6	81.7
P3HT + 3 % ZnO	53.0	9.8
P3HT + 4 % ZnO	38.1	28.2
P3HT + 5 % ZnO	33.8	22.6
P3HT + 10 % ZnO	43.5	28.3

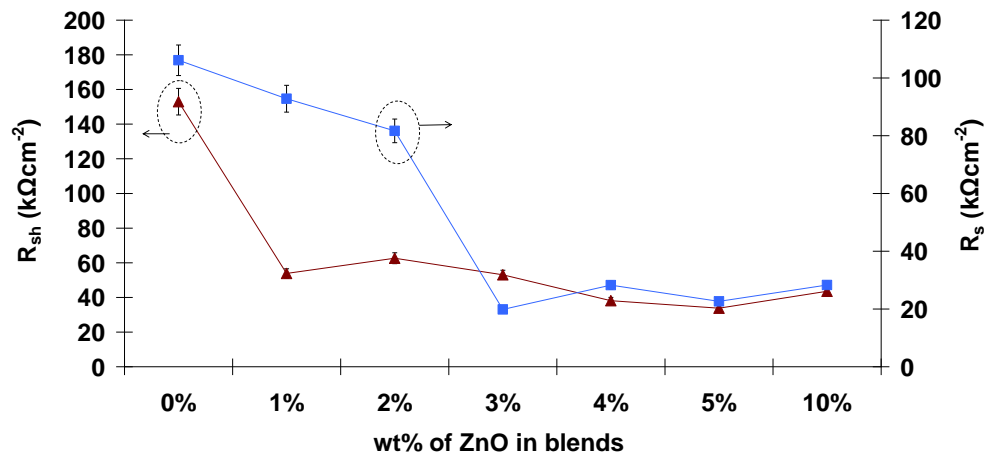


Figure 4.20: The variation of R_{sh} and R_s with the blend composition.

As evidenced by Table 4.7 and Figure 4.20, the device with pristine P3HT has the highest R_s of $106.1 \text{ k}\Omega\text{cm}^{-2}$ despite of a high R_{sh} value of $152.9 \text{ k}\Omega\text{cm}^{-2}$ which might responsible for the poor device performances. In contrast, the blend devices exhibit fairly low R_{sh} (except for the device with 1% ZnO) and reduced R_s with the ZnO content. Among all of these devices, the blend device with 3% ZnO exhibits the lowest R_s value of $9.8 \text{ k}\Omega\text{cm}^{-2}$ and sufficiently high R_{sh} of $53.0 \text{ k}\Omega\text{cm}^{-2}$, and therefore yields the highest J_{sc} and device efficiency. However, there is no significant rise in R_s value after the addition of 5% ZnO in blend. This suggests that the blend composition is still showing some profound effects on the device resistances since the J_{sc} values of blend devices have been remarkably increased than that of pristine P3HT device due to the incorporation of ZnO nanoparticles and begin to decrease with much more higher amount of ZnO in blends. In fact, the coarse surface morphology of the devices with higher ZnO content (as seen in the AFM images of Figure 4.11) can result in a gradual increase in R_s , which leads to the bottlenecks in charge transfer within the photoactive layer and between the photoactive layer and collecting electrodes as well (Nelson, Kirkpatrick, & Ravirajan, 2004). Hence, the photocurrent generation and device efficiency have been decreased which is consistent with what is expected.

As a conclusion for this chapter, in order to achieve a good device performance, several factors need to be taken account in advance including the enhanced light absorption with optimal film thickness, better quality film morphology with optimal extent of phase separation, increased exciton dissociation interface area together with a well-balanced charge mobility and appropriate energy alignment with respect to each others.

CHAPTER 5

HYBRID SOLAR CELLS BASED ON INORGANIC NANOPARTICLES AND P3HT:ZNO ACTIVE LAYERS PREPARED BY SOL-GEL SYNTHESIS ROUTE

5.1 Overview

The content of this chapter is divided into two main parts. The first part reveals the significant effects of two types inorganic materials, namely TiO_2 and Y_2O_3 metal oxide nanoparticles on the physical and electrical properties of hybrid blend films. In this part, a comprehensive investigation and comparison are also being made on the hybrid devices based on blends of P3HT and three different types of inorganic nanoparticles. The second part presents device improvement for P3HT:ZnO hybrid systems via ZnO sol-gel synthesis route. Additionally, three different physical approaches are presented along with their effects on the device performances, i.e., varying the sol content in P3HT blends, application of different annealing temperature, and inserting an additional ZnO buffer layer between the active layer and metal electrode.

5.2 Part I: Investigation of Hybrid Solar Cells Based on Various Inorganic Nanoparticles.

5.2.1. Results on P3HT: TiO_2 Blend Films and Their Based Solar Cell Devices

A. Optical Characterization

Figure 5.01 shows the absorption coefficient spectra of the pristine P3HT, TiO_2 and P3HT: TiO_2 blend films with different contents of TiO_2 . Similar to the case of P3HT:ZnO blends, the P3HT film exhibits a strong absorption in the visible wavelength range from 450-650 nm, whereas the TiO_2 nanoparticles film is found to absorb light in the UV wavelength range from 200-400 nm with an absorption onset around 311 nm. Upon the incorporation of TiO_2 into P3HT, the absorbance in the UV-Visible range

increases from $(17.4 \text{ to } 20.7) \times 10^4 \text{ cm}^{-1}$, and then drops gradually for $>4\%$ of TiO_2 in the blends. The films thickness slightly increases with the increment of TiO_2 contents. On the other hand, the E_g values for the blend films tend to gradually decrease from 1.97 eV to 1.94 eV and reach the smallest value for blend with 4% of TiO_2 . These obtained results of $\text{P3HT}:\text{TiO}_2$ are found to follow the similar patterns with the previous case of $\text{P3HT}:\text{ZnO}$ hybrid system in which an optimal amount of TiO_2 content is required to enhance the light absorption over broader wavelength regime and simultaneously able to reduce the optical band gap of the blends to increase optical $\pi-\pi^*$ transition rate (Sergio et al., 2010).

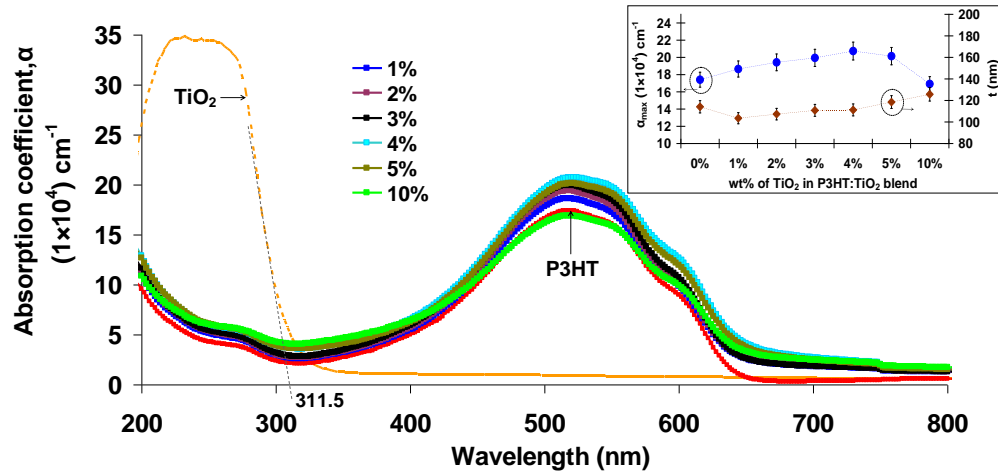
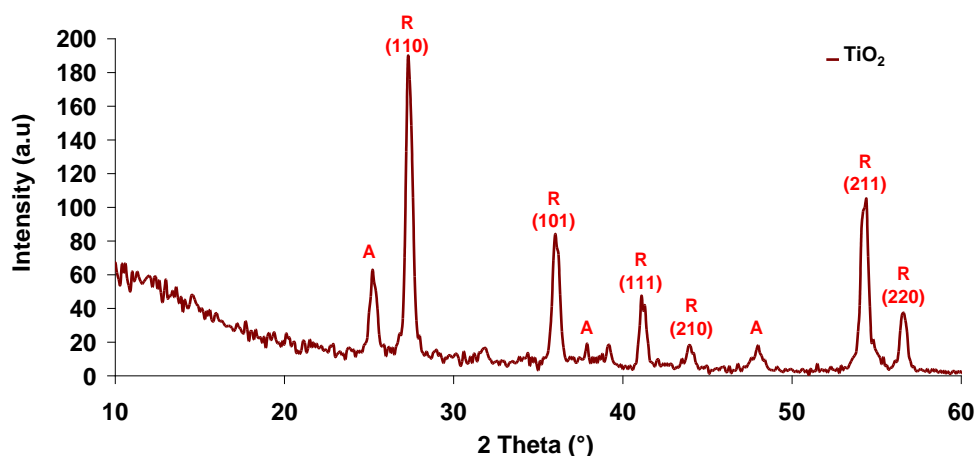


Figure 5.01: Absorption coefficient of $\text{P3HT}:\text{TiO}_2$ blend films with different contents of TiO_2 nanoparticles. The inset shows the variation of maximum absorption coefficient peak values, α_{max} and film thickness, t as a function of TiO_2 contents.

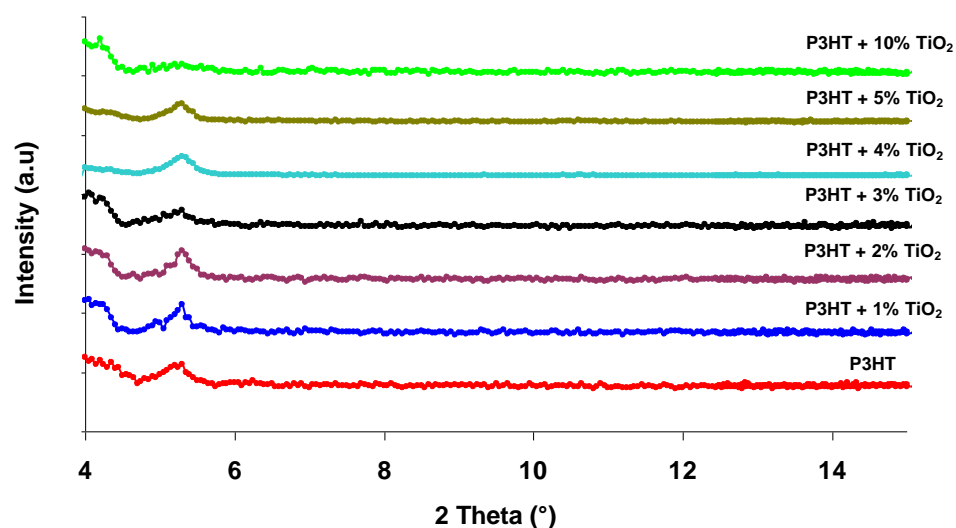
Table 5.1: Summaries of the α_{max} values together with the corresponding wavelength positions, λ , film thickness, t and estimated E_g for pristine P3HT and $\text{P3HT}:\text{TiO}_2$ blends.

Samples	α_{max} (1×10^4) cm^{-1}	λ (nm)	t (nm)	E_g (eV) (± 0.01 eV)
Pristine P3HT	17.4	518	114.1	1.97
Pristine TiO_2	34.9	232	115.0	4.23
$\text{P3HT} + 1\% \text{ TiO}_2$	18.6	518	103.5	1.96
$\text{P3HT} + 2\% \text{ TiO}_2$	19.4	518	107.3	1.96
$\text{P3HT} + 3\% \text{ TiO}_2$	19.9	520	110.8	1.96
$\text{P3HT} + 4\% \text{ TiO}_2$	20.7	520	111.2	1.94
$\text{P3HT} + 5\% \text{ TiO}_2$	20.1	520	118.5	1.95
$\text{P3HT} + 10\% \text{ TiO}_2$	16.9	520	125.7	1.95

B. Structural Characterization



(i)



(ii)

Figure 5.02: The XRD patterns of (i) TiO₂ in powder form; (ii) pristine P3HT and P3HT:TiO₂ blend films.

Table 5.2: Summaries of the Bragg diffraction angles and film roughnesses (obtained from AFM images) of pristine P3HT and P3HT:TiO₂ blends.

Samples	Bragg diffraction angle, 2θ (± 0.01°)	Film roughness (± 0.1 nm)
Pristine P3HT	5.21	1.1
P3HT + 1% TiO ₂	5.27	2.2
P3HT + 2% TiO ₂	5.30	3.1
P3HT + 3% TiO ₂	5.22	6.2
P3HT + 4% TiO ₂	5.29	10.5
P3HT + 5% TiO ₂	5.26	22.1
P3HT + 10% TiO ₂	5.25	37.7

Figure 5.02 shows the XRD spectra of TiO₂ powders, pristine P3HT, and the blend films. TiO₂ thin film does not produce apparent XRD peak, thus the TiO₂ in powder form is used. All the regarding data are summarized in Table 5.2. As indicated in Figure 5.02(i), the TiO₂ nanoparticles comprise of major phase of rutile phase (27.4°, 36.0°, 41.2°, 44.1°, 54.4°, and 56.6°) with the minor anatase phase (25.2°, 37.9°, and 48.0°). The diffraction peak at $2\theta \approx 27.4^\circ$ shows the strongest intensity. This peak corresponds to the crystal lattice plane of (110) for the TiO₂ structure with d-spacing of 0.33 nm and crystallite size of about 20 nm. The XRD result of TiO₂ is in agreement with that previously reported data (Y. Wang, Sun, & Li, 2009). For the spin-coated P3HT:TiO₂ blend film, a small crystalline peak at 2θ in the range of 5.20° to 5.30° in the diffractogram is observable which corresponding to the first-order reflection of P3HT polymer chains that well dispersed within the TiO₂ domains (Zhokhavets, Erb, Hoppe, Gobsch, & Serdar Sariciftci, 2006). Such a small XRD peak indicates that the P3HT:TiO₂ blend films are largely amorphous phase. Furthermore, the crystalline peak of TiO₂ can not be detected by means of the thin film form which is ascribed to the formation of large distribution of possible molecular packing during the dilution of the TiO₂ powder in the solvent and spin-coated onto glass substrates. These XRD spectra of the P3HT:TiO₂ blend film are found to be in accordance to the results obtained for P3HT:ZnO films in which the crystallinity of P3HT is disrupted by excess TiO₂ nanoparticles loadings (Erb et al., 2005).

C. Morphological Characterization

Figure 5.03 shows the AFM images of P3HT:TiO₂ blend films, while the surface roughnesses of these films are indicated in Table 5.2. All the blend films are seemed to be homogeneous except for some small submicron-scaled spheres that are randomly dispersed throughout the composite. However, it can be noticed that the blend film images in Figure 5.03((f) & (g)) exhibit a drastic increment in the peak height and cluster size with irregular shape with the increasing TiO₂ content. This yields a remarkably increase in the film roughness, rising from 2.2 nm to above 37.7 nm.

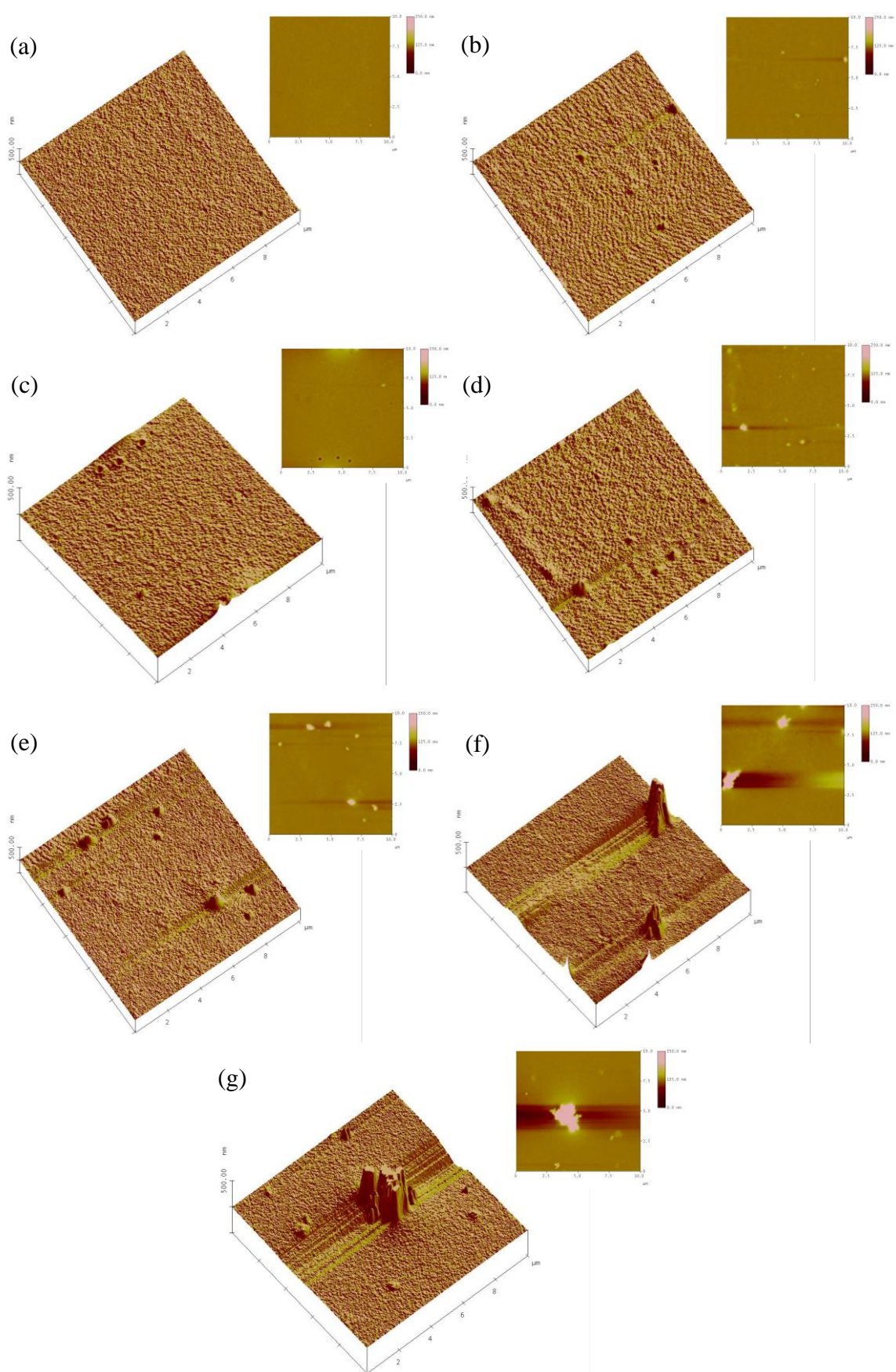


Figure 5.03: AFM images in 2D and 3D views for (a) pristine P3HT and P3HT:TiO₂ blend films with (b) 1%, (c) 2%, (d) 3%, (e) 4%, (f) 5%, and (g) 10% TiO₂.

D. Electrical Characterization

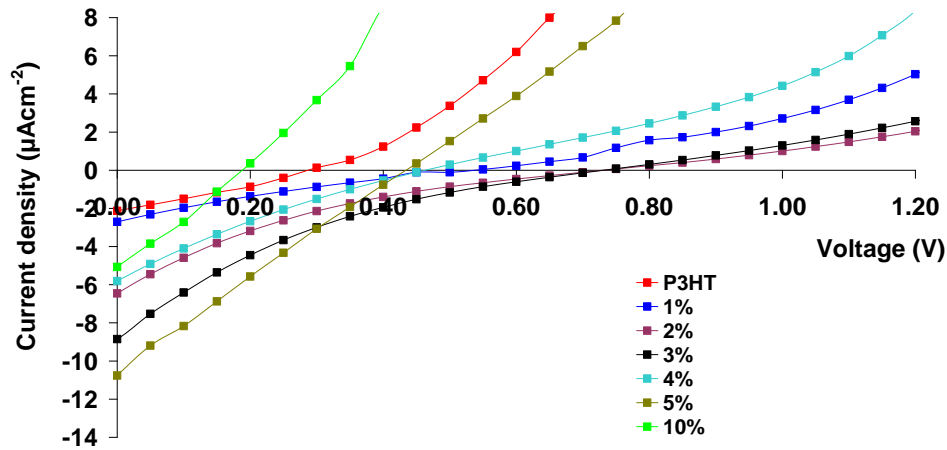


Figure 5.04: The J-V plots for P3HT:TiO₂ solar cells with different blend compositions under light illumination.

Table 5.3: The comparison of device characteristics parameters for P3HT:TiO₂ solar cells.

Samples	J_{sc} (μAcm^{-2})	V_{oc} (V)	R_{sh} (± 0.1 $k\Omega cm^{-2}$)	R_s (± 0.1 $k\Omega cm^{-2}$)	FF	η ($10^{-3}\%$)
Pristine P3HT	2.13	0.28	152.9	106.1	0.29	0.17
P3HT + 1 % TiO ₂	2.71	0.52	121.5	334.8	0.19	0.28
P3HT + 2 % TiO ₂	6.46	0.72	46.5	282.5	0.14	0.66
P3HT + 3 % TiO ₂	8.86	0.74	49.0	225.2	0.15	0.92
P3HT + 4 % TiO ₂	5.81	0.46	52.9	124.1	0.20	0.54
P3HT + 5 % TiO ₂	10.77	0.43	31.1	43.7	0.24	1.01
P3HT + 10 % TiO ₂	5.07	0.18	38.6	33.7	0.23	0.27

The blend composition dependence of the device performances of hybrid solar cells consist of TiO₂ nanoparticles are investigated as well. As shown in Figure 5.04 and Table 5.3, the efficiency initially increases with the increment in TiO₂ content until reaches the optimum point, and then reduces at a higher content. The highest photovoltaic parameters with η value of 1.01E-3%, $J_{sc} = 10.77 \mu Acm^{-2}$ and $V_{oc} = 0.43$ V are achieved for devices with 5% TiO₂. The increase of TiO₂ content in the blend film forms more percolation pathways for both electrons and holes, and thereby reduces the R_s that facilitate the charge transport. Subsequently, a large photocurrent and higher η

are yielded. Further increases the TiO_2 content ($>4\%$) has reduced the contribution of P3HT content to the light absorption in visible wavelength regime and destroyed the percolation pathways for hole transports. Thus, it yields a reduced J_{sc} , V_{oc} and η (Wendy U. Huynh, Peng, & Alivisatos, 1999). These PV characteristics display a similar PV trend as that observed for the P3HT:ZnO blend devices.

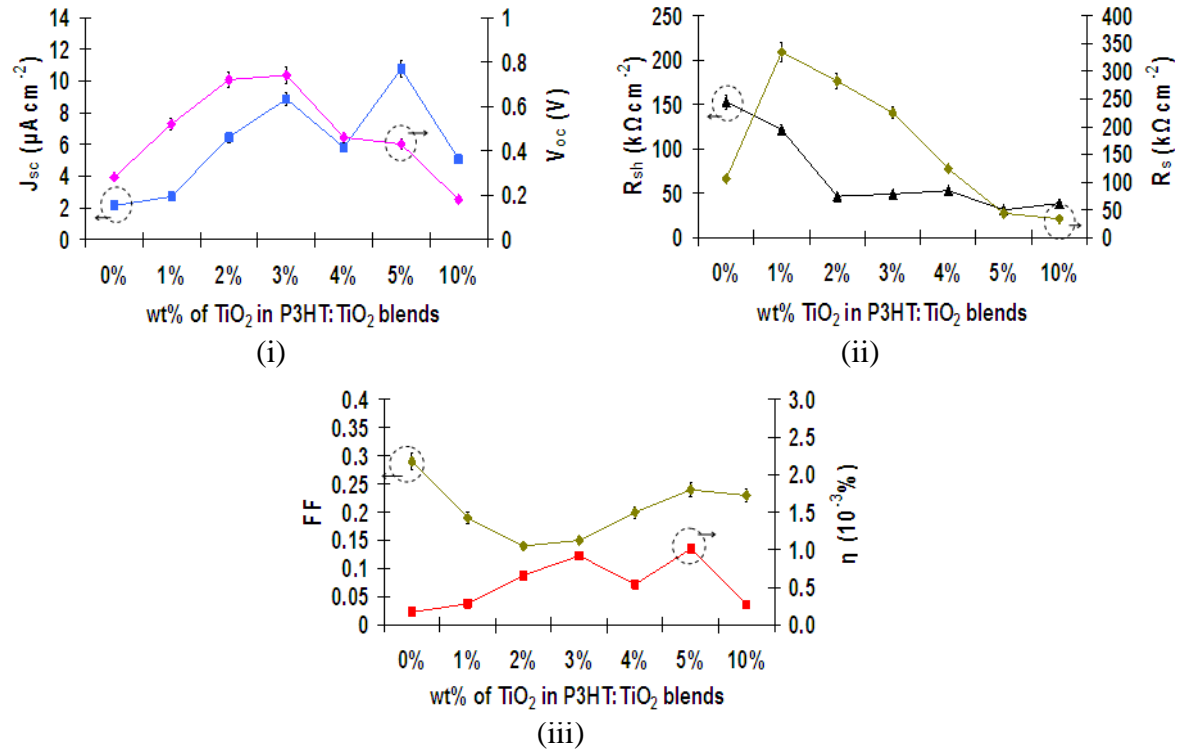


Figure 5.05: Variations in the device parameters for (i) J_{sc} and V_{oc} , (ii) R_s and R_{sh} , (iii) FF and η as a function of blend composition.

The trends observed for the PV effects of the P3HT: TiO_2 devices as a function of TiO_2 concentration in blends (see Figure 5.05) can partially be correlated to the morphological properties of the films that visualized by AFM images. Upon addition of certain amount of TiO_2 , spherical features are formed and appear to be more interconnected. A further increase in TiO_2 content eventually produces rougher films. Solar cells made from such films exhibit poor PV behavior as the absorbance of light has been reduced and the poor quality of surface morphology might most likely contains pinholes leading to shunts. The reduction in J_{sc} , induced by the increase of TiO_2 content

above 5% may result in the growth of larger aggregates, which consequently lead to the formation of unperturbed P3HT domains between the TiO₂ and P3HT components. This may ultimately minimize the effective charge transport and overall device performances.

5.2.2. Results on P3HT:Y₂O₃ Blend Films and Solar Cell Devices.

A. Optical Characterization

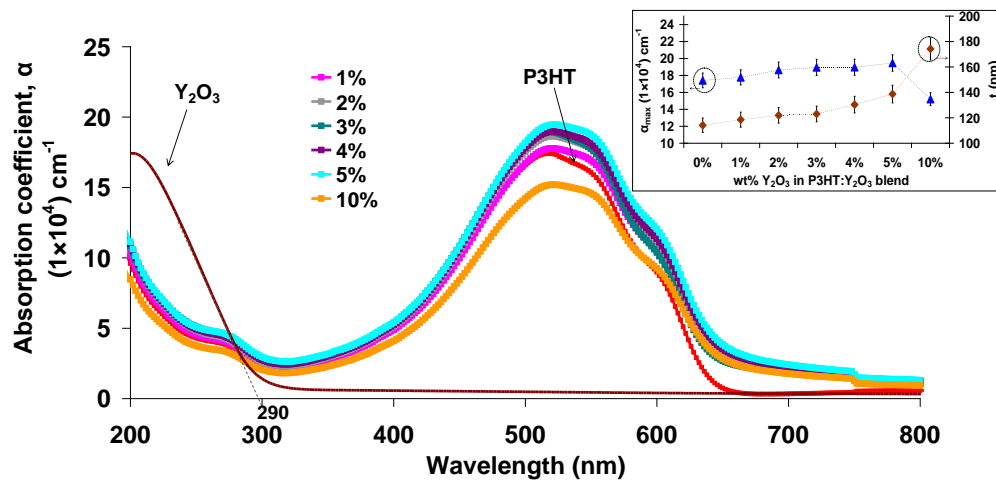


Figure 5.06: The optical spectra for the P3HT:Y₂O₃ blend films. The inset indicates the variation of α_{\max} and film thickness as a function of Y₂O₃ content in P3HT:Y₂O₃ blends.

Table 5.4: Summaries of the α_{\max} values together with the corresponding wavelength positions, λ , film thickness, t and estimated E_g for pristine P3HT and P3HT:Y₂O₃ blends.

Samples	α_{\max} (1×10^4) cm ⁻¹	λ (nm)	t (nm)	E_g (eV) (± 0.01 eV)
Pristine P3HT	17.4	518	114.1	1.97
Pristine Y ₂ O ₃	34.9	232	122.5	4.33
P3HT + 1% Y ₂ O ₃	17.8	520	105.2	1.95
P3HT + 2% Y ₂ O ₃	18.6	520	109.1	1.96
P3HT + 3% Y ₂ O ₃	18.9	518	113.1	1.96
P3HT + 4% Y ₂ O ₃	19.0	520	115.2	1.95
P3HT + 5% Y ₂ O ₃	19.5	522	116.9	1.94
P3HT + 10% Y ₂ O ₃	15.2	522	120.2	1.95

Figure 5.06 shows the absorption spectra of the pristine P3HT, Y_2O_3 and P3HT: Y_2O_3 blend films with different contents of Y_2O_3 . The Y_2O_3 nanoparticles film absorbs light in the UV wavelength range from 190-250 nm while the optical band gap reported for Y_2O_3 is around 5.0–5.8 eV (Cho et al., 1998; Ohta, Yamaoka, & Miyazaki, 2004; Paumier, Gaboriaud, & Kaul, 2002). The effect of blend composition on the optical properties of the blends is in agreement with the aforementioned metal oxide nanoparticles as well, in which an optimal amount of Y_2O_3 is needed to achieve a broader light absorption region.

B. Structural Characterization

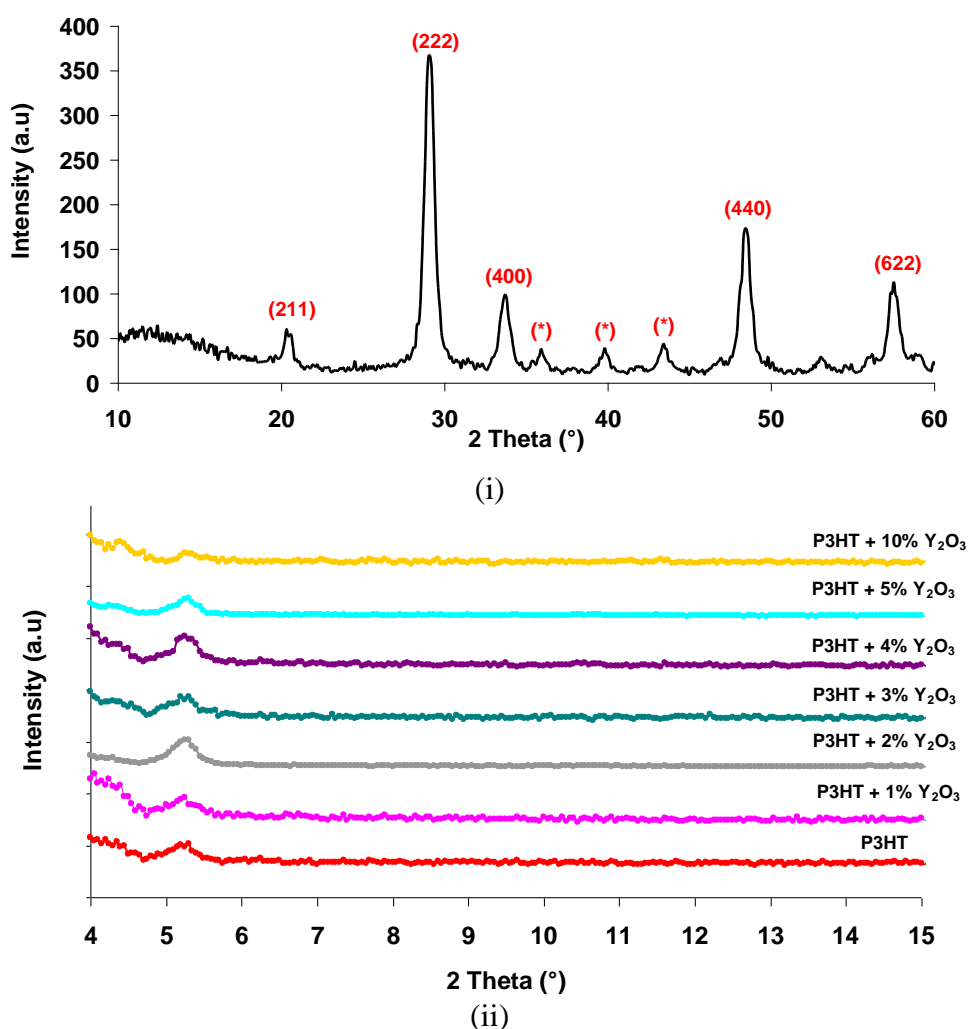


Figure 5.07: The XRD spectra of (i) Y_2O_3 nanopowder; (ii) P3HT: Y_2O_3 blend films.

Table 5.5: Summaries of the Bragg diffraction angles and film roughnesses of pristine P3HT and P3HT:Y₂O₃ blends.

Samples	Bragg diffraction angle, 2 θ ($\pm 0.01^\circ$)	Film roughness (± 0.1 nm)
Pristine P3HT	5.21	1.1
P3HT + 1% Y ₂ O ₃	5.21	3.9
P3HT + 2% Y ₂ O ₃	5.29	4.0
P3HT + 3% Y ₂ O ₃	5.27	5.3
P3HT + 4% Y ₂ O ₃	5.26	6.3
P3HT + 5% Y ₂ O ₃	5.26	9.1
P3HT + 10% Y ₂ O ₃	5.25	14.3

Figure 5.07(i) shows XRD spectrum of Y₂O₃ powder which exhibit strong diffraction peaks at about 20.3°, 29.1°, 33.7°, 48.4° and 57.5°. These peaks are assigned to be due to the (211), (222), (400), (440), (622) planes of Y₂O₃, respectively (Bezuidenhout & Pretorius, 1986; Sipp, Langlais, & Naslain, 1992; Swarnalatha, Stewart, Guenther, & Carniglia, 1992; Tsutsumi, 1970). Other weak diffraction peaks which correspond to unknown planes are labeled (*) in the diffractogram. The semi-crystalline structure of the sample is identified as a cubic crystal structure with space group Ia-3 (No. 206), which is the same as bulk Y₂O₃ (L. Wang et al., 2009). From the obtained XRD result, the particle size of the as-purchased Y₂O₃ powder is confirmed in nanoscale with a crystallite size of about 23 nm. This XRD result suggests that Y₂O₃ powder is composed of polycrystalline as well as a small portion of amorphous phase as indicated by a broader pattern with low diffraction intensity. Figure 5.07(ii) shows the XRD patterns for the P3HT:Y₂O₃ blend films. It can be observed that all the films virtually exhibit almost amorphous phase with only a single small crystalline peak referring to that of P3HT phase. A higher doping of Y₂O₃ into the blends reduces the crystallinity of P3HT, which can be ascribed to the presence of enhanced interaction between Y₂O₃ nanoparticles and P3HT chains.

C. Morphological Characterization

The AFM images of P3HT:Y₂O₃ at different blend compositions are shown in Figure 5.08. The evolution of film morphology is apparent with the Y₂O₃ nanoparticles concentration. The films with higher Y₂O₃ content show much larger agglomerated particles, forming irregular shape of large clusters throughout the film compared to the blends with low Y₂O₃ contents. The film roughness gradually increases from 3.9 nm to 14.3 nm with increasing the Y₂O₃ content. Again, this result is consistent with the previous obtained AFM results for the blends of P3HT:inorganic metal oxide nanoparticles.

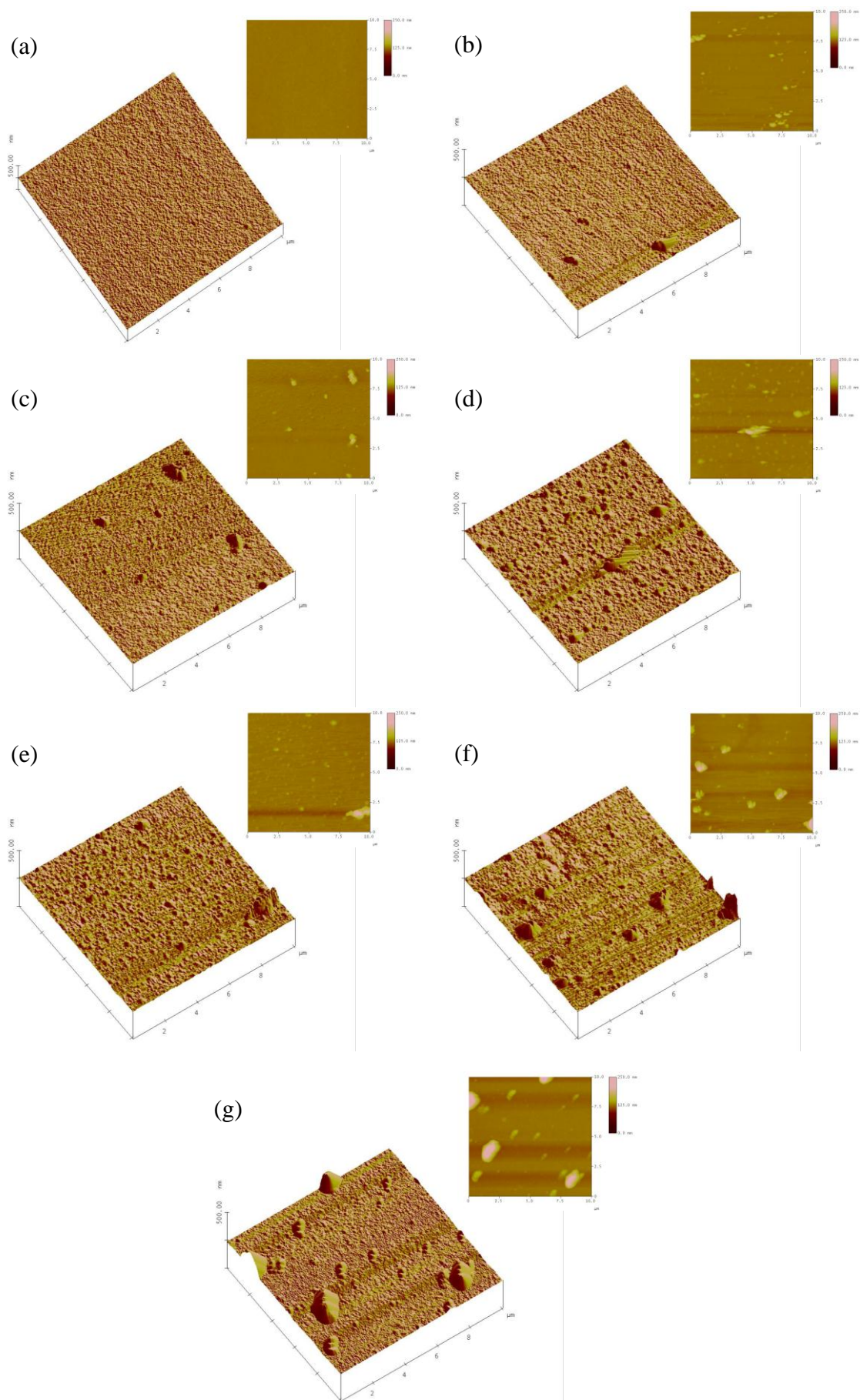


Figure 5.08: The AFM images for (a) pristine P3HT and the blend films with (b) 1%, (c) 2%, (d) 3%, (e) 4%, (f) 5%, and (g) 10% Y_2O_3 .

D. Electrical Characterization

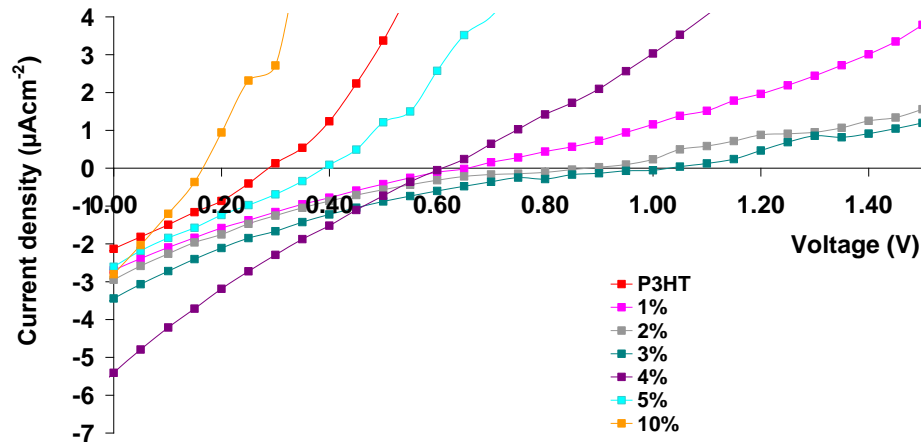


Figure 5.09: The J-V plots for pristine P3HT and P3HT:Y₂O₃ blend devices.

Table 5.6: The comparison of device characteristics parameters for P3HT and P3HT:Y₂O₃ solar cells.

Samples	J_{sc} (μAcm^{-2})	V_{oc} (V)	R_{sh} (± 0.1 $k\Omega cm^{-2}$)	R_s (± 0.1 $k\Omega cm^{-2}$)	FF	η ($10^{-3}\%$)
Pristine P3HT	2.13	0.28	152.9	106.1	0.29	0.17
P3HT + 1 % Y ₂ O ₃	2.70	0.65	150.8	286.4	0.21	0.35
P3HT + 2 % Y ₂ O ₃	2.95	0.92	133.3	779.3	0.15	0.38
P3HT + 3 % Y ₂ O ₃	3.45	1.01	125.8	529.2	0.16	0.50
P3HT + 4 % Y ₂ O ₃	5.41	0.61	81.3	170.5	0.23	0.69
P3HT + 5 % Y ₂ O ₃	2.61	0.38	115.2	116.3	0.25	0.25
P3HT + 10 % Y ₂ O ₃	2.80	0.17	64.4	98.0	0.24	0.12

Figure 5.09 shows the J-V characteristics of P3HT:Y₂O₃ based solar cells under white light illumination. The PV performance of P3HT:Y₂O₃ devices as a function of the Y₂O₃ nanoparticles concentration in the P3HT:Y₂O₃ blends are summarized in Table 5.6. As shown in Figure 5.10 and Table 5.6, it is obvious that the non-monotonic variation in the PV properties of P3HT:Y₂O₃ devices is strongly governed by the blend composition. It can be seen that there is a drastic increase in J_{sc} and V_{oc} with a decreased R_s that leads to an increase in η from 0.17E-3% to 0.69E-3%. The highest values of J_{sc} and η (5.41 μAcm^{-2} and 0.69E-3%, respectively) are obtained at Y₂O₃ concentration

around 4%. This is expected to originate from the optimization of both concentration and Y_2O_3 dispersion through the P3HT matrix. These observed PV trends are consistent with those previously presented for P3HT:ZnO and P3HT:TiO₂ solar cell devices, in which an optimal amount of Y_2O_3 nanoparticles is required to ensure enhanced absorption and good quality of surface morphology. By controlling these properties, favorable phase separation and efficient charge transport can be achieved, which are the initial key parameters for obtaining affordable solar cell performance. Noteworthy, the determination of the optimal blend composition is varying dependent on the types and different forms of n-type inorganic metal oxide materials.

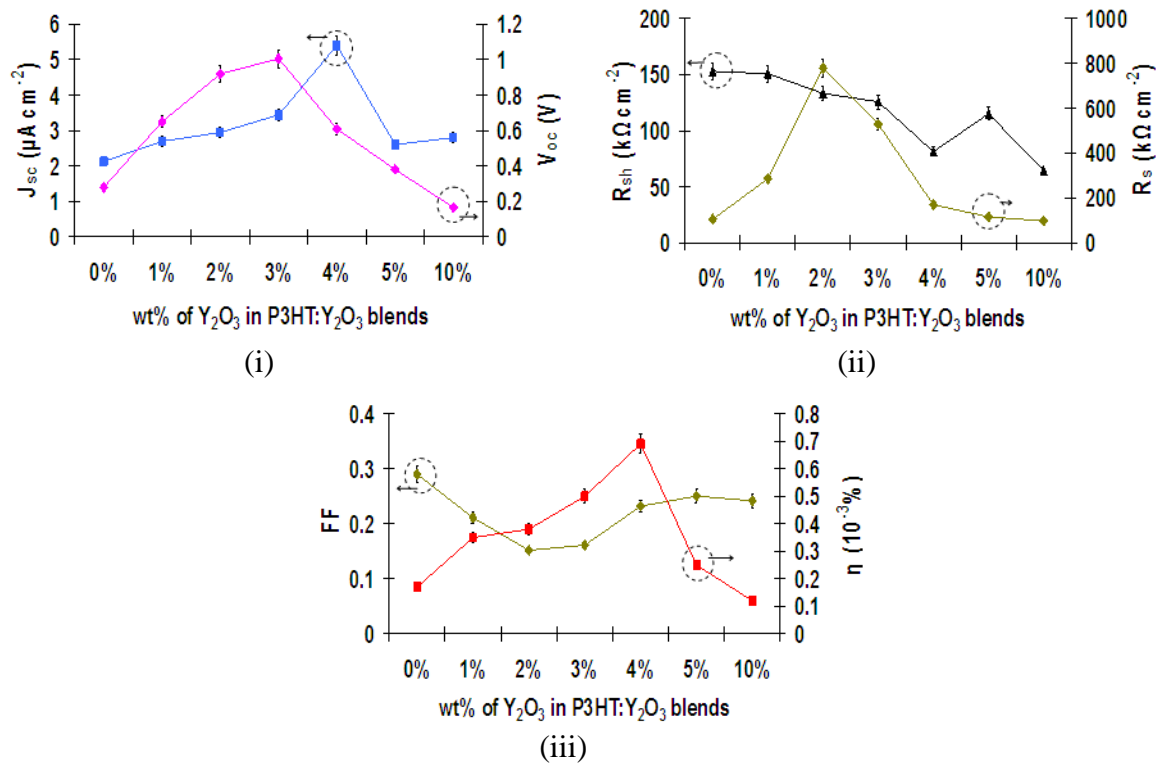


Figure 5.10: Variations in the device parameters for (i) J_{sc} and V_{oc} , (ii) R_s and R_{sh} , (iii) FF and η as a function of blend composition.

5.2.3 Comparison of Hybrid Systems Based on Three Different Types of Inorganic Metal Oxide Nanoparticles

A. Optical Characterization

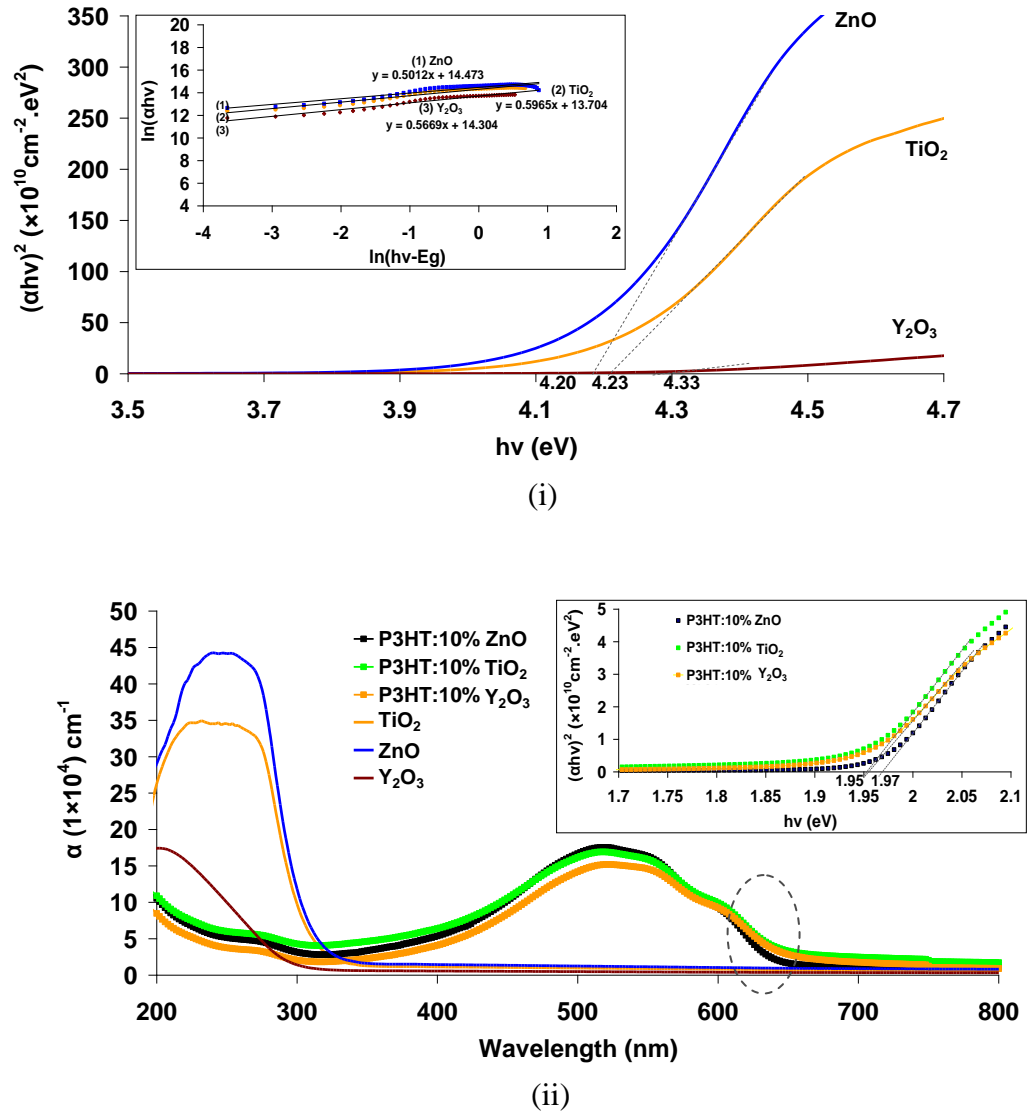


Figure 5.11: (i) Plots of $(\alpha h\nu)^2$ against $h\nu$ for ZnO, TiO_2 and Y_2O_3 films, the inset shows the plots of $\ln(\alpha h\nu)$ versus $\ln(h\nu - E_g)$ to determine the type of electronic transition for the nanoparticles. (ii) Absorption coefficient spectra of the P3HT:nanoparticles blends; the inset shows the estimated E_g of the blends.

To start studying with the optical properties of the three types of as-purchased inorganic metal oxide nanoparticles (ZnO, TiO₂ and Y₂O₃), their optical band gap and types of electronic transitions governing within the materials are determined. These are estimated by means of the optical absorption spectra (Essick & Mather, 1993). Figure 5.11(i) shows that all three metal oxide materials in thin film form exhibit steep absorption edge characteristics of direct band gap semiconductors. Below the edge, extending throughout the visible range, each material becomes mostly transparent. Nevertheless, their estimated E_g values (4.2-4.3 eV) are found to deviate from that of the reported values for their bulk counterparts (~3.0 to ~4.0 eV for ZnO and TiO₂ (Ravirajan et al., 2006; Rodríguez & García, 2007; Srikant & Clarke, 1998); ~5.0 to ~6.0 eV for Y₂O₃ (Cho, et al., 1998; Ohta, et al., 2004; Paumier, et al., 2002)). Such deviation may due to the variation in the stoichiometric of the involved synthesis methods, the purity degree of nanoparticle, crystalline size and the types of electronic transition (Hidalgo, Aguilar, Maicu, Navío, & Colón, 2007; Hossain, Sheppard, Nowotny, & Murch, 2008).

The absorption coefficient spectra of the three different films based on P3HT:inorganic nanoparticle blends is shown in Figure 5.11(ii). It can be observed that the P3HT:ZnO blend film achieves a slightly higher absorption coefficient than those of other blends. This may be attributed to the relatively high photon absorption capability of ZnO nanoparticles as it has been reported that ZnO capable to achieve an absorption coefficient of $(\sim 1.5 \times 10^5) \text{cm}^{-1}$ at a wavelength of 340 nm (Ozgun et al., 2005; Srikant & Clarke, 1998). All these blends virtually exhibit similar E_g values of about ~1.9 eV. Nonetheless, the P3HT:ZnO blend film exhibits a slightly larger E_g of about 0.02 eV than that of the others. It is inferred that this discrepancy may refer to the differences in nanoparticle sizes. In general, a smaller nanoparticle's size yields a broader broad band gap, and consequently results in a blue-shift in the absorption onset (Klaus Sattler,

2002), as indicated by the dashed circle in Figure 5.11(ii). This indicates that ZnO clusters may possess a smaller size than that of others. Since the band gap of P3HT is around 1.9 eV, limiting the solar photon absorption to below a wavelength of about 650 nm. Hence, a smaller band gap is required to be achieved so as to increase the total amount of photons that can be harvested by these organic solar cells. Nevertheless, the narrowing of polymers band gap may probably yield a decrease in device efficiency due to the reduction in V_{oc} . Here, an optimal band gap in the range of 1.9-2.0 eV is found to be favorable for the hybrid devices as these devices substantially rely on the charge separation and transport properties of both the donor and acceptor materials (Kroon, Lenes, Hummelen, Blom, & de Boer, 2008).

B. Structural Characterization

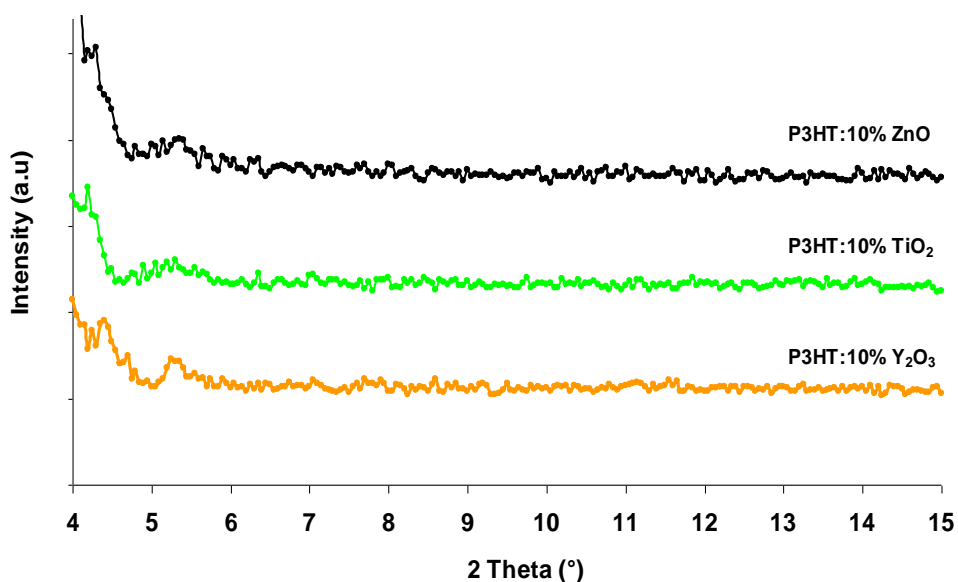


Figure 5.12: The XRD spectra of P3HT:nanoparticles blend films.

Figure 5.12 shows the XRD patterns of the P3HT:inorganic nanoparticles hybrid thin films. The XRD spectra shows that these blend films are virtually transformed from ordered structure of the P3HT chains into the amorphous state, indicating that the dissolution of metal oxide nanoparticles in hybrid have certain effects on the stacking

pattern and structural ordering of P3HT, in which a strong polymer-nanoparticle interaction occurs upon incorporation of the inorganic metal oxides into the P3HT matrix.

C. Morphological Characterization

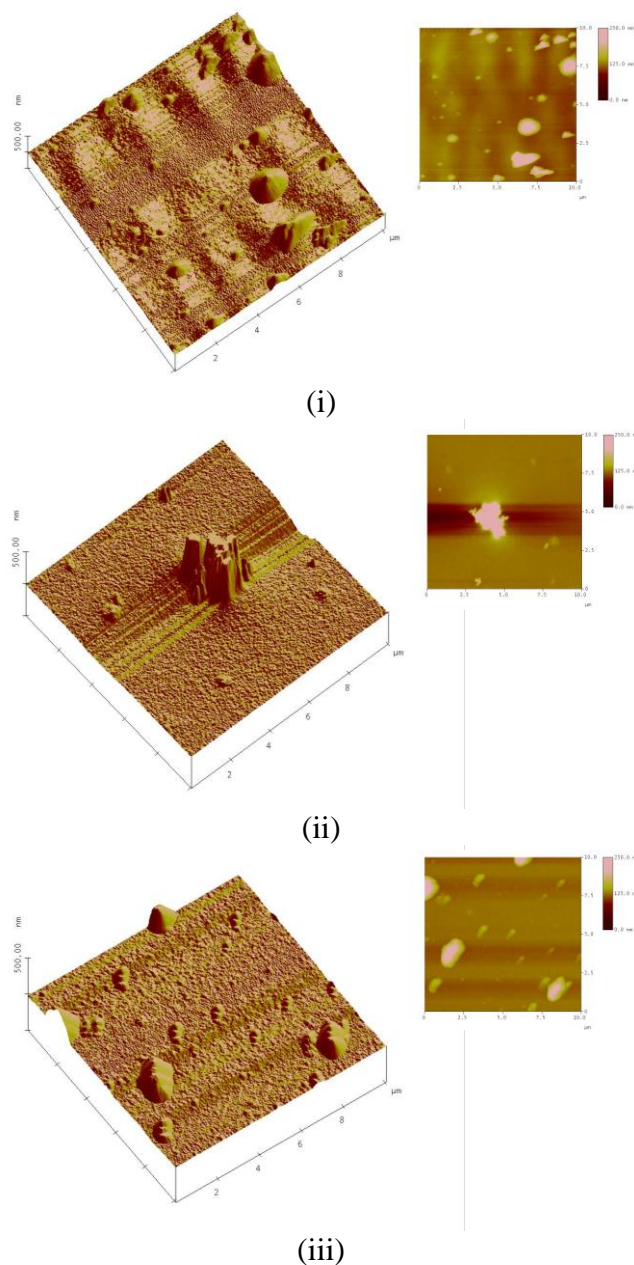


Figure 5.13: The AFM images of P3HT:nanoparticles blend films in 3D and 2D views for (i) P3HT:ZnO, (ii) P3HT:TiO₂, and (iii) P3HT:Y₂O₃ film.

Figure 5.13 shows the AFM images of P3HT:inorganic nanoparticles blend films. A significant difference between the surface morphologies of these P3HT blend films with different types of metal oxide nanoparticles can be observed. All the blends exhibit relatively coarse film surface with a RMS roughness of about 20.5 nm for P3HT:ZnO film, 37.7 nm for P3HT:TiO₂ film, and 14.3 nm for P3HT:Y₂O₃ film. However, it is not sufficient to evaluate the film quality merely by the surface roughness of the film. In fact, a certain level of coarsening is still desired to produce a nanoscale or microscale phase separation, providing bicontinuous pathways for the charges to transport towards their appropriate electrodes (Lei, Yao, Kumar, Yang, & Ozolins, 2008; Ma, Yang, Gong, Lee, & Heeger, 2005; Watkins, Walker, & Verschoor, 2005). It is shown that apparent phase separation are noticeable in P3HT:ZnO hybrid film. In contrast, the AFM images reveal that the surface morphology of P3HT:TiO₂ and P3HT:Y₂O₃ films are rather smoother with less well-detectable phase separation characteristics. Hence, it can be assumed that TiO₂ and Y₂O₃ are fairly well miscible with P3HT. With this degree of miscibility, a low degree of phase separation may be resulted, thereby inducing poor percolation pathway networks within the blends.

For a hybrid system, once the exciton is dissociated, it appears that electron transport has to be reliant on hopping and tunneling mechanism to travel from one domain to other adjacent domain. A certain level of domain agglomeration is desirable in order to facilitate the charge transport and to reduce the frequency of charge interhopping between adjacent domains (Beal et al., 2010). Otherwise, photogenerated charge carriers may not be able to transport efficiently to the respective electrodes and hence the excitons may recombine geminately. Similar predictions have been reported for organic solar cells based on P3HT:phenyl-C71-propionic acid propyl ester ([70]PCPP) and P3HT:(6,6)-phenyl-C71-butyric acid methyl ester ([70]PCBM blends, in which the films exhibit coarser surface morphology to provide optimal phase

separation (Popescu, van 't Hof, Sieval, Jonkman, & Hummelen, 2006; Riedel et al., 2005). As such, the differences in morphology may significantly influence the charge transport behaviors within these blends.

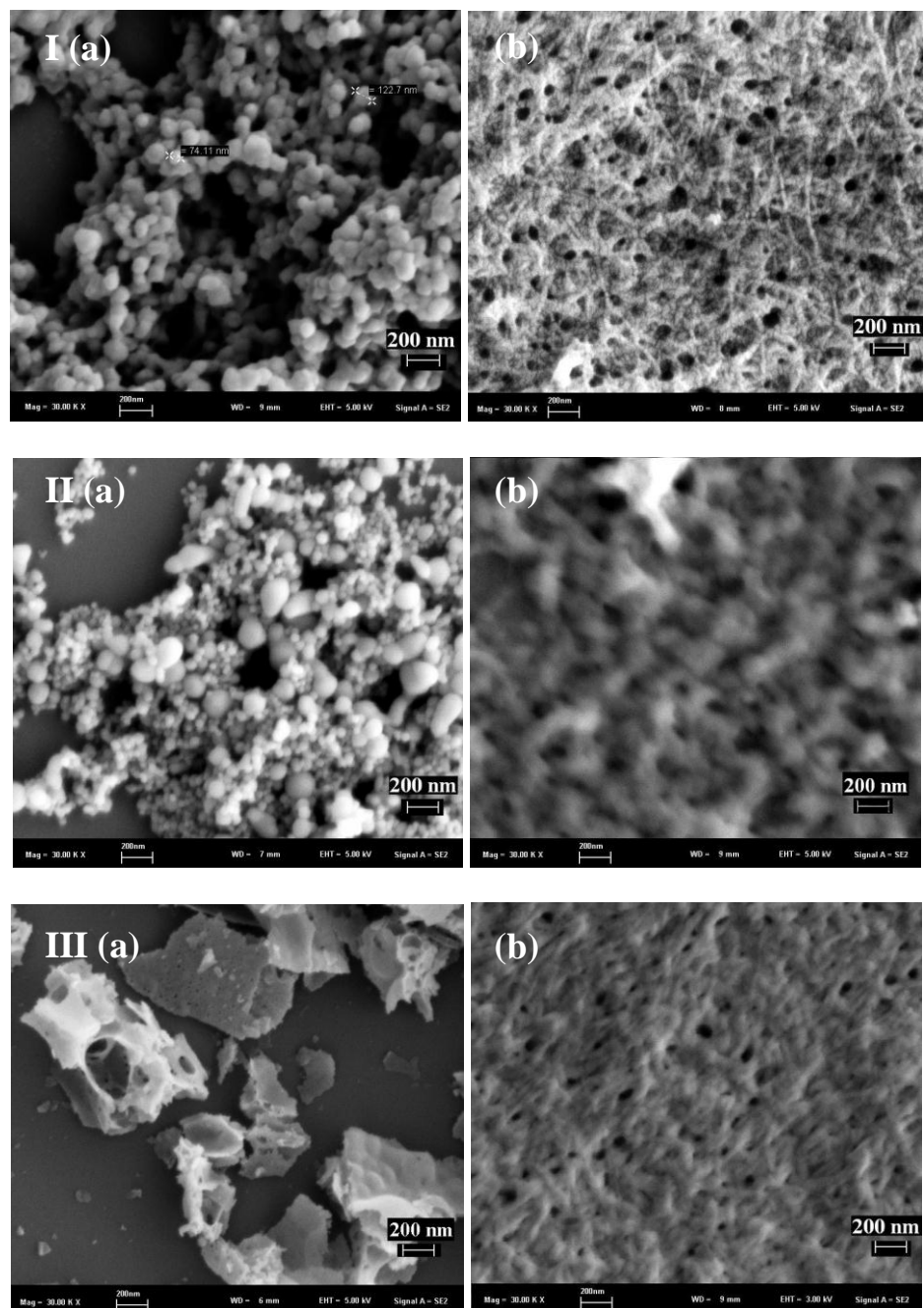


Figure 5.14: FESEM images of the (a) pristine inorganic metal oxide nanoparticles, and (b) P3HT:nanoparticles blend films with ZnO (I), TiO₂ (II) and Y₂O₃ (III).

Figure 5.14(a) shows the FESEM images of the surface morphology of pristine ZnO, TiO₂ and Y₂O₃ films while those for the blend films are shown in Figure 5.14(b). Interestingly, all the pristine films consist of random distribution of agglomerated nanoparticles which are composed of many primary finer particles. The sizes of these particles are found to be varied between 20–40 nm for different types of metal oxides. It has been noticed that nanoparticles geometry has significant effect on the device performance. As reported by Wendy and co-researchers, the photocurrent generation is correlated to the aspect ratio A_R of the nanoparticles (W. U. Huynh, Dittmer, & Alivisatos, 2002). Both the ZnO and TiO₂ nanoparticles possess nearly spherical shape with average primary size <50 nm. Such smaller particle size exhibits larger specific surface area, indicating a higher aspect ratio. On the other hand, it is well noticeable that the Y₂O₃ nanoparticles are most likely to form larger, rectangular-like shapes that may induce a smaller specific surface area than that of the formers. Moreover, it is observed that the ZnO film exhibits more homogenous and uniform agglomeration of ZnO nanoparticles within the film than that of TiO₂ film. This indicates that the ZnO is fairly soluble in organic solvent and tend to disperse more homogeneously in chloroform solution. By taking into account the average geometry size, shape and particles distribution of these types of materials, it can be inferred that the ZnO nanoparticles possess better dispersion stability than that of TiO₂ and Y₂O₃ nanoparticles.

It is worthy to mention that in the case of P3HT blend films, the FESEM morphology images confirm that a net-like structure is favorably formed in the P3HT:TiO₂ and P3HT:Y₂O₃ blend films. Contrary to this, the P3HT:ZnO blend film is likely exhibits a finer fiber-like structure with well-dispersed nanoparticles aggregation over the polymer matrix. By comparing the images of Figure 5.14 (I(b)) and Figure 5.14 (II(b)), it can be observed that the average fiber diameter increases. Similar trend is noticeable for P3HT:Y₂O₃ film (see Figure 5.14 (III(b))). These FESEM results suggest

that the net-like structure of the P3HT:TiO₂ and P3HT:Y₂O₃ samples consist of extensively large acceptor domains, which may virtually limit the carrier mobility and impede effective hole transport to anode from donor P3HT domains. In contrast, P3HT:ZnO shows well-defined acceptor domains and exhibits a larger extent of continuous, unperturbed P3HT domains to facilitate better hole transport network.

D. Electrical Characterization

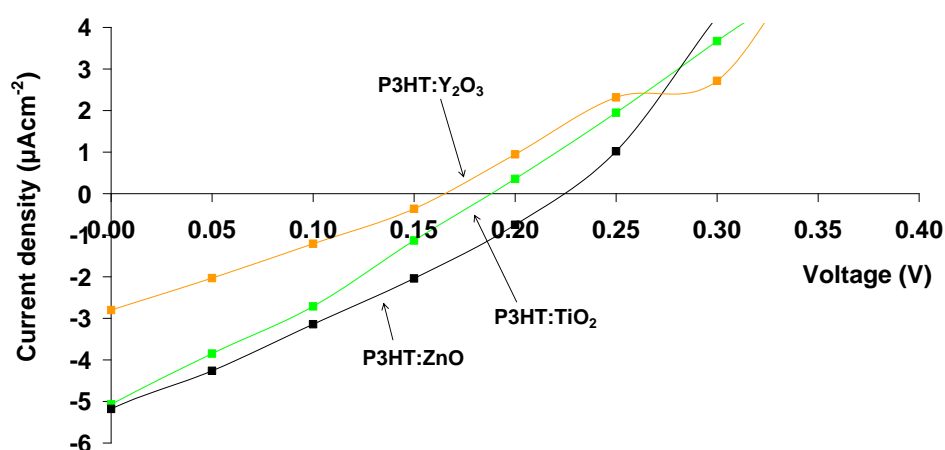


Figure 5.15: Comparison of the J-V characteristics of the solar cells based on three different types of P3HT:metal oxide nanoparticles hybrid systems under white light illumination.

Table 5.7: Variation in the J-V characteristics of P3HT:metal oxide nanoparticles hybrid solar cells.

Devices	J_{sc} (μAcm^{-2})	V_{oc} (V)	R_{sh} (± 0.1 $k\Omega cm^{-2}$)	R_s (± 0.1 $k\Omega cm^{-2}$)	FF	η ($10^{-3}\%$)
P3HT:ZnO	5.18	0.22	43.5	28.3	0.26	0.31
P3HT:TiO ₂	5.07	0.18	38.6	33.7	0.23	0.27
P3HT:Y ₂ O ₃	2.80	0.17	64.4	98.0	0.24	0.12

Figure 5.15 shows the J-V characteristic curves of hybrid solar cells measured under white light illumination power of 100 mWcm^{-2} . The device parameters are summarized in Table 5.7. It is noticed that device based on P3HT:ZnO hybrid system shows the best performance compared to the other systems. In comparison to the P3HT:TiO₂ device, the P3HT:ZnO device shows a slight enhancement in the power conversion efficiency, accompanied by an increase in the V_{oc} of about 22 % and a slightly increased J_{sc} . In contrast, the solar cell device based on P3HT:Y₂O₃ hybrid system is found to be the poorest device, demonstrating the lowest η due to the relatively low photogenerated J_{sc} and V_{oc} . The increased J_{sc} in the P3HT:ZnO device can be ascribed to the improved charge carrier mobility that facilitates efficient charge transport, thereby enhancing FF and reducing R_s for the devices. It is well-known that the generated photocurrent strongly depends on the charge carrier mobility. Bulk ZnO is reported to possess electron mobility of about $4.0 \text{ cm}^2\text{V}^{-1}\text{s}^{-1}$ at room temperature (Bhargava, 1997), which is much higher than that of TiO₂ ($\sim 1 \text{ cm}^2\text{V}^{-1}\text{s}^{-1}$) (Hendry, Wang, Shan, Heinz, & Bonn, 2004) and that of Y₂O₃ (less than $1 \text{ cm}^2\text{V}^{-1}\text{s}^{-1}$) (Klabunde, 2001). Additionally, this enhancement of device efficiency can be attributed to the better nanoparticles dispersion that induces larger effective surface area between the donor and acceptor domains for better exciton dissociation (Ltaief et al., 2005).

Besides, it is noteworthy that these three types of devices exhibit substantially different V_{oc} . The reason for this variation in V_{oc} is hard to be clearly understood. However, one of the plausible reasons may be attributed to the energy level alignment between the donor and acceptor that results in various recombination rates at the hybrid P3HT:metal oxide nanoparticles interfaces. This can be more understood based on the surface morphology of the films and an inferred energy band diagram of the hybrid devices, as illustrated in Figure 5.16. The back-charge recombination may easily take place in which the holes from P3HT recombine again with the electron from

nanoparticles at the D/A interface, owing to the slow transport of the charge carriers to reach their respective electrodes. This type of recombination is strongly affected by the dopant concentration in the blends. Consequently, the distribution and mixing of P3HT and inorganic nanoparticles phases within the film have to be taken into account and need to be well optimized (Beal, et al., 2010).

As shown in Figure 5.16, both ZnO and TiO₂ exhibit considerably small energy offset at the conduction band edges. A smaller energy offset yields a lower energy loss during the charge transfer at the D/A interface. This can be manifested by a higher V_{oc} since the V_{oc} is ultimately dependent on the difference between the HOMO of the donor and LUMO of the acceptor. This means that the photogenerated excitons in both P3HT and inorganic nanoparticles can more easily be dissociated and able to reach the respective electrodes through more energetically favorable channels. This is owing to a lower value of energy offset between the donor and acceptor's LUMO. In contrast, the poor performance of the P3HT:Y₂O₃ based device may be due to the mismatch of the energy level position between P3HT and Y₂O₃, in which the energy offset between P3HT and Y₂O₃'s LUMO is much more larger in comparison to that of the other two systems (Chiam et al., 2008; Ohta, et al., 2004). Hence, it results in more unfavorable exciton dissociation.

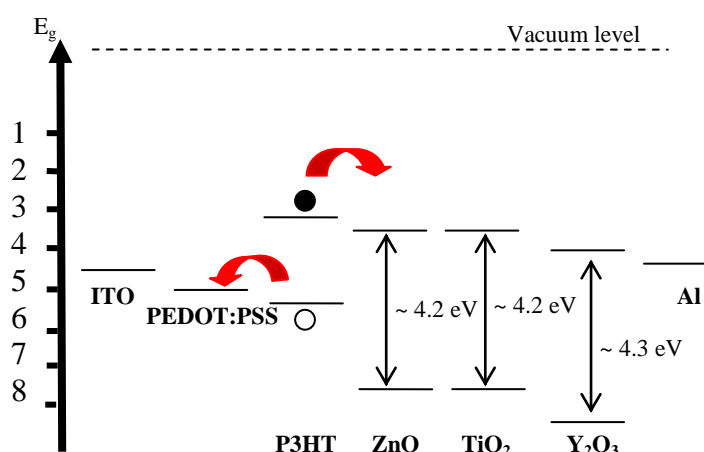


Figure 5.16: An inferred schematic energy band diagram for the P3HT:inorganic nanoparticle hybrid systems, placed between anode ITO and cathode Al.

Nonetheless, the overall device efficiency is still unsatisfied due to the considerably low J_{sc} . The low efficiency in these devices is more likely due to poor charge transport within the blends as the recombination rate might be increased at the domain boundaries between the donor P3HT and metal oxide acceptors, thereby hindering the charges to transport towards the appropriate electrodes (Snaith, Arias, Morteani, Silva, & Friend, 2002). As such, a strongly morphology-dependent charge transport in hybrid solar cells can always be the matters of debate (Shaheen et al., 2001). Typically, microscale phase separation may easily be formed due to the inherent incompatibility and less miscibility between the tendentiously hydrophilic surfaces of ZnO nanoparticles with the hydrophobic P3HT. Consequently, this results in a reduced D/A interfacial area and hence limits the exciton dissociation efficiency (Chen, Xu, Hong, & Yang, 2010). Hence, it is imperative to modify the surface of ZnO nanoparticles to obtain a more homogenous hybrid system with P3HT by applying sol-gel synthesis route, which will be discussed later in detail in Part II.

5.3 Part II: The Improvement of P3HT:ZnO Devices by Sol-gel Synthesis Route

As mentioned before, sol-gel technique is particularly attractive among all of the ZnO thin film preparation techniques due to its good homogeneity, cost effective, ease of fabrication of large area films with excellent compositional control (Sengupta, Sahoo, Bardhan, & Mukherjee, 2011). However, there are still many principal factors affecting the properties of the sol-gel derived films, including sol concentration (Dutta, Mridha, & Basak, 2008), annealing treatment (Y. C. Liu, Tung, & Hsieh, 2006), and film thickness (Sharma & Mehra, 2008). Here, in this study, three different approaches have been employed and their feasibilities in improving the device performances are investigated.

5.3.1 First Approach: Effects of Different Sol Content

For the first approach, the quantity of as-synthesized sol within the P3HT solution is altered in order to estimate the required optimal sol content. Its effects on the physical properties as well as photovoltaic performance of the fabricated solar cell devices are explored.

A. Optical Characterization

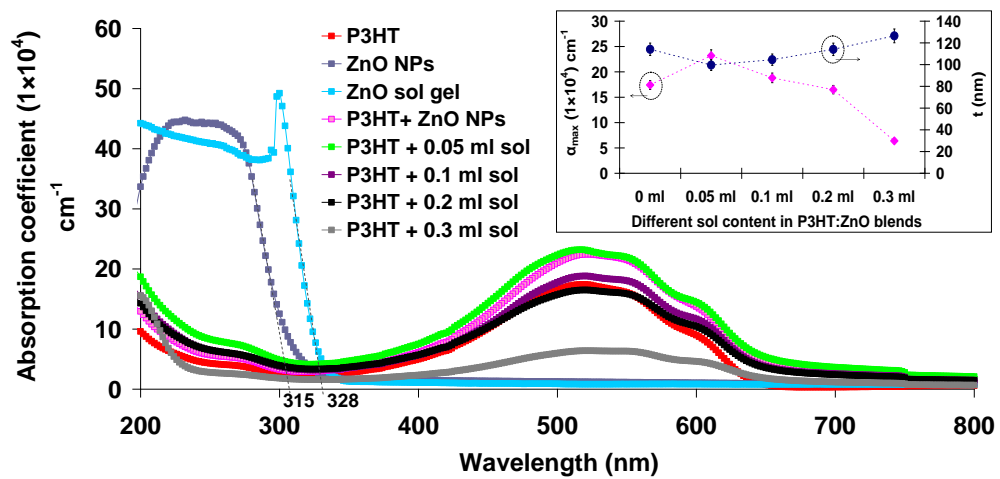


Figure 5.17: Absorption coefficient spectra of pristine P3HT, sol-gel derived ZnO and P3HT:sol gel ZnO blend films with different sol contents. The inset indicates the variation of α_{max} and film thickness as a function of sol content. Also, the comparison between P3HT:ZnO NPs and P3HT:sol-gel ZnO films is shown.

Figure 5.17 shows the absorption coefficient spectra of derived sol-gel ZnO and P3HT:sol-gel ZnO blend films with different sol contents in the form of mixed solutions. The comparison in optical properties between the sol-gel ZnO and as-purchased ZnO nanoparticles (ZnO NPs) film is shown as well. The optical properties, together with the thickness of the films are listed in Table 5.8. The absorption spectra indicate that the sol-gel derived ZnO film possesses high UV absorption properties at wavelength below 400 nm. A sharp absorption edge at approximately 328 nm is observed which corresponds to the direct transition of electrons between the valence

band and conduction band (Mamat, Khusaimi, Musa, Sahdan, & Rusop, 2010). The absorption pattern of the sol-gel ZnO film is found to be different to that of the ZnO nanoparticle film, which is most likely due to the variation in synthesis processing means. However, the presence of this peak on the absorption spectra reveals a better structural quality of the ZnO film derived from sol-gel precursor (Peulon & Lincot, 1996).

From Figure 5.17, it can be observed that the absorbance of the films in the visible range drastically reduces with the increase of sol content from 0.05 ml to 0.3 ml. This property can be elucidated by two major factors that may affect the optical properties of the films, which are surface scattering and grain-boundary scattering (Li, Xu, Li, Shen, & Wang, 2010). A rough surface and irregular grain-boundary of film may induce stronger surface scattering and grain-boundary scattering. This evidence can be more understandable upon taking AFM images which will be discussed later. The inset of Figure 5.17 shows that the film thickness increases almost linearly from 114.1 nm to 126.5 nm with increasing sol content.

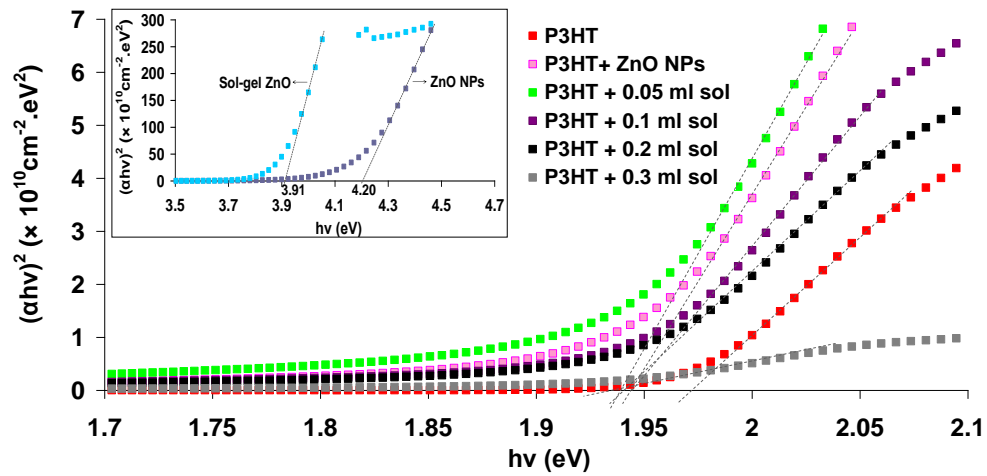


Figure 5.18: The plots of $(\alpha h\nu)^2$ against $h\nu$ for P3HT:sol gel ZnO blend films with different sol contents.

Figure 5.18 shows the plots of $(\alpha h\nu)^2$ vs $h\nu$ for the blend films with various sol contents. A slightly decrease in E_g from 1.97 eV to 1.93 eV with sol content varies from 0 ml to 0.3 ml is noticed for the blend films. The narrowing band gap energy is most probably due to the increasing carrier concentration with Zn^{2+} doping (Bae, Choi, Na, & Park, 2005; Caglar, Ilican, & Caglar, 2009) that alters the width of the localized states within the optical band. The E_g of the bare sol-gel ZnO film can be determined by extrapolation of the plot of $(\alpha h\nu)^2$ versus $h\nu$ (see the inset of Figure 5.18) and is found to be about 3.91 eV. Although this estimated E_g is found to be different from the reported values for ZnO crystal (3.3 eV) (J.-H. Lee, Ko, & Park, 2003; J. Lee, Eastal, Pal, & Bhattacharyya, 2009) which might be due to the grain boundaries and imperfection of the polycrystalline films (Bao, Gu, & Kuang, 1998), this deviation is found to be smaller than that of the as-purchased ZnO NPs film.

Table 5.8: The comparison of α_{max} values, the corresponding wavelength positions, average film thicknesses and estimated E_g for P3HT:sol gel ZnO blends with different sol contents.

Samples	Maximum absorption coefficient peak, α_{max} (1×10^4) cm^{-1}	Wavelength position, λ (nm)	Average film thickness, t (nm)	E_g (± 0.01 eV)
Pristine P3HT	17.4	518	114.1	1.97
ZnO NPs	44.8	232	164.4	4.20
ZnO sol gel	49.2	300	119.5	3.91
P3HT + ZnO NPs	22.4	522	130.7	1.95
P3HT + 0.05 ml sol	22.4	516	99.6	1.94
P3HT + 0.1 ml sol	18.8	520	104.5	1.94
P3HT + 0.2 ml sol	16.5	520	114.8	1.94
P3HT + 0.3 ml sol	6.4	522	126.5	1.93

B. Structural Characterization

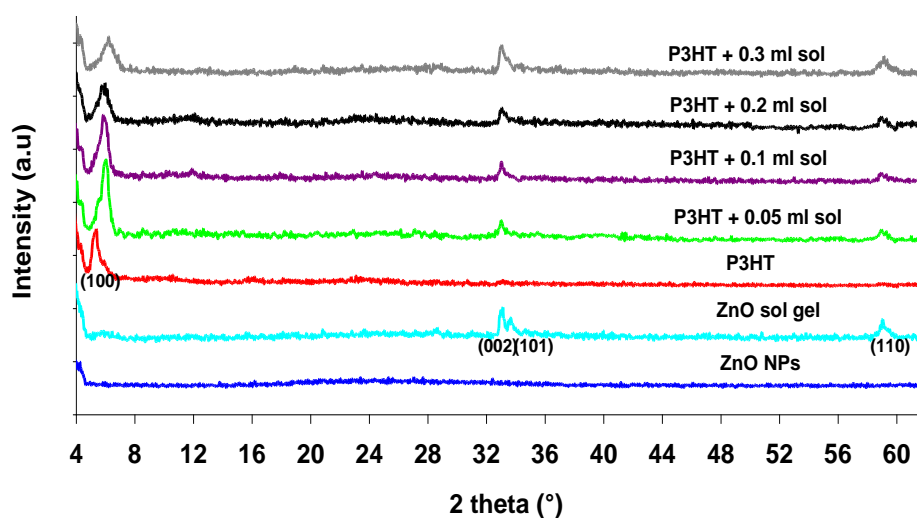


Figure 5.19: The XRD patterns of P3HT:sol-gel ZnO blend films with different sol contents as well as XRD patterns of bare ZnO NPs deposited film and sol-gel derived ZnO films.

Table 5.9 (i) & (ii): Summaries of the XRD parameters of P3HT:sol gel ZnO blend films with different sol contents.

(i)

Samples	Bragg diffraction angle, 2θ at different planes ($\pm 0.01^\circ$)				d-spacing at (100) plane (± 0.01 nm)
	(100)	(002)	(101)	(110)	
Pristine P3HT	5.28	-	-	-	1.67
ZnO sol gel	-	33.06	33.64	59.08	-
P3HT + 0.05 ml sol	5.95	33.03	-	59.02	1.48
P3HT + 0.1 ml sol	5.87	33.06	-	59.00	1.50
P3HT + 0.2 ml sol	5.85	33.09	-	59.00	1.51
P3HT + 0.3 ml sol	6.18	33.07	-	59.13	1.43

(ii)

Samples	FWHM, B ($\pm 0.10^\circ$)				Crystallite size, t (± 0.1 nm)				Dislocation density, δ (1×10^{-3}) nm $^{-2}$			
	(100)	(002)	(101)	(110)	(100)	(002)	(101)	(110)	(100)	(002)	(101)	(110)
Pristine P3HT	0.42	-	-	-	21.0	-	-	-	2.30	-	-	-
ZnO sol gel	-	0.42	0.95	0.57	-	22.0	9.7	17.9	-	2.07	1.06	3.14
P3HT + 0.05 ml sol	0.67	0.97	-	0.71	13.2	9.5	-	14.3	5.74	1.11	-	2.36
P3HT + 0.1 ml sol	0.61	0.43	-	0.43	14.6	21.2	-	23.6	4.70	2.23	-	1.80
P3HT + 0.2 ml sol	0.50	0.40	-	0.54	12.5	23.2	-	18.8	6.37	1.86	-	2.82
P3HT + 0.3 ml sol	1.09	0.39	-	0.86	8.1	23.7	-	11.9	1.53	1.78	-	7.11

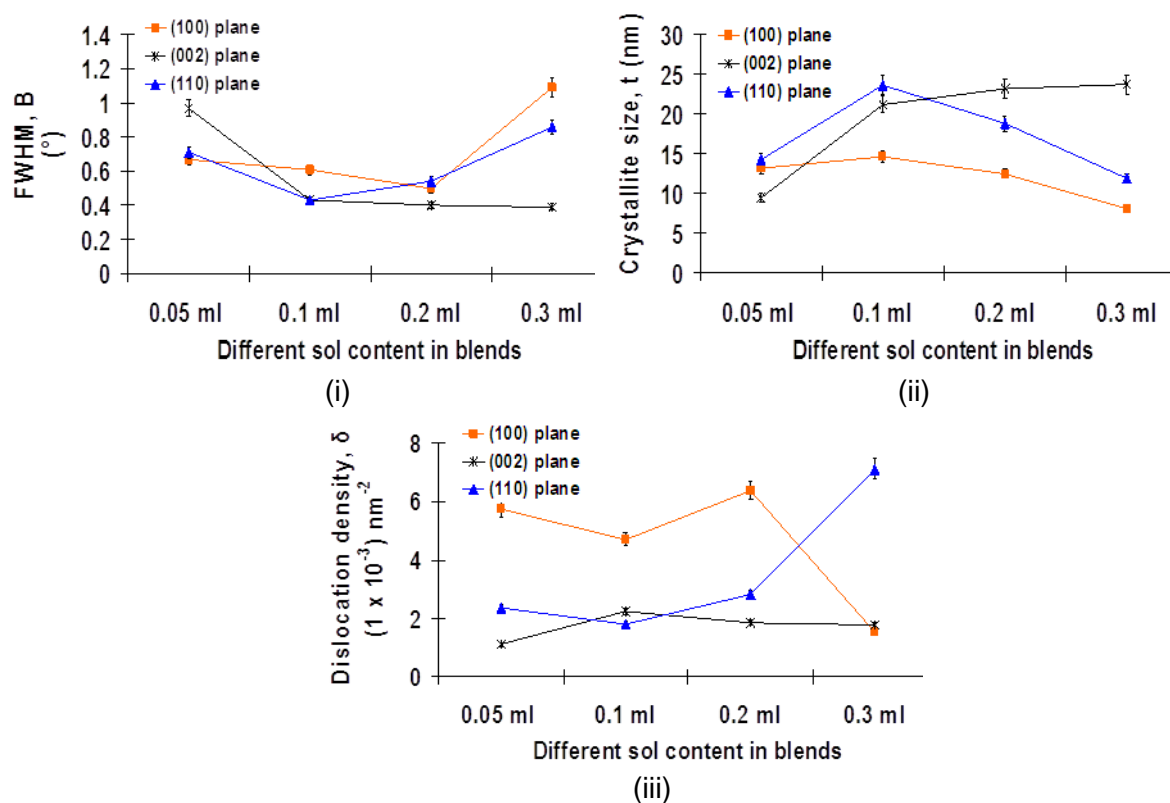


Figure 5.20: XRD parameters of blend films as a function of different sol contents, namely: (i) FWHM, (ii) crystallite size and (iii) dislocation density corresponding to (100), (002), and (110) planes.

Figure 5.19 shows the XRD pattern of P3HT:sol-gel ZnO blend films with different sol contents. It is noticeable that the derived sol-gel ZnO film exhibits three peaks at 2θ angle of 33.06° , 33.64° and 59.08° which correspond to the diffraction from (002), (101) and (110) planes, respectively. All the peaks indicate the polycrystalline nature of the ZnO with hexagonal wurtzite structure (Gupta et al., 2009). This XRD pattern is found to be different from that of the P3HT blend film prepared from as-purchased ZnO nanoparticles, whereby no crystallite peak can be detected and the film is mostly amorphous. Upon the addition of different sol contents into P3HT, it is found that the blend films exhibit several diffraction peaks. These peaks are indexed to the (100) plane owing to the existence of P3HT crystallites, while peaks at (002) and (101) planes are corresponding to the polycrystalline phase of ZnO. There are no other peaks can be detected in the spectra.

In several research findings, c-axis preferentially oriented growth of wurtzite ZnO grains has been observed (Musat, Rego, Monteiro, & Fortunato, 2008; Ohyama, Kozuka, & Yoko, 1998). However, in the present results, the relative peak intensities shown in XRD spectra suggest that there is no preferred grain orientation in the films. The random distribution of ZnO grains suggests a random nucleation and growth kinetics mechanism in which such a grain growth is categorized as isotropic types (Oral, Menşur, Aslan, & Başaran, 2004; Xue et al., 2008). This may be most likely due to the difference in the sol precursor chemistry and annealing treatment temperature (Fujihara, Sasaki, & Kimura, 2001). This suggests that the crystallographic orientation of sol-gel derived ZnO film can be significantly affected by the processing conditions. It is noticeable that the crystalline character of the films at (002) and (110) peaks which correspond to the ZnO crystalline phase is increased with the increase in sol content from 0.05 ml to 0.3 ml, as indicated by enhanced peak intensities. This suggesting that the increased amount of sol into the blend may cause further condensation and aggregation of zinc moieties in the blend solution, thereby substantially improve the growth of ZnO along (002) and (110) planes (Fathollahi & Amini, 2001). However, the random orientation of grains is ultimately acted upon increasing the film thickness and the composite material becomes less dense (Torres Delgado, Zúñiga Romero, Mayén Hernández, Castanedo Pérez, & Zelaya Angel, 2009).

The average crystallite size of P3HT and ZnO grains is estimated from the XRD spectra by using Scherrer's formula and the results are summarized in Table 5.9(ii). For the sol-gel derived ZnO film, the crystallite size is found to be in the range between 9 to 23 nm. It is observed that the crystallite sizes of both ZnO and P3HT grains are sensitive to the sol content. Based on the plot (ii) in Figure 5.20, it is noticed that the crystallite size of P3HT (refer to (100) peak) decreases, but the crystallite size of ZnO remains to increase with the increasing sol content (refer to (002) peak). These are

consistent with the decreasing trend of FWHM (peak width) values in the XRD spectra, indicating a higher coalescence of small ZnO crystallites along (002) plane. Hence, the free surface energy and interfacial energy between the substrate and film is minimized (Sharma & Mehra, 2008). The crystallite size and the variation of dislocation density of the films as a function of sol content are also presented in Figure 5.20(iii). The dislocation density, δ of the films is used to identify the amount of defects present in the films owing to the imperfection of a crystal. This is estimated using Williamson and Smallman's relation (Caglar, et al., 2009):

$$\delta = \frac{n}{t_c^2} \quad (5.1)$$

where n is a factor, which equals to unity providing minimum δ and t_c is the estimated crystallite size. The increase in δ with increasing sol contents indicating a higher degree of lattice imperfections. As the crystallite size of the ZnO increases with increasing sol content, the δ exhibits an increasing trend too, indicating an increased concentration of the lattice imperfections for blends with higher sol content. This suggests that the optimal sol content required for the blends of P3HT to show enhanced film crystallinity with small amount of lattice imperfections is less than 0.2 ml.

C. Morphological Characterization

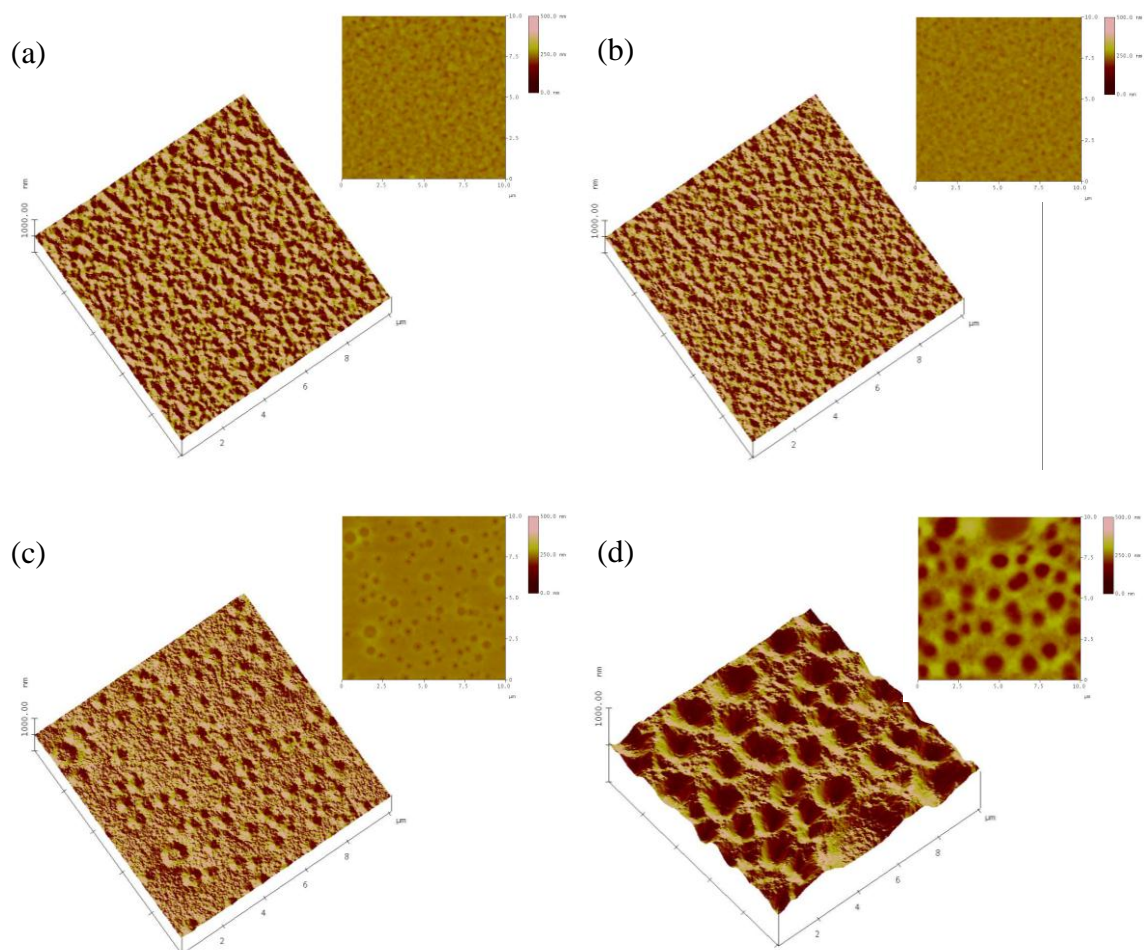


Figure 5.21: The AFM images of P3HT:sol-gel ZnO blend films with (a) 0.05 ml, (b) 0.1 ml, (c) 0.2 ml, and (d) 0.3 ml sol content.

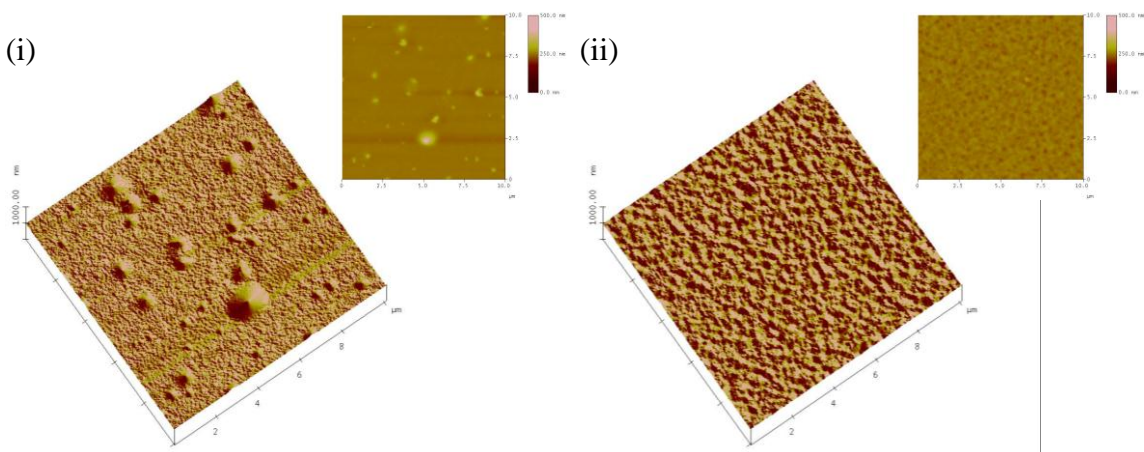


Figure 5.22: AFM images by $10 \times 10 \mu\text{m}^2$ scan in both 2D and 3D views of (i) P3HT:ZnO NPs and (ii) P3HT:sol gel ZnO blend films.

Table 5.10: Surface roughness values of the blend films obtained from AFM.

Samples	Root-mean-square roughness, RMS (± 0.1) nm
Pristine P3HT	1.1
P3HT + ZnO NPs	9.5
P3HT + 0.05 ml sol	8.3
P3HT + 0.1 ml sol	6.8
P3HT + 0.2 ml sol	10.4
P3HT + 0.3 ml sol	30.5

Figure 5.21 shows the two dimensional (left) and three dimensional (right) surface morphology images of the P3HT:sol-gel ZnO films. The RMS roughness values for all the films are presented in Table 5.10. Apparently, the blend film morphology evolves drastically with the variation in sol content in blends. It can be seen from Figure 5.21 that upon the addition of a small quantity of sol into the blends, the films show relatively even surface which is necessary to diminish inelastic scattering processes at the film surface. However, the surface morphology of the films become uneven and coarser, changing from hillock-like feature to highly porous feature when the content of sol is increased from 0.05 ml to 0.3 ml. Comparatively, the films roughnesses varied in this manner are 8.3, 6.8, 10.4 and 30.5 nm, respectively. This morphology change is presumably because of increased viscosity of the resultant blend solutions which may result in an increased amount of solutes that provoke the growth of Zn^{2+} nuclei. In order to minimize the free surface energy and interface energy between the blend film and substrate (Sharma & Mehra, 2008), they favorably coalesce with each other to form larger grains. It is speculated that the porous structure formation may be assigned to a faster rate of phase separation between P3HT and the zinc moieties adsorbed by mixture solvent than that of the polycondensation of hydrolyzed zinc acetate (Z. Liu, Jin, Li, & Qiu, 2005). Otherwise, it may be generated during the out-gassing of the mixture solvent upon heating (Roberson et al., 2004).

From the 2D morphology images, it can be seen that as the sol content increases to above 0.1 ml, the grains in plane become mostly unclear together with the formation of larger size of pores in the film, which varies from nanometer to micrometer range. Since the as-synthesized sol may not thoroughly stable enough, the sizes and dispersion of the ZnO colloidal particles in the sol need to be well optimized. Otherwise, the highly porous structure of the film that consists of higher sol content may expose to higher probability of interface scattering that is compatible with the decreased optical absorption of the films.

Figure 5.22 shows the surface morphology of the optimized P3HT:ZnO nanoparticles blend film and P3HT:sol-gel derived ZnO film (consists of 0.1 ml sol) . In comparison to the P3HT:sol-gel ZnO film morphology, the P3HT:ZnO nanoparticles film virtually exhibits slightly inhomogeneous and rougher film surface with the formation of major aggregations of particles throughout the film. However, the P3HT:sol-gel ZnO film exhibits an improved surface flatness due to the reduced extent of ZnO aggregation.

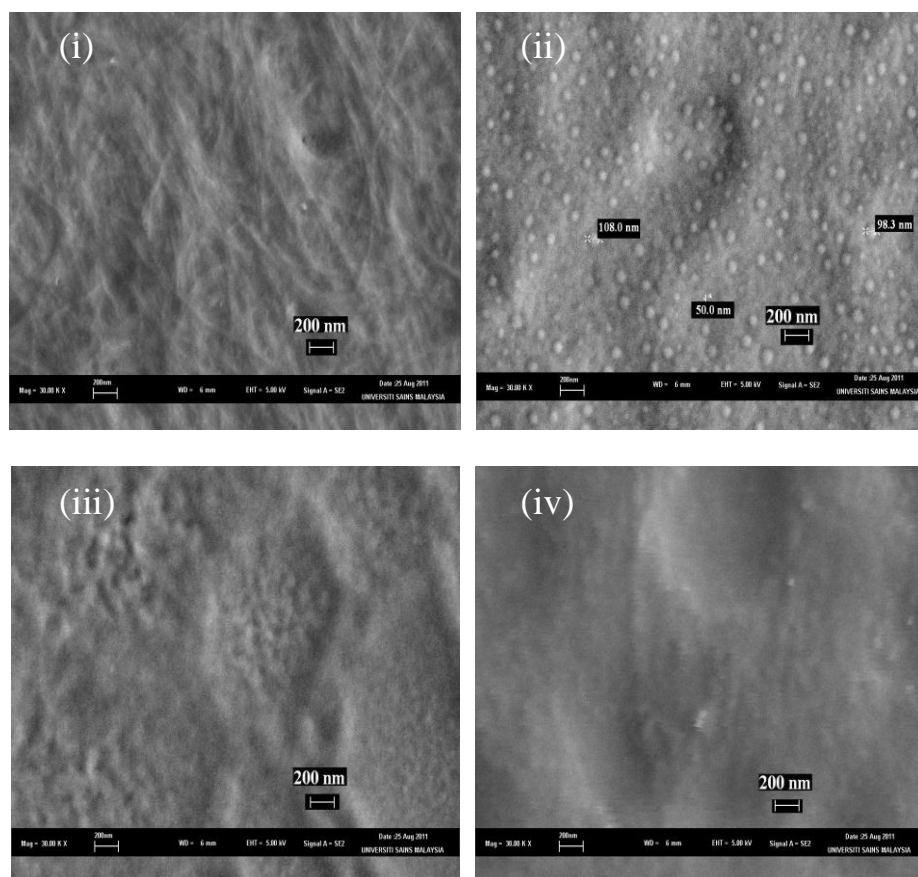


Figure 5.23: The FESEM images of P3HT:sol-gel ZnO films with (a) 0.05 ml, (b) 0.1 ml, (c) 0.2 ml, and (d) 0.3 ml sol.

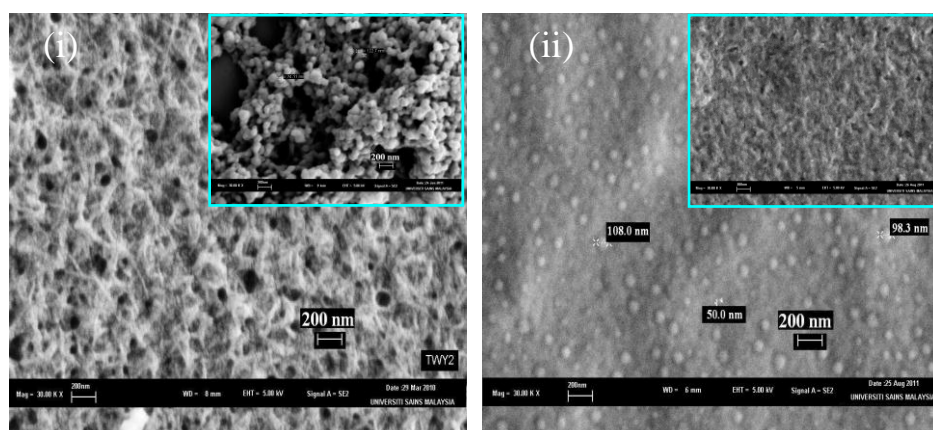


Figure 5.24: The comparison of FESEM images between (i) P3HT:ZnO NPs film and (ii) P3HT:sol-gel ZnO film. The inset shows the surface micrograph of (i) bare ZnO NPs film and (ii) bare sol-gel derived ZnO film.

Figure 5.23 shows the FESEM photographs of the surface topography of P3HT:sol-gel ZnO blend films with different sol contents. It is found that upon addition of 0.5 ml sol into P3HT, the fiber-like feature of the blend film covered with ZnO sol has appeared. Besides, several ZnO colloidal particles with sizes in the range between ~30 nm to ~60 nm are found scarcely dispersed in the film. However, the film morphology dramatically changes when the sol content is increased above 0.1 ml. Consequently, the film has been filled with the homogenous distribution of round-shaped crystal particles with an average size of ~50 to ~110 nm as shown in Figure 5.23(b). As the sol content increases further, it is found that the nano-sized grainy features of the films become less apparent. It is speculated that the grains in the film increase in size and the distribution becomes unequal, resulting in a rougher and uneven surface morphology, which is most likely due to an increased amount of Zn^{2+} solutes in the blend solution. Hence, the probability of coalescence of Zn^{2+} solutes increases that leads to the formation of larger grains (O'Brien, Koh, & Crean, 2008). From these FESEM results, it can be speculated that the blend films with higher sol content comprised of larger amount of grain boundaries, which may essentially limit the carrier mobility and hinder effective charge transport. Therefore, it is clear that the addition of 0.1 ml sol into P3HT is the optimum sol content to produce a good quality and uniform film.

To further investigate the difference in film morphology between optimized P3HT:ZnO nanoparticles blend film and P3HT:sol-gel derived ZnO film (consists of 0.1 ml sol), their FESEM images are taken as shown in Figure 5.24. The insets of Figure 5.24((i) & (ii)) show the surface micrograph of the ZnO nanoparticles film and sol-gel derived ZnO film, respectively. Varies from the large particulates and less network-like aggregation feature of the bare ZnO nanoparticles film, the sol-gel ZnO film exhibits an intensive network-like aggregation feature, which is presumably due to its sol-gel

diphase state. Virtually, the P3HT:sol-gel derived ZnO film shows a more uniform and homogenous dispersion of acceptor ZnO particulates throughout the donor P3HT matrix. Hence, it is suggested that the film prepared from sol-gel precursor route may significantly modify the film morphology, at the same time, providing more bicontinuous, interpenetrating pathways for effective charge transport.

D. Electrical Characterization

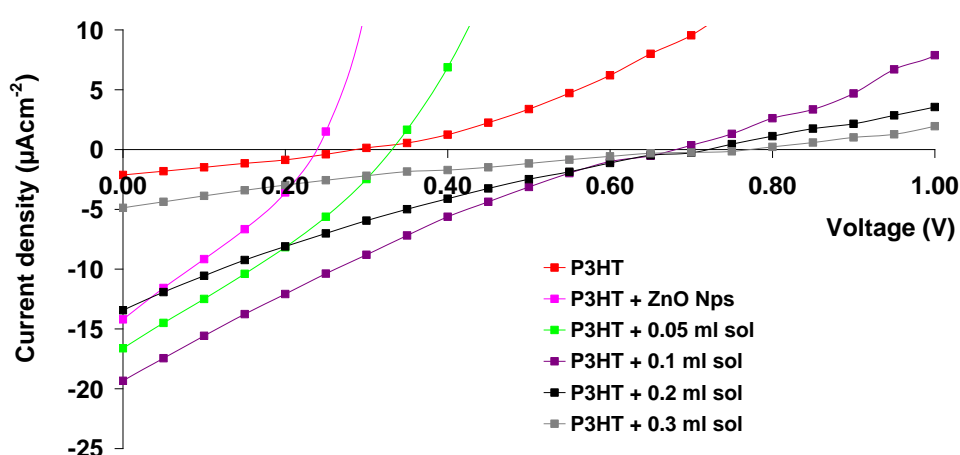


Figure 5.25: The J-V plots for P3HT:sol-gel ZnO solar cells with different sol contents in blends.

Table 5.11: The comparison of device characteristics parameters for P3HT:sol-gel ZnO solar cells.

Samples	J_{sc} (μAcm^{-2})	V_{oc} (V)	R_{sh} (± 0.1 $k\Omega cm^{-2}$)	R_s (± 0.1 $k\Omega cm^{-2}$)	FF	η ($10^{-3}\%$)
Pristine P3HT	2.13	0.28	152.9	106.1	0.29	0.17
P3HT + ZnO NPs	14.20	0.24	53.0	19.8	0.30	1.10
P3HT + 0.05 ml sol	16.62	0.33	43.3	12.1	0.29	1.59
P3HT + 0.1 ml sol	19.34	0.68	44.9	24.6	0.22	2.89
P3HT + 0.2 ml sol	13.44	0.72	51.7	38.5	0.19	1.84
P3HT + 0.3 ml sol	4.88	0.75	92.1	65.6	0.14	0.51

Figure 5.25 shows the J-V characteristics of the P3HT:sol-gel ZnO devices composed of different sol contents in the blend. The photovoltaic parameters of the devices and the variation of electrical properties as a function of sol content are presented in Table 5.11 and Figure 5.26, respectively. It has been noticed that the device with 0.1 ml sol achieves the best solar cell performance with the highest J_{sc} value of $19.34 \mu A cm^{-2}$. It can be appointed that the high J_{sc} achieved by the device consists of blend film with 0.1 ml sol may be due to its better film surface quality with evenly distributed acceptor ZnO particulates throughout the film, forming well interconnected pathways for effective charge transport. In contrast, the device with 0.3 ml sol performs the worst among all the others, achieving relatively low photocurrent that is comparable to the pristine P3HT device.

From Figure 5.55 and 5.26, one can notice that the J_{sc} slightly increases as the sol content increases until up to 0.1 ml sol, then drops gradually with further increment in the sol content. However, it is noticeable that the V_{oc} remains increasing with the sol content, which is presumably because of an increase in carrier concentration that gradually blocks the lowest state in the conduction band of the material under Burstein-Moss effect (Burstein, 1954). Generally, the variation in the devices performance may be attributed to the increased recombination loss in the blend film of higher sol content owing to the redundant thickness and high surface roughness (Kyaw et al., 2008). The diminution in the carrier mobility due to charge traps in the film results in a decrease in J_{sc} but a rise in R_s values (Mandoc, Kooistra, Hummelen, De Boer, & Blom, 2007). Thus, it is suggested that 0.1ml sol is the optimum quantity required to produce a homogenous blending with P3HT.

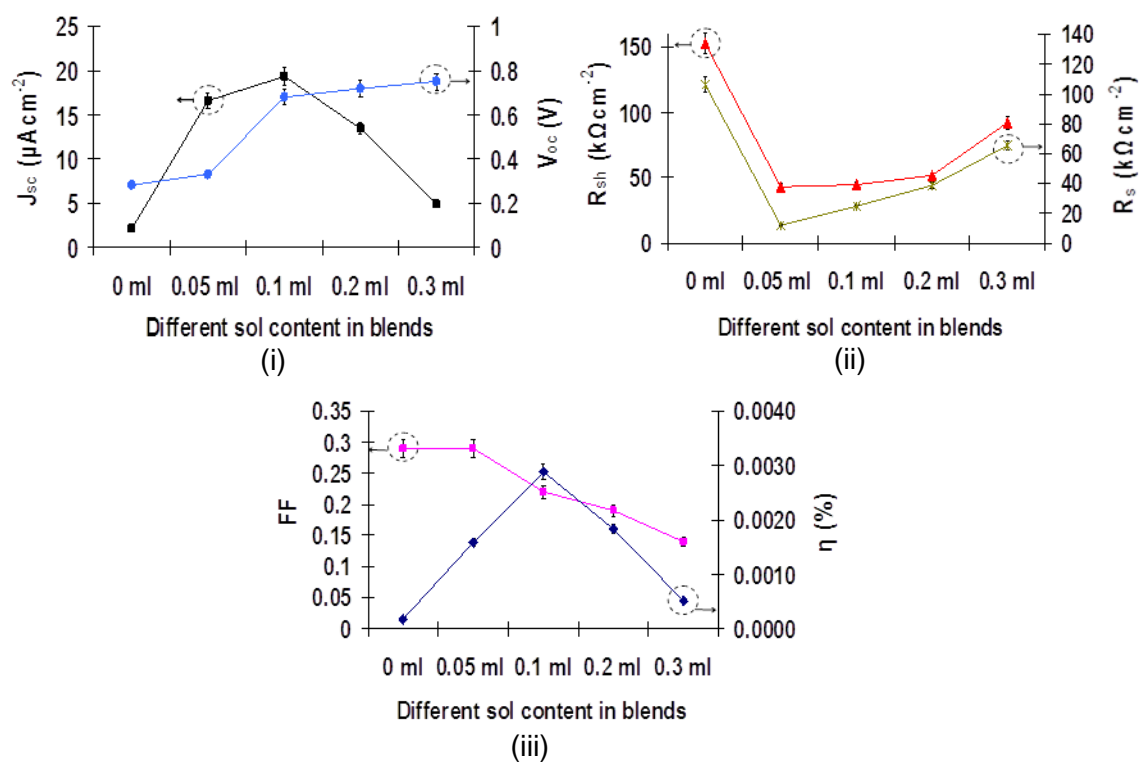


Figure 5.26: Variations in the device parameters for (i) J_{sc} and V_{oc} , (ii) R_s and R_{sh} , (iii) FF and η as a function of sol content in blends.

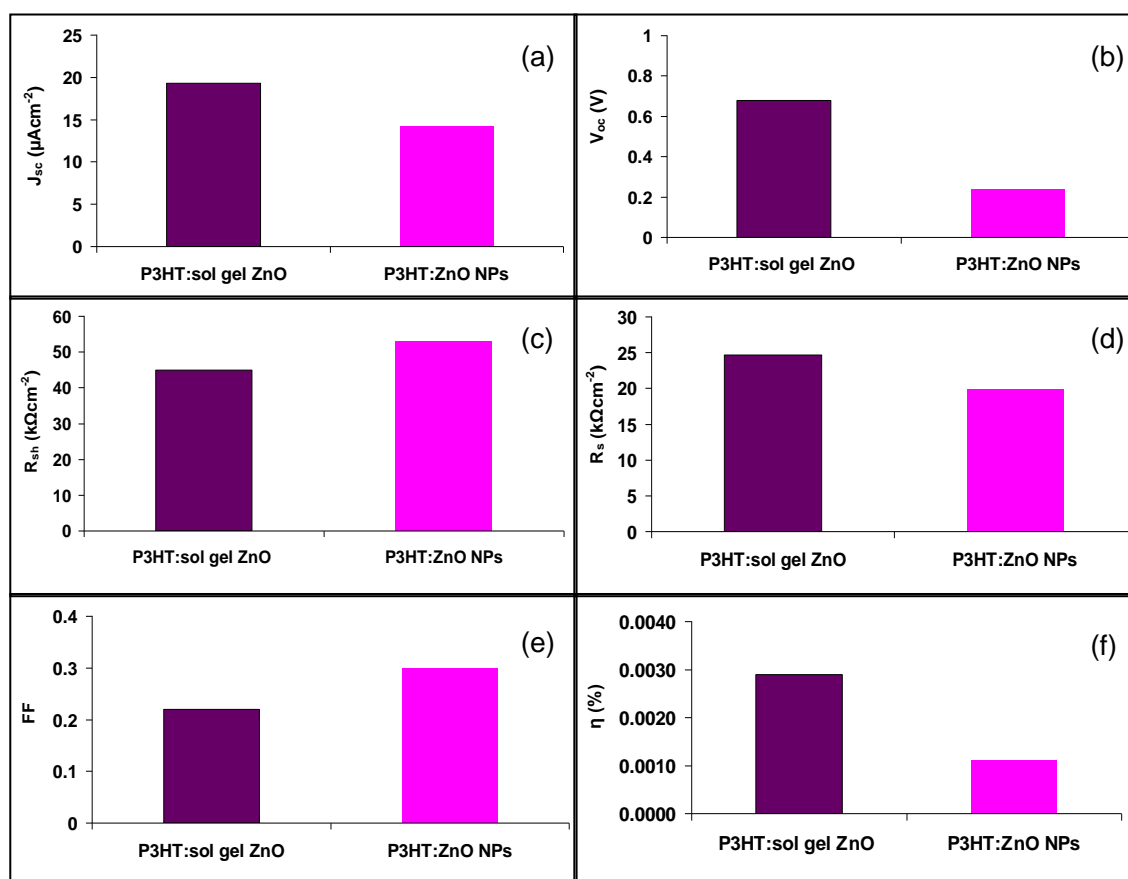


Figure 5.27: Photovoltaic comparison for P3HT:sol gel ZnO and P3HT:ZnO NPs films.

In addition, a photovoltaic comparison is made for both devices based on well optimized P3HT:ZnO nanoparticles blend film and P3HT:sol-gel derived ZnO film, as indicated in Figure 5.27. Compared to the P3HT:ZnO nanoparticles device, the P3HT:sol-gel ZnO device shows a higher value of J_{sc} and V_{oc} , and hence yields a higher device efficiency of $\approx 62\%$ greater than that of the former device, despite of a lower FF. The difference in V_{oc} achieved by both devices may be attributed to the variation in carrier concentration of both hybrid systems. However, the deviation in device resistance and FF for both devices is still not fully understood. It is speculated that the P3HT:sol gel ZnO device may have higher contact resistance between the film and metal electrode than that of the P3HT:ZnO nanoparticles based, thereby resulting a higher R_s and lower FF. This is presumably because of a weaker compatibility and adhesion of the electrode with the blend film.

5.3.2 Second Approach: Effects of Different Annealing Temperature

For the second approach, the film properties have been manipulated via thermal annealing by varying the annealing temperature during the drying and dehydration process. This attempt is taken in order to provoke further phase separation in the blend films and to induce better charge mobility.

A. Optical Characterization

The absorption spectra of the P3HT:sol gel derived ZnO blend films and the annealed films at different temperatures, T_a varying from $75\text{ }^{\circ}\text{C}$ to $150\text{ }^{\circ}\text{C}$ are shown in Figure 5.28. Noticeably, the absorption values increase with the increasing T_a and then gradually drops again, as shown as inset of Figure 5.28 (see the trend of pink coloured spots). The E_g values that estimated by the extrapolating method using the $(\alpha h\nu)^2$ vs. $h\nu$ plots are shown in Figure 5.29 and Table 5.12.

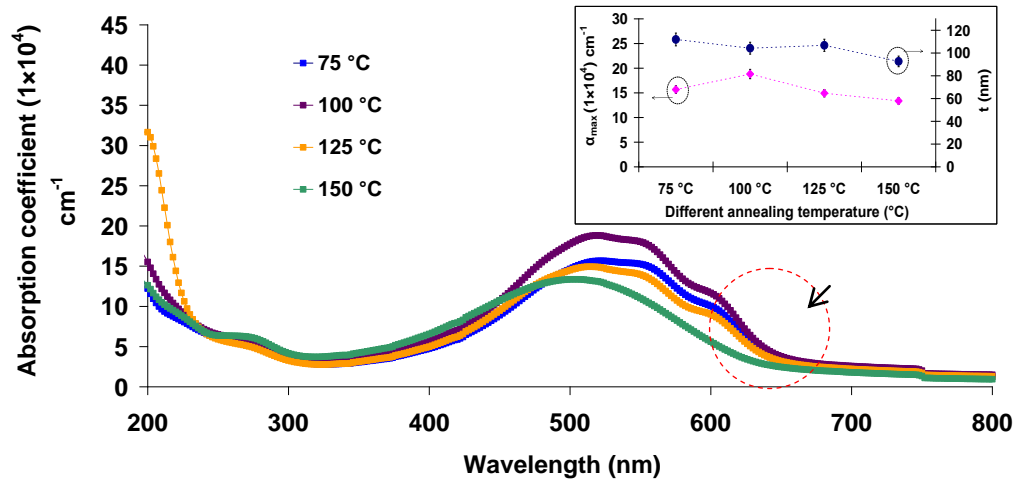


Figure 5.28: The optical spectra of P3HT:sol-gel ZnO films annealed at different temperatures, T_a . The inset indicates the variation of α_{\max} and film thickness as a function of T_a .

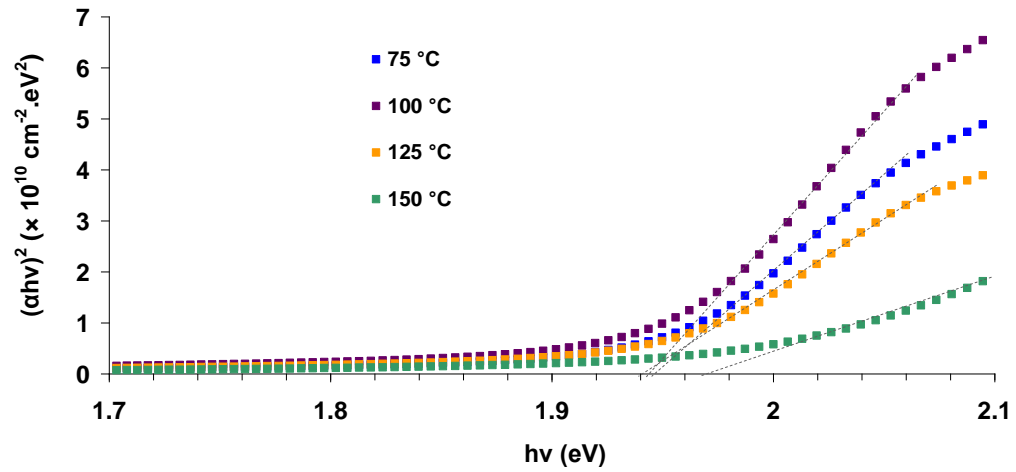


Figure 5.29: The plots of $(\alpha h\nu)^2$ against $h\nu$ for P3HT:sol gel ZnO blend films annealed at different T_a .

Table 5.12: The comparison of the α_{\max} values, the corresponding wavelength positions, average film thicknesses and estimated E_g for the P3HT:sol gel ZnO films annealed at different T_a .

Samples	Maximum absorption coefficient peak, $\alpha_{\max} (1 \times 10^4) \text{ cm}^{-1}$	Wavelength position, λ (nm)	Average film thickness, t (nm)	E_g (eV) (± 0.01 eV)
75 °C	15.7	522	111.9	1.94
100 °C	18.8	520	104.5	1.94
125 °C	14.9	514	106.8	1.94
150 °C	13.4	504	92.6	1.97

As it can be seen from these results that the E_g value remains almost constant (~ 1.94 eV) when the films annealed from 75°C to 125°C , but begins to increase, reaching 1.97 eV when the films annealed above 125°C . The increase in the E_g of the films is in good agreement with the corresponding blue-shift observed in the absorption edge, as indicated by the dashed circle in Figure 5.28. The shifting of the E_g with variation of T_a in the films can be understood by means of the effect of lattice thermal expansion which is associated to the variation in electron energies with volume. In other words, the variation in E_g with annealing temperature may be ascribed to the shift in the relative positions of the valence and conduction bands owing to the temperature dependence of dilation of the lattice (Allen & Heine, 1976). Recently, a similar result is reported by Ezema & Nwankwo, (2010) in which the increment of E_g is assigned to the evaporation of impurities ions (OH^- ions) that results in a broadening of band gap. Besides, it is noticeable that the thickness of the blend films reduces with increasing annealing temperature, varying from 111.9 nm to 92.6 nm, which is most likely due to the dehydration of the film and combustion of resultant organic substances upon heating (Zak, Abrishami, Majid, Yousefi, & Hosseini, 2011).

B. Morphological Characterization

The annealing temperature dependent morphological evolution of the P3HT:sol-gel ZnO blend films is investigated by AFM and the images in 2D and 3D forms are shown in Figure 5.30. Visually, the surface roughness of the films decreases from 12.4 to 4.4 nm with the reduced number of agglomerated grains and large submicron-sized of pores over the film when the annealing temperature, T_a is increased from 75°C to 150°C . This may because of a faster dehydration of the ZnO sol as the film annealed at elevated T_a that results in the fragmentation of agglomerated grains, forming finer size of crystal nucleus (Tsay, Fan, Chen, & Tsai, 2010). Additionally, this morphology

change may be also due to the variation of surface tension and intrinsic stress in the films during annealing which caused by deep dehydration of the films. Consequently, the films become more homogenous, uniform, and exhibit denser internal structure as it is noticeable from the images of Figure 5.30, where the boundaries among the grains in films become more hardly identifiable upon annealing treatment at elevated temperature. However, as the film annealed at 150 °C, coalescence of grains begins to take place, which can be observed from the images of Figure 5.30 (d). This suggests that at even higher T_a , the possibility of fusion of grain boundaries increases, thereby yielding a marginal increase in the grain size (Gupta, et al., 2009).

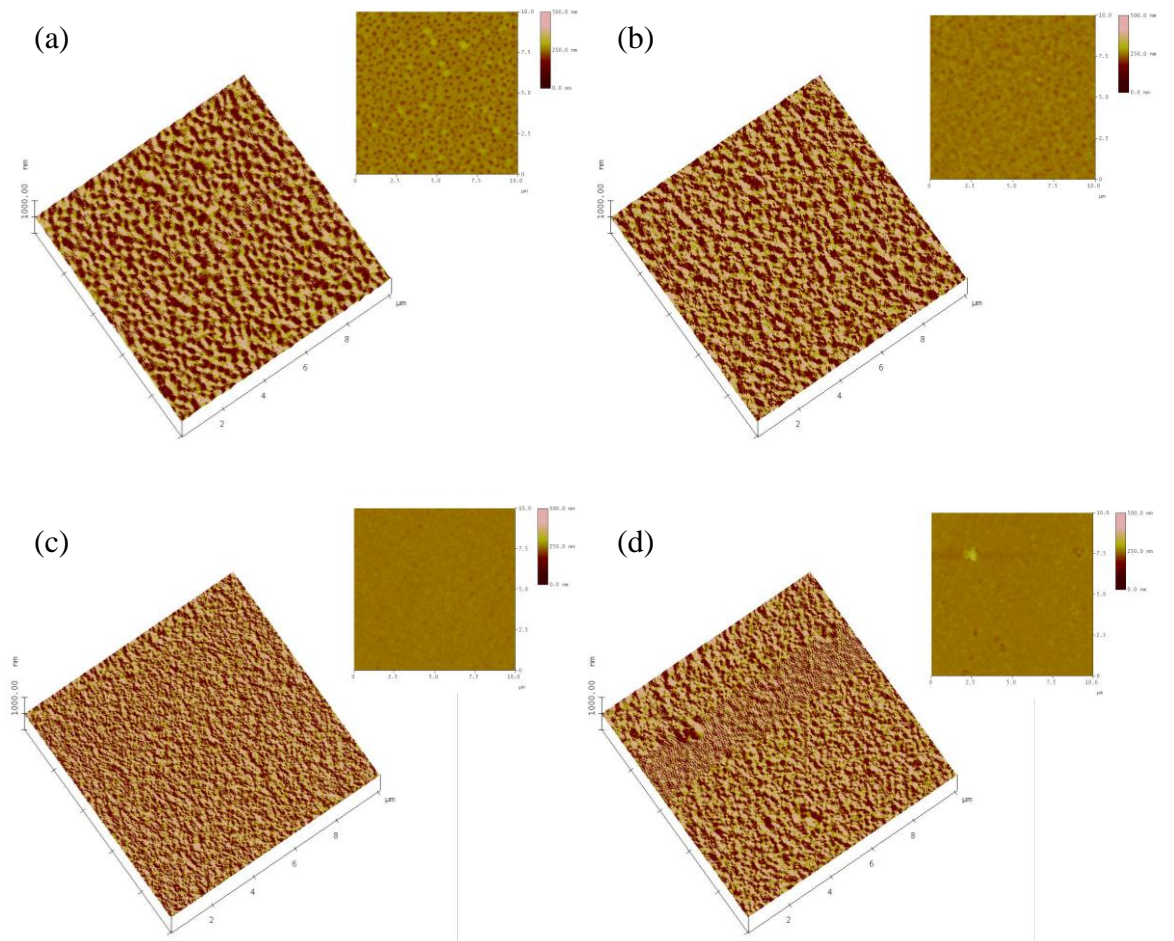


Figure 5.30: The AFM images in 2D and 3D of P3HT:sol gel ZnO films annealed at different T_a of (a) 75 °C, (b) 100 °C, (c) 150 °C, (d) 175 °C.

Table 5.13: Surface roughness values of P3HT:sol gel ZnO films annealed at different T_a .

Samples	Root-mean-square roughness, RMS (± 0.1) nm
75 °C	12.4
100 °C	6.8
125 °C	3.3
150 °C	4.4

C. Electrical Characterization

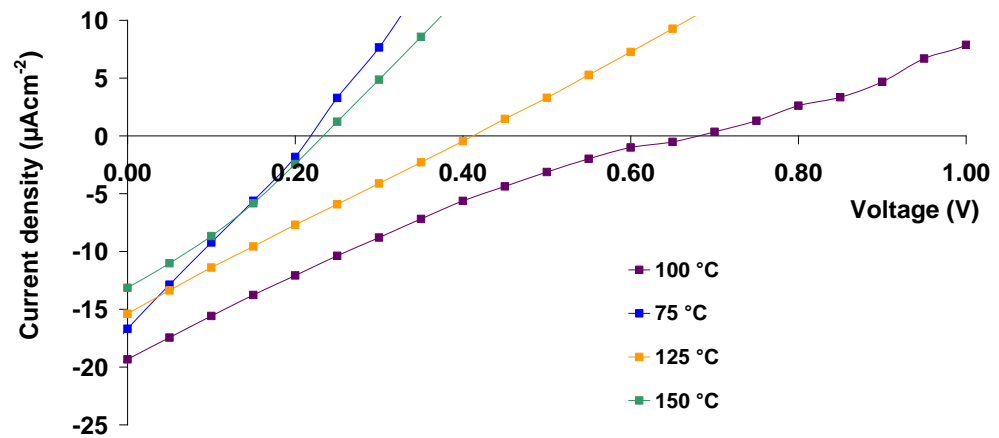


Figure 5.31: The J-V plots for P3HT:sol gel ZnO solar cells fabricated from active layers annealed at different T_a .

Table 5.14: The comparison of device characteristics parameters for P3HT:sol gel ZnO solar cells.

Samples	J_{sc} (μAcm^{-2})	V_{oc} (V)	R_{sh} (± 0.01 $k\Omega cm^{-2}$)	R_s (± 0.01 $k\Omega cm^{-2}$)	FF	η ($10^{-3}\%$)
75 °C	16.69	0.22	12.6	29.8	0.25	0.37
100 °C	19.34	0.68	44.9	24.6	0.22	2.89
125 °C	15.40	0.41	23.8	36.7	0.24	1.52
150 °C	13.15	0.23	24.8	13.6	0.28	0.85

Figure 5.31 shows the J-V characteristic curves of the blend devices prepared under different T_a , while the device parameters are listed in Table 5.14. The variation in the device parameters with increasing T_a are shown in Figure 5.32. Noticeably, the device annealed at 100 °C shows the best performance compared to the other devices, achieving the highest η of 2.89E-3% with maximized J_{sc} and V_{oc} values. This enhancement can be assigned to the improved optical absorption properties and more uniform surface morphology of the film with eliminated redundant large pores and grain agglomerations, providing better charge mobility and transport network throughout the film. The devices annealed at higher T_a exhibit deteriorated performance with decreased J_{sc} and V_{oc} . This is most possibility due to the low melting point temperature of donor P3HT, which is considered to be less than 200 °C (Verploegen et al., 2010).

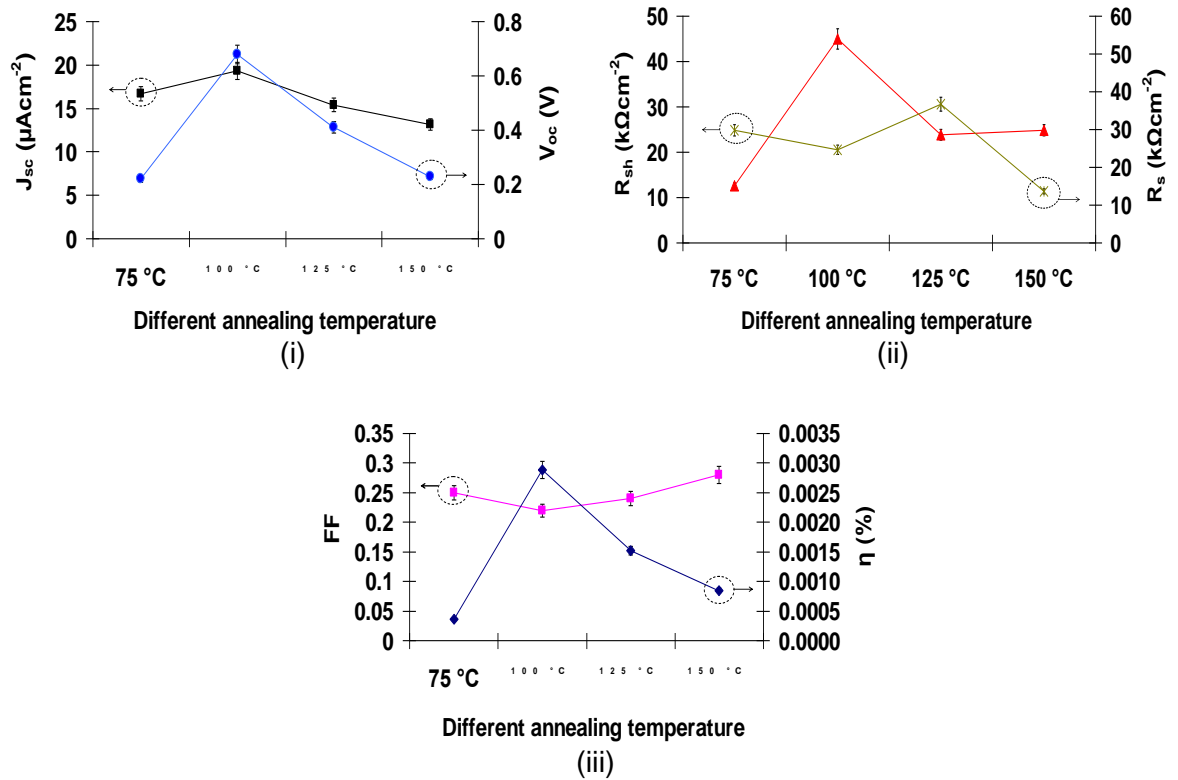


Figure 5.32: Variation in the device parameters for (i) J_{sc} and V_{oc} , (ii) R_s and R_{sh} , (iii) FF and η as a function of annealing temperature.

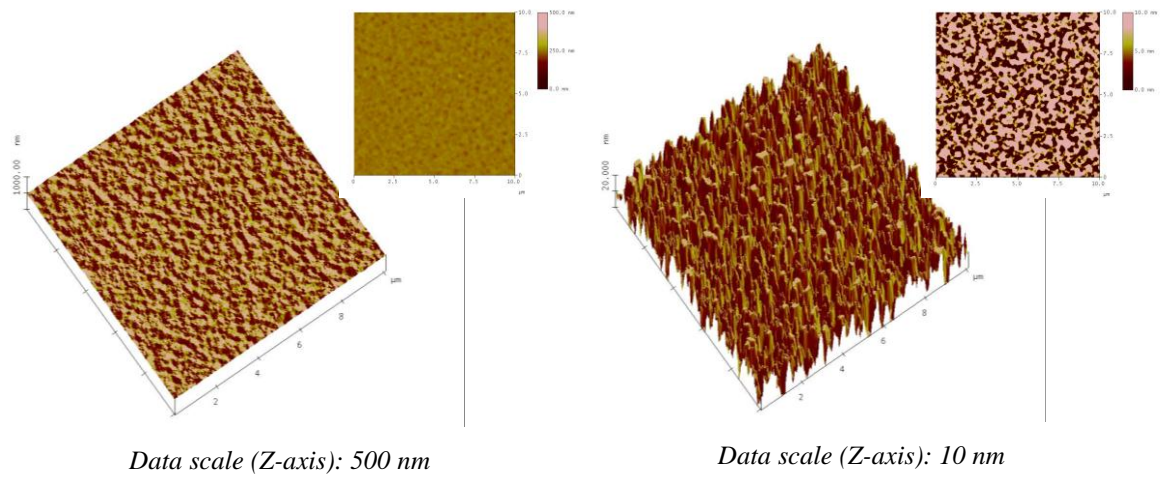
5.3.3 Third Approach: Effects of Additional ZnO Buffer Layer

In hybrid solar cells, the relatively high contact resistance between the hybrid materials and the metal electrodes has become one of the challenges that substantially affects the charge-collection properties of the devices. In order to reduce this barrier, an approach is applied in which an n-type layer (Gao et al., 2004; Nonomura, Hiromitsu, & Tanaka, 2006) or high conductive material (J. Wang, Wang, Zhang, Yan, & Yan, 2005) is inserted between the blend film and the cathode electrode to act as buffer layer. Here in this research work, ZnO buffer layer (BL) is applied due to its good compatibility with the photoactive layer. Additionally, this buffer layer can act as a protective layer to prevent the diffusion of metal electrode into the photoactive film, and hence reducing the degradation rate produces due to moisture and oxygen attack (Hau et al., 2008; Hau, Yip, Ma, & Jen, 2008).

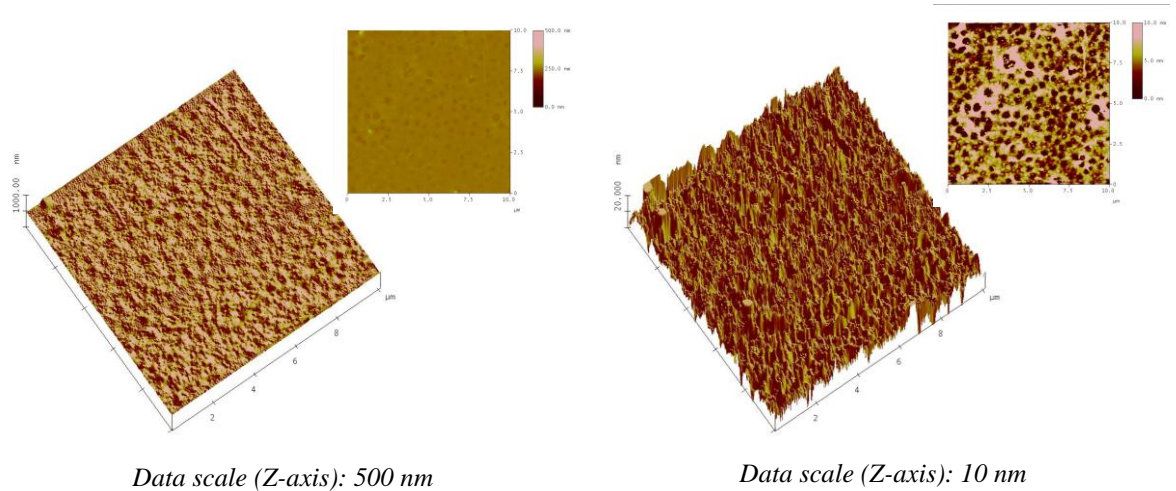
A. Morphological Characterization

The morphology-dependent influences of ZnO buffer layer on the BHJ solar cell performance are explored and studied by AFM as shown in Figure 5.33. The film with ZnO buffer layer exhibits a significant decrease in RMS roughness of 3.9 nm due to smoothened surface layer and reduced pores or voids between the grains. In order to view deeply the difference between these two films, two data scale at z-axis, namely 500 nm and 10 nm are captured. From the images of Figure 5.33(ii), the film with buffer layer is comprised of loosely aligned nanopillars with height of above 10 nm. These nanopillars are suggested to function as antenna system for efficient electron collecting from the active layer (Takanezawa, Tajima, & Hashimoto, 2008). Compared to the pristine film (see Figure 5.33(i)), the surface morphology is considerably rough and uneven, with the tightly piled up ZnO nanopillars, which may reduce the interfacial area between the donor and acceptor phases.

Additionally, the observed reduced porous V-groove structure over the film may be assigned to the nucleation thermodynamics and growth kinetics of the nuclei, as reported by Yang & Liu, (2000), in which the ZnO atom clusters are more favorable to nucleate in V-groove structure than the flat surface due to a smaller nuclei formation energy during the dehydration and oxidization process. Higher densities of nucleation are then causing the grain coalescence to take place, leading to a flatter and extended surface layer (Bang, Hwang, & Myoung, 2003).



(i) P3HT:sol gel ZnO blend film (with 0.1 ml sol; at T_a of 100 °C) without ZnO BL.



(ii) P3HT:sol gel ZnO blend film (with 0.1 ml sol; at T_a of 100 °C) with an additional ZnO BL.

Figure 5.33: Morphological characteristics of the P3HT:sol-gel ZnO film (i) without and (ii) with an additional ZnO buffer layer (BL) via AFM imaging.

Table 5.15: Surface roughness values of the films obtained from AFM.

Samples	Root-mean-square roughness, RMS (± 0.1) nm
Without ZnO BL	6.8
With ZnO BL	3.9

B. Electrical Characterization

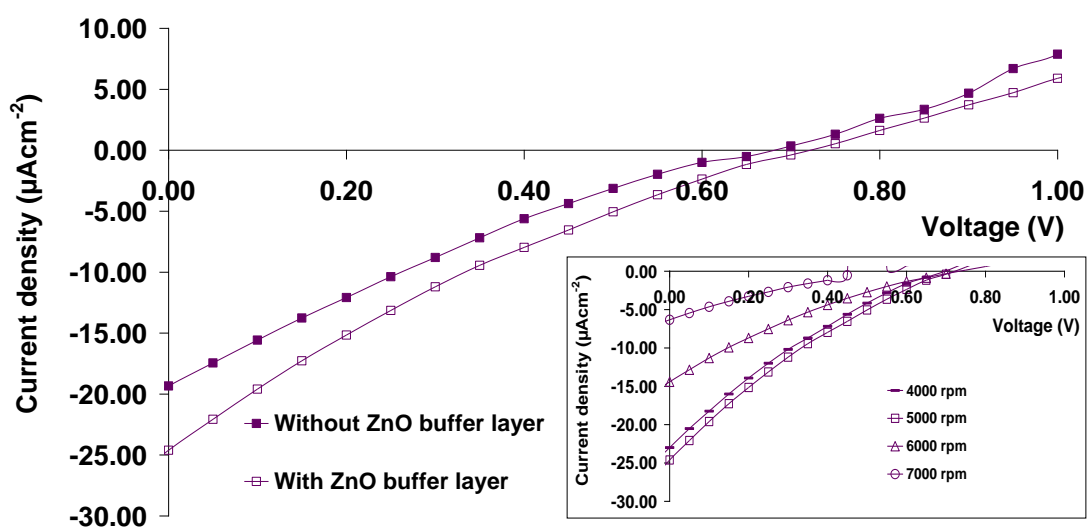


Figure 5.34: The comparison of the J-V characteristics of the solar cell devices without and with an additional ZnO buffer layer.

Table 5.16: Device characteristics parameters of P3HT:sol gel ZnO solar cells with ZnO buffer layer spun at different spin speed.

Different spin speed	Thickness of buffer layer (± 0.5) nm	J_{sc} (μAcm^{-2})	V_{oc} (V)	R_{sh} ($k\Omega\text{cm}^{-2}$)	R_s ($k\Omega\text{cm}^{-2}$)	FF	η ($10^{-3}\%$)
4000 rpm	95.5	22.99	0.70	19.9	58.9	0.19	3.06
5000 rpm	82.0	24.60	0.72	18.4	20.2	0.29	5.14
6000 rpm	65.5	14.42	0.74	30.6	107.0	0.18	1.92
7000 rpm	45.0	6.34	0.45	54.4	117.2	0.22	0.63

Table 5.17: Device characteristics parameters of P3HT:sol gel ZnO solar cells.

Devices	J_{sc} (μAcm^{-2})	V_{oc} (V)	R_{sh} ($k\Omega cm^{-2}$)	R_s ($k\Omega cm^{-2}$)	FF	η ($10^{-3}\%$)
Without ZnO BL	19.34	0.68	44.9	24.6	0.22	2.89
With ZnO BL	24.60	0.72	18.4	20.2	0.29	5.14

The comparison of the devices performance of these two types of solar cells are investigated and presented in Figure 5.34. The thickness of the ZnO buffer layer is optimized by altering the spin speed. Its effect on J-V characteristics of the devices is shown in the inset of Figure 5.34. The thicknesses of the ZnO buffer layers are estimated to be 95.5 nm, 82.0 nm and 65.5 nm for spin speed varying from 4000 rpm to 6000rpm, as indicated in the Table 5.16, respectively. There is almost no significant change in the V_{oc} of these devices, except for the buffer layer spun at 7000 rpm. The J_{sc} slightly increases from 22.99 to 24.60 μAcm^{-2} when the thickness of ZnO layer is increased. However, it drops drastically to 6.34 μAcm^{-2} for a much thicker layer. This is suggesting that an optimal thickness of buffer layer is required in order to reduce the recombination possibility caused by the limited exciton diffusion length within the film (Bang, et al., 2003).

From Figure 5.34 and Table 5.17, it is found that the device with an additional ZnO buffer layer on top of P3HT:sol-gel ZnO film exhibits a higher J_{sc} and V_{oc} of 24.60 μAcm^{-2} and 0.72 V, respectively, together with a reduced R_s value of 20.21 $k\Omega cm^{-2}$. Accordingly, the device yields a higher η of $\approx 56\%$ greater than that of pristine device. There are several possible reasons for the improved J_{sc} and η of the device. First, it can be attributed to the increased number of photogenerated charge carriers collected by the loosely aligned ZnO nanopillar antennas since the average distance travelled by carriers from active layer to the cathode is shortened. Hence, such a device constitutes better charge transport and collecting network system than the pristine device. Secondly, the smoothened and extended film surface morphology results in a larger interfacial area

between the donor P3HT and ZnO, thereby increasing the exciton dissociation rate. In addition, the irradiated light may be scattered or reflected multiple times within the internal optimum porous structure of the film that results in enhanced light absorption by increasing the optical path length; producing higher J_{sc} for the device (Hu, Zhang, Liu, Hao, et al., 2011; Hu, Zhang, Liu, Li, et al., 2011; Park et al., 2010). Besides, the high conductive property of ZnO may lead to more charge carrier accumulations occur at the interface between Al electrode and the blend film that aids in reducing the contact potential barrier between them, as indicated by a reduced R_s value.

In conclusion, by modifying the physical properties and charge transport of the hybrid systems through an easy means of sol-gel synstheiss route, the devices have been further optimized, resulting in an improvement in solar cell performance.

CHAPTER 6

CONCLUSIONS AND FUTURE WORKS

6.1 Conclusions

Hybrid solar cells have attracted great research attention due to the combine advantages of conjugated polymers and inorganic semiconductors, as well as the ability to readily tailor their physical and electrical properties. The P3HT, which is a types of highly conductive conjugated polymer, acts as an electron donor while the inorganic metal oxide nanoparticles act as electron acceptors having high charge carrier mobility. At the preliminary stage of this research work, the effects of blend composition on the optical, structural, morphological and electrical properties of P3HT:ZnO hybrid system have been evaluated. To make a comparison, another two different types of hybrid systems, namely P3HT:TiO₂ and P3HT:Y₂O₃ are then fabricated and studied as well. In order to further improve the compatibility between P3HT and ZnO so that to enhance the devices performance, a blend of P3HT with as-synthesized ZnO through sol-gel route is prepared and the processing parameters have been successfully optimized via three different approaches as the final stage of this research work.

For the optical characterizations, pristine P3HT film exhibits a strong absorption in the visible wavelength range (450-650 nm), whereas the metal oxide nanoparticles films are found to favorably absorb light in the UV range (200-400 nm). In this work, it is found that all the three types of metal oxide nanoparticles in thin film form exhibit steep absorption edge characteristics of direct band gap semiconductors which are deviated from that of the bulk counterparts. However, the estimated E_g values are different from the reported values which are presumed due to the variation in the stoichiometric of the involved synthesis method, the purity degree of nanoparticles and crystallite size. Upon the addition of moderate amount of metal oxide nanoparticles

(low doping rate), the absorbance is enhanced with a narrowed optical band gap, E_g . However, the high nanoparticles doping in the blends is found to have no further significant effect on the absorbance and E_g of the blends becomes comparable to that of P3HT film. In general, the blends exhibit comparative E_g of values from 1.94 to 1.97 eV. As compared to other hybrid systems, P3HT:ZnO blend film achieves slightly higher absorption coefficient which may be attributed to the relatively high photon absorbing capability of ZnO nanoparticles ($\approx 10^5 \text{ cm}^{-1}$). For P3HT:sol-gel ZnO film, the optical property does not show remarkably different behavior compared to that of P3HT:ZnO nanoparticles film, despite of the deviated absorption spectrum obtained for bare sol-gel ZnO film than that of the ZnO nanoparticles film. However, it is found that the E_g of P3HT:sol-gel ZnO film is slightly smaller than that of the P3HT:ZnO nanoparticles film which corresponds to a smaller E_g of the sol-gel ZnO film. Upon thermal annealing in the temperature range (from 75°C to 150°C), the E_g of the films is increased which may be assigned to the effect of lattice thermal expansion that correlated to the variation in electron energies with volume. Thermal annealing can induce a higher absorption with a decreased film thickness owing to the improved surface morphology and decomposition of the sol substances, respectively.

The structural properties of the selected films have been studied by XRD technique. Pristine P3HT prepared in chloroform exhibits a single crystalline peak corresponding to (100) plane at diffraction angle of $\sim 5.2^\circ$. Meanwhile, it is noticed that the polycrystalline ZnO nanoparticles in powder form exhibit wurtzite structure and possess an average crystallite size of $\sim 20 \text{ nm}$, whereas TiO_2 and Y_2O_3 are belong to tetragonal (rutile and anatase phase) and cubic crystal structures with average crystallite size of ~ 20 and $\sim 23 \text{ nm}$, respectively. Nevertheless, due to a very small XRD peak detected in the P3HT:inorganic nanoparticles blend films and the films are found to be mostly in amorphous phase, the crystallization process upon inorganic nanoparticles

doping is therefore considered to be negligible. On the other hand, P3HT:sol-gel ZnO blend films exhibit several diffraction peaks at (002), (101), (110) planes. The relative peak intensities suggest that there is no preferred grain orientation in the film. The crystallite size and intensities of XRD pattern in the P3HT film decrease, but the crystallite size of ZnO remains to increase with the increasing sol content, indicating the coalescence of small ZnO crystallites to form larger crystallites. However, the dislocation density of the films exhibits an increasing trend as well, indicating an increased concentration of lattice imperfection of the blends with higher sol content. This shows that the ZnO sol content playing major role in influencing the physical properties of the blends.

Based on morphological characterizations using AFM and FESEM analysis, the P3HT has shown a relatively smooth surface with a small RMS roughness value of about 1.1 nm. Upon the addition of inorganic nanoparticles, phase separation takes place between the P3HT donor and ZnO acceptor as indicated by the increment in surface roughness and morphological features. A light nanoparticles doping yields a finer phase separation and the molecules are closely arranged throughout the blends. In contrast, a heavier doping yields a larger scale phase separation due to excessive nanoparticles aggregations. This results in redundant coarse surface morphology (RMS values of >20 nm) for the blend films which is unfavorable for high device efficiency. Additionally, the excess amount of inorganic nanoparticles aggregates has seriously distorted the P3HT chain structure as evidenced by FESEM photograph. In this study, it is found that the optimum degree of fine phase separation take places at nanoparticles doping of less than 5%. For comparison between the three types of P3HT:inorganic hybrid systems, it is deduced that P3HT:ZnO film possesses a better morphology property than the others, owing to its well-detectable phase separation and more

homogenous, moderate-scaled of nanoparticles dispersion over the film without perturbing the P3HT domains for efficient hole transport.

In order to further improve the devices performance, film morphology is modified by using sol-gel route and few processing parameters are altered (e.g., sol content, annealing temperature and addition of n-type ZnO buffer layer). As compared to P3HT:ZnO nanoparticles film, P3HT:sol-gel ZnO film exhibits an improved surface quality with reduced extent of ZnO aggregations. Upon varying the sol content in blends (from 0.05ml to 0.3ml), the film morphology changes from hillock-like feature to highly porous feature with increased RMS values which is assigned to an increased Zn^{2+} coalescence and a faster rate of phase separation between P3HT and the Zn^{2+} adsorbed by mixture solvent. Based on FESEM images, it can be concluded that blend film with 0.1 ml sol content possesses much better organized film morphology with evenly dispersed ZnO particulates in the film, forming well-defined pathways to facilitate charge transport. By annealing the sol-gel films, the roughness reduces from 12.4 to 4.4 nm with a reduced number of larger pores and surface defects. This is presumably because of a faster dehydration and decomposition of ZnO sol that yields a fragmentation of agglomerated grains. Otherwise, it may be due to the variation of surface tension and intrinsic stress in the films upon heating. However, at even higher annealing temperature, the possibility of fusion of grain boundaries increases, resulting in a marginal increase in grain size. Accordingly, the film roughness increases again with the formation of uneven large grain coalescence. Lastly, by inserting an additional ZnO layer on top of P3HT:sol-gel ZnO film, the surface roughness is found to be successfully reduced due to a higher densities of Zn^{2+} nucleation in the V-groove structure of the P3HT:sol-gel ZnO film layer that results in a flatter, extended surface.

In general, the variations in the photovoltaic characteristics are well-related to the variations in optical, morphological as well as structural properties and charge

transport network of the hybrid systems. The increased photon absorption in broader wavelength region, a better organized morphology with bi-continuous percolation pathways to facilitate charge transport and improved charge mobility are the main factors contributing to the device enhancement. In contrast, the device deterioration may be well-related to the increased recombination loss in the blend film owing to the redundant thickness and high surface roughness. The existence of the low carrier mobility due to charge traps or surface defects in the films yields a lower J_{sc} , together with an increased R_s value. It is found that the blend composition dependence of P3HT:inorganic hybrid solar cells device performances are varying depending on the types of inorganic nanoparticles. For P3HT:ZnO nanoparticles device, the best device is obtained by 3% ZnO doping into the blend to show a device efficiency, η of 1.1E-3%. Meanwhile, for P3HT:TiO₂ and P3HT:Y₂O₃ devices, the best performances have been achieved for hybrid systems consisting of 5% TiO₂ (η of 1.0E-3%) and 4% Y₂O₃ (η of 0.69E-3%), respectively. For P3HT:sol-gel ZnO devices, it is concluded that 0.1 ml sol in blend that annealed at an optimal elevated temperature of 100°C gives the best device performance, contributing to a higher η of 2.9E-3% due to higher J_{sc} and V_{oc} . To further enhance the device efficiency, a device with additional ZnO buffer layer which acts as electron collecting layer has been designed. By shortening the average distance travelled by electrons to reach the cathode within their life time, such device yields an increased η of $\approx 56\%$ greater than that of the device without ZnO buffer layer.

In conclusion, hybrid solar cells have shown a promising performance since their properties can be easily modified and optimized. Meanwhile, light-weight, cost-effective and flexibility of these types of solar cells deserve intensive research works. The largest challenge remains in the low device efficiency which is mainly because of poor charge mobility, device instability owing to fast degradation, and high series resistance.

6.2 Future Works

As explained earlier, it is found that the peculiar properties of P3HT:ZnO hybrid system has made it applicable in photovoltaic applications. However, in the present work, only several processing parameters are varied and optimized, thereby limiting a comprehensive understanding of the properties of this hybrid system. This work is suggested to be continued by including more others processing parameters such as choice of different solvents, applying other types of metal electrodes, sol aging duration, amount and types of sol stabilizer, etc. Besides, the results obtained from the film produced via sol-gel route can be compared with several other preparation techniques such as spray-pyrolysis, sputtering, hydrothermal, etc. Accordingly, the best technique used to produce a better P3HT:ZnO hybrid device performance can be identified. In addition, in future work can include the measurement of charge carrier mobilities and energy levels of the donor and acceptor materials using appropriate techniques such as photoinduced electroluminescence and cyclic voltammetry (CV), respectively.

In the present work, the device fabrication and measurements are carried out in ambient condition which may increase the risk of degradation of the devices. Therefore, in future works, it can be suggested that all the experimental work would be done under vacuum condition. Additionally, the device can be encapsulated or shielded in order to protect the device against oxygen and moisture attack. As found out by several reports, the degradation of ITO can be one of the factors for the failure of the device performance. It is suggested that future work can include the plasma treatment or thermal annealing of the ITO under vacuum condition in order to produce a device with excellent electrical contacts.